

MICROANALYTICAL STUDY OF
DISCONTINUOUS PRECIPITATION
IN ALUMINIUM-ZINC ALLOYS

By

IVAN GUILLERMO SOLÓRZANO-NARANJO, Eng., M.Sc.

A Thesis

Submitted to the School of Graduate Studies
in Partial Fulfilment of the Requirements
for the Degree
Doctor of Philosophy

McMaster University

June 1983



DISCONTINUOUS PRECIPITATION IN Al-Zn ALLOYS

Dedicated to Bryan and Alexandro

DOCTOR OF PHILOSOPHY
(Metallurgy and Materials Science)

MCMASTER UNIVERSITY
Hamilton, Ontario

TITLE: Microanalytical Study of Discontinuous Precipitation
in Aluminium-Zinc Alloys

AUTHOR: Ivan Guillermo Solórzano-Naranjo,
Eng. (University of Rio de Janeiro,
Brazil)
M.Sc. (University of Rio de Janeiro,
Brazil)

SUPERVISOR: Professor G.R. Purdy

NUMBER OF PAGE xviii , 202

ABSTRACT

This thesis treats the discontinuous mode of precipitation in Al-22 and 28 at.% Zn. High resolution STEM x-ray microanalysis has been used to measure the composition profiles in individual depleted lamella formed under isothermal conditions. These data, combined with local values of cell velocity and interlamellar spacing, have been used to evaluate the kinetic and thermodynamic quantities of main concern. It is shown that the reaction is grain boundary-diffusion controlled and depending of individual grain boundary characteristics. The driving force for grain boundary migration and possible free-energy sinks are discussed. The results are compared with predictions of existing theories.

The problem of the optimal interlamellar spacing is addressed, mainly from the experimental point of view. Experimental data for Al-Zn and Mg-Al alloys are analyzed and related to the discussion.

It is demonstrated that initiation involves diffusion induced grain boundary displacements, and that during the growth process a significant amount of elastic energy is stored in the product phases. The dissolution of the reheated lamellar structure is volume diffusion-controlled.

ACKNOWLEDGEMENTS

The author is indebted to his supervisor, Dr. G. R. Purdy, for suggesting the topic of research treated here, for the provision of laboratory facilities and for his continuing guidance and encouragement throughout the course of this work. Sincere gratitude is expressed to Dr. J. D. Embury and Dr. G. C. Weatherly for serving on the Ph.D. Supervisory Committee.

The author wishes to express his many thanks to Mr. P. Zaya for assistance with the non-linear regression analysis, to Mrs. H. Kennelly for rapid and accurate typing of the manuscript and to Dr. V. S. Raghunathan and Mr. N. Parikh for their formidable help during the final preparation of this thesis.

Thanks are also extended to many of the faculty and graduate students of the McMaster Metallurgy Department for stimulating discussions; and to the technical staff of the McMaster Engineering Building and of the Institute for Materials Research for technical assistance.

The financial support from the following institutions is gratefully acknowledged: Canadian International Development Agency (in particular, Mrs. Barbara Richardson), Secretaria de Tecnologia Industrial (Brazil) and Universidade Catolica do Rio de Janeiro (Brazil).

TABLE OF CONTENTS

		<u>PAGE</u>
CHAPTER 1	INTRODUCTION AND SCOPE	1
CHAPTER 2	LITERATURE REVIEW	5
2.1	Occurrence of Reaction	5
2.2	Initiation Mechanisms	7
2.2.1	Precipitate induced boundary migration	9
2.2.2	Precipitation in migrating boundaries	12
2.3	The Growth Process	14
2.3.1	The nature of the driving force	14
2.3.2	Models for growth kinetics	17
2.3.3	Thermodynamical treatment of the reaction front	25
2.4	Reaction Morphology	33
2.4.1	Reaction Classification	33
2.4.2	Micromorphology	34
2.4.3	Macromorphology	35
2.5	Effect of Grain Boundary Structure on Kinetics	39
2.6	Dissolution of the Discontinuous Product	46
2.7	The Role of Interphases: some Thermodynamical and Structural Aspects	50
2.2.1	Interfacial equilibria	50
2.2.2	the structure of two-phase interfaces	57

	<u>PAGE</u>
CHAPTER 3 EXPERIMENTAL PROCEDURE AND TECHNIQUES	64
3.1 The Choice of Alloy System	64
3.2 The Al-Zn System	65
3.3 Alloy Preparation	66
3.4 Heat Treatment Schedule	68
3.5 Sample Preparation	69
3.6 Electron Microscopy	71
3.7 STEM Microanalysis	71
3.7.1 Principles of characteristic x-ray produc- tion	72
3.7.2 Resolution limiting factors	74
3.7.3 X-ray data collection	77
3.7.4 Operation and interpretation of data	79
CHAPTER 4 EXPERIMENTAL RESULTS	82
4.1 Morphological Features of the Discontinuous Precipitation Product	83
4.1.1 Extent of the reaction	83
4.1.2 Modes of grain boundary migration	87
4.1.3 The reaction front morphology	95
4.1.4 Microstructural characteristics of the discontinuous product	96
4.1.5 Mechanisms of lamellae multiplication	105
4.1.6 Stability of the discontinuous product	111
4.2 Microanalysis and Microdiffraction Results	111
4.2.1 The steady state lamellar reaction front	111

	<u>PAGE</u>
4.2.2 The initial bowing of the grain boundary	130
4.3 Other Modes of Decomposition	137
4.4 Dissolution of the Discontinuous Product	145
CHAPTER 5 DISCUSSION	159
5.1 The Precursor of Discontinuous Precipitation	160
5.2 The Steady State Growth	162
5.2.1 The resulting microstructure and thermo- kinetic results	162
5.2.2 The interlamellar spacing problem	166
5.3 The Post Dissolution Microstructure	184
5.4 The Analytical Results	185
5.5 Suggestions for Further Work	186
CHAPTER 6 CONCLUSIONS	188
REFERENCES	192

LIST OF FIGURES

<u>FIGURE</u>		<u>PAGE</u>
1	Ideal discontinuous precipitation of β plates from supersaturated α_0 . The α'/α_0 boundary acts as a high diffusivity path.	2
2	Free energy diagrams for a) interface at rest, b) grain boundary in discontinuous precipitation assuming local equilibrium, and c) grain boundary in discontinuous precipitation with deviation from local equilibrium. From Hillert ¹⁰ .	8
3	The pucker mechanism for initiation reaction after Tu and Turnbull ¹¹ . For explanation see text.	11
4	Three stages in a possible ageing sequence. In state 2, the equal size precipitates of Stage 1 have coarsened, such that the outer precipitates have grown carrying the grain boundary forward with them. When the boundary is released from the center (shrinking) precipitate it will straighten abruptly. After Lange and Purdy ¹⁴ .	11
5	Development of a precipitation cell after Fournelle and Clark ¹⁵ . For explanation see text.	13
6	Cahn's solution of the moving boundary diffusion problem. The numbers on the curves are values of the parameter a .	20
7	A non-planar α_0/α' front of the type computed by Sundquist ⁴⁵ .	23
8	Calculated concentration profiles for the case of grain boundary diffusion to a rod. The numbers on the curves are values of $\sigma(b-a)$. After Perovic and Purdy ⁴⁶ .	24
9	Interfacial force balance at junctions in a lamellar discontinuous precipitation product ¹⁰ .	28

<u>FIGURE</u>		<u>PAGE</u>
10	Schematic shapes the grain boundary can take if a) the full chemical force acts in a high mobility boundary, b) the chemical force is partially offset by a friction term, c) no net force acts on the boundary, and d) precipitate fractions aid boundary motion. From reference 46.	28
11	Proposed mechanism controlling the average interlamellar spacing. After Sundquist ⁴⁵ .	29
12	Free-energy diagram for discontinuous precipitation showing the various sinks for the total driving free-energy, as proposed by Hillert ²² . The dashed curves apply for the growing α and β phases, x_2 is the composition of the boundary material and of the growing α' phase.	30
13	a) Schematic diagram of S-mechanism, after Fournelle ⁶⁴ , b) Development of double seams via S-mechanism, after Frebel and Shenk ⁶³ .	37
14	Possible mechanisms for lamellae multiplication during discontinuous precipitation: a) branching, b) repeated nucleation on cell boundary, c) nucleation in recess of cell boundary. After Butler ⁶⁵ .	38
15	Penetration depth of Zn along [110] tilt boundaries in Al at 250°C as function of misorientation angle. After Herbeval et al. ⁷³ .	40
16	Plot of the Zn/Al count rate as a function of distance along the grain boundary plane for 3 bicrystals, classified by their axis/angle pair. After Briceno-Valero and Gronski ⁸³ .	43
17	Schematic curves of cellular reaction rate vs. temperature, after Tu ⁹⁹ .	47
18	A section through a γ -plot for a precipitate showing one coherent interface, together with the equilibrium shape (a disc). From ref. 151.	52
19	Wulf construction for one-facet nucleus at a grain boundary, $\gamma_{\alpha\beta}^c < \frac{1}{2} \gamma_{\alpha\alpha}$. From ref. 13.	52

<u>FIGURE</u>		<u>PAGE</u>
20	Illustration of vector $\vec{\xi}$ for anisotropic surface of orientation \vec{n} . After Hoffman and Cahn ¹²² .	55
21	Two graphs of equilibrium construction. a) particle with isotropic but unequal surfaces b) particle at a twin boundary. In both cases the equilibrium shape is given by truncation of isolated particles. After Cahn and Hoffman ¹²³ .	55
22	Precipitates morphology on the plane of a grain boundary. a) the lens type shape, local equilibrium around its circumference is assigned, no torque is exerted by the particle; the grain boundary remains stationary. b) The disc type shape which lies on a habit plane of the lower grain α_1 . The pair of arrows indicates the torque exerted by the precipitate which twists the boundary.	56
23	Mechanisms for coherency loss. a) Dislocation punching from interface. b) Capture of matrix dislocation. c) Nucleation at edge of lengthening plate. d) Loop expansion by vacancy condensation in the precipitate.	61
24	Equivalent dislocation arrays which fully relieve a dilational misfit. After Sargent and Purdy ¹⁵⁴ .	63
25	a) The Al-Zn phase diagram published by Hultgren et al ¹⁶⁵ . b) A modified version, borrowed from ref. 166.	67
26	Schematic illustration of the heat treatment sequences for the Al-22 at.% Zn alloys	69
27	McMaster HB5' STEM x-ray detector system.	78
28	a) Al-22 at.% Zn, 473K, 300 s, b) Al-28 at.% Zn, 473K, 300 s. Note high density of discontinuous precipitation product and some precipitate-free grain boundaries. SEM micrographs. 170 \times .	84

<u>FIGURE</u>		<u>PAGE</u>
29	Average temperature-velocity dependence for discontinuous precipitation in Al-22 and 28 at.% Zn alloys.	85
30	Al-22 at.% Zn, 423K, 300 s SEM micrograph 4200 \times .	86
31	Average cell spacing versus ageing temperature.	86
32	Al-22 at.% Zn, 478K, 300 s. The migration of the boundary took place in the bulk. The thin foil was maintained in the TEM stage for about 2 h. The boundary did not continue moving at a measurable speed. The effect of surface diffusion is probably responsible, STEM, bright field, BF, micrography, 20K \times . Inset the selected area microdiffraction patterns from the two grains showing they are slightly misoriented.	88
33	Same sample as in fig. 31. Different grain boundary. A second stage of boundary migration proceeds in the thin foil but this time, producing discontinuous precipitates. Annular dark field, ADF, STEM micrograph 10K \times . The SADP insert shows that the two parent grains are more misoriented with each other than those in the previous figure.	89
34	Development of discontinuous precipitation colonies at both sides of the original grain boundary position. This is an as aged and quenched microstructure, the precipitation; took place isothermally, 478K, 30 s in the bulk. Al-22 at.% Zn, STEM, ADF micrograph 5K \times .	91
35	Al-22 at.% Zn, 428K, 300 s. ADF STEM micrograph showing a regularly formed single seam colony.	92
36	Al-22 at.% Zn. 478K, 300 s. ADF STEM micrographs showing a large extent of discontinuous precipitation reaction in a partial double seam morphology.	92
37	Al-22 at.% Zn, 428K, 300 s ADF STEM micrograph, 2K \times .	93

<u>FIGURE</u>		<u>PAGE</u>
38	Al-22 at.% Zn. 428K, 300 s, ADF STEM micrograph, 5K ×.	93
39	Al-22 at.% Zn, 489K, 180 s. Single, double seam and intermediate morphologies are evident. Annular dark field under low mag image setting STEM micrograph.	94
40	An irregular cell front, 428K, 300 s. STEM ADF micrograph.	97
41	A regular reaction front, 478K, 300 s. STEM ADF micrograph.	97
42	Two typical cell matrix interfaces characteristic of steady state growth. 428K, 300 s a) TEM micrograph, 25K ×, b) STEM micrograph 50K ×. Interfacial precipitates occurred after the thinning of the foil, are decorating the reaction front.	98
43	The imaging of the α_0/α' interface. a) No shape is apparent, b) Dynamical fringes aid its visualization. B.F. TEM micrographs. 44K ×	99
44	Imaging of the α_0/α' interface in the STEM a) BF, b) CDF with a parent grain reflection. 428K, 300 s.	100
45	Sample annealed at 428K, 300 s. a) in ADF low magnification, where a discontinuous precipitation cell and some bumps are visible. b) Magnification of the DIGM region. Dark zones are Zn rich pockets.	101
46	Bowing grain boundary. a) bright field, b) Centered dark field with a growing grain reflection. 428K, 300 s. TEM micrograph, 30K ×.	102
47	Disorganized microstructure precedes the steady state lamellar growth in a) single, and b) double seam morphologies. TEM micrographs, 10K ×.	103
48	Grain boundary migration preceding the onset of discontinuous precipitation. 478K, 300 s. STEM micrograph 20K ×.	104

<u>FIGURE</u>		<u>PAGE</u>
49	a) Stem annular dark field image of a double seam morphology. b) Centered dark field image with a right hand parent grain reflection. 478K, 300 s, 5K \times .	106
50	a) BF image of a double seam morphology, b) and c) Matrix CDF from each grain of a) showing crystallographic orientation relationship, between parent grain and discontinuous cell.	107
51	a) A preexistant colony has grown in situ a second stage 20 K \times . b) A third stage. The selected area diffraction patterns show that the cell/matrix orientation has been maintained.	108 109
52	a) Bright field; b) Transformed cell centered dark field image showing strain fields.	110
53	Al-28 at.% Zn, 473K, 150 s. Ion thinned during 10 h. Spheroidisation is evident. Intensity curves produced by the electron beam traversing the line drawn through the square indicator mark. A. Zn x-ray intensity. B. Electron intensity that produced the picture.	112
54	Al-22 at.% Zn. a) treated and thinned identically as in fig. 53. b) 428K, 240 s and ion thinned. The decomposition of the depleted α' is clear. 200K \times .	113
55	a) Details of neighbouring lamellae #6 and #7. CBMD patterns for the microanalysis position are shown. b) Composition profile of lamellae #7.	117 118
56	a) ADF image of cell containing lamellae #8, imaged at 500K \times in b). Slight contamination of the position of analysis can be observed. c) Composition profile of lamella #8	119 120
57	a) BF image of reaction front containing lamella #9. CBMD pattern from this and from its lower neighbour are included. Note the parent grain spinoidal microstructure. b) CDF image with a product matrix reflection emphasizing the sharp change in diffraction contrast.	121

FIGUREPAGE

- c) The same reaction front imaged in "low mag mode" (objective lens off) with "parallel beam" microdiffraction patterns from the marked individual lamellae and from the parent grain. 122
- d) Composition profile of lamella #9. 123
- e) Individual x-ray spectra obtained at center ($z = 0$) and close to the edge ($z = 80$ nm) of lamella #9. 124
- 58 a) A well formed colony. Inset SADP are from parent and product grains. b) The same cell. The marked lamellae are shown individually with their composition profiles in Figures 59-61. 126
- 59 Lamella #1 and its composition profile. Grain boundary diffusion controlled steady state growth are not applicable to this case. 127
- 60 Lamella #2 and its composition profile. The steady state growth process is well characterized. 128
- 61 Lamella #4 and composition profile. Note the coarsened spinodal microstructure in the parent grain. 129
- 62 Lamella #5 and composition profile. The colony containing the lamella is shown in fig. 34. 131
- 63 a) A typical reaction front with steady state spacing. Note the precipitate at the interface which occurred after the preparation of the foil. b) The composition profile of lamella #10. 132
- 64 a) STEM BF image of lamella #17, b) Its concentration profile. 133
- c) BF image of colony containing lamella #17 CDF images with a product matrix reflection, fig. d), and with parent grain reflection, fig. e. 134
- f) "Parallel beam" image and microdiffraction pattern from each marked and neighbouring lamellae or from the parent grain. 135

<u>FIGURE</u>		<u>PAGE</u>
65	a) DIGM structure in Al-22 at.% Zn, 428K, 300 s b) Compositional STEM scan across the region shown in a).	136
66	a) BF STEM image of dealloyed zone resulting from DIGM in Al-12 at.% Zn, 428K, 300 s. b,c) CDF images showing the migration of the boundary.	138
67	Compositional STEM scan across alloyed zone. Note that Zn concentration in this case is closer to the equilibrium value, 0.035, than in the example in fig. 65.	139
68	Spinodal microstructure in Al-22 at.% Zn annealed 428K, 300 s and maintained at room temperature for 5 h. a) bright field, b) centered dark field images.	140
69	a) Coarsened spinodal microstructure in Al-22 at.% Zn after 478K, 300 s. ADF image. b) Area of microanalysis. 10 ⁶ ×. B.F. image.	141
70	a) Granular precipitation at a static grain boundary Al-22 at.% Zn. RT, 100 h. b) SADP sequence showing the low misorientation of the grain boundary.	142 143
71	Granular precipitation posterior to discontinuous precipitation when the last has lost mobility. Al-22 at.% Zn 423K, 300 s, RT, 125 h.	144
72	Low magnification SEM of microstructure resulting from ageing followed by dissolution treatment. a) Al-28 at.% Zn, 472K, 300 s + 615K, 10 s. b) Al-22 at.% Zn, 428K, 300 s + 595K, 10 s.	147
73	a) Illustrating that neither the favourable curvature of the grain boundary nor the dislocation content in the product cell has insensitized at this stage, the migration of the boundary. Bright field TEM micrograph, 10K ×. The SADP is from the product cell. b) A bright field (top) centered dark field (bottom) detail of the former reaction front.	148 149

<u>FIGURE</u>		<u>PAGE</u>
74	Bright field TEM image of the microstructure resulting from ageing and dissolution treatment: 478K, 300 s; 595K, 10 s. Despite the pronounced curvature of the grain boundaries (particularly at left), no retreating migration of these can be inferred. At this stage a high density of dislocations has resulted, although ineffective to induce the boundary to migrate.	150
75	a) STEM bright field micrograph of partially dissolved lamellar precipitates within two cells. 475K, 300 s; 593K, 10 s. b) Detailed view of the interfacial dislocation arrangement.	151 152
76	Illustrating an isolated partially dissolved lamella in bright field a); in CDF with a Zn reflection, b) and in the weak beam dark field mode, c) in order to narrow the width and enhance the contrast of the strain fields.	153
77	Bright field STEM micrographs illustrating the fact that the recovery process eventually can produce a tilt boundary in the depleted lamella. This is shown as a wall of edge dislocation in a) the same area is shown under different diffraction conditions in b)	154
78	A second example of the edge dislocation wall perpendicular to the screw dislocation walls. a) in bright field, b) in dark field mode. 478K, 300 s, 595K, 10 s.	155
79	Illustrating that the generated dislocations organize themselves into subcells. a) Bright field, b) centered dark field. 478K, 300 s; 595K, 10 s.	156
80	a) Bright field; b) centered dark field STEM micrographs showing the formation of subcells after 478K, 300 s, 590K, 11 s. c) Bright field micrograph of the same area under different diffraction conditions.	157 158
81	Schematic free energy-composition diagram demonstrating the driving force for discontinuous precipitation is reduced by spinodal decomposition in the parent grain at the ageing temperature T_A .	172

<u>FIGURE</u>		<u>PAGE</u>
82	Computed plots of $P\Delta G_{\text{chem}}$ vs. v . The numbers on the curves are values of S in nm Al-22 at.% Zn a) at 428K. b) 478 K.	173 174
83	Computed plots of $P\Delta G_{\text{chem}}$ vs. S , numbers on curves are values of v in nms^{-1} . a) 428K. b) 478K.	175 176
84	Computed plots of the net free-energy released, ΔG_{net} , as a function of cell velocity. Numbers of the curves are values of S in nm a) 428K b) at 478K.	177 178
85	Computed plots of ΔG_{net} as a function of lamellar spacing. Numbers of curves are values of cell velocity in nm. s^{-1} . a) at 428K b) at 478K.	179 180
86	Computed variation of the dissipation function, $\Delta G_{\text{net}} \cdot v$, with the cell velocity. Numbers of curves are values of S in nm. Al-22 at.% Zn. a) at 428K b) 478K	181 181

LIST OF TABLES

<u>TABLE</u>		<u>PAGE</u>
I	Electropolishing conditions	70
II	Probe sizes* and angles in the McMaster HB5 STEM	75
III	Ageing treatment	83
IV	Details of cells studied, 428K ageing temperature	115
V	Details of cells studied, 478K ageing temperature	116
VI	Comparison of measured with optimal values of cell velocity and interlamellar spacing	183

CHAPTER 1
INTRODUCTION AND SCOPE

Discontinuous precipitation is a solid-solid phase transformation resulting in the decomposition of a supersaturated solid solution α_0 in a structurally identical, but solute depleted, phase α' and a new β precipitate, behind an advancing grain boundary. The grain boundary then acts as a fast diffusion path, enabling the required composition change at temperatures too low for appreciable volume diffusion. Thus, for most cases, it can be considered that the moving grain boundary sweeps solute to the growing precipitate. The α' and β phases form cooperatively generating a duplex structure (Figure 1). The precipitate may form as lamellae or as rods. Due to this morphological characteristic, the transformation is also known as cellular reaction and explains why its theory has evolved in close contact with the theory of eutectoid transformation.

From both scientific and practical points of view, discontinuous precipitation reactions have been of interest for a long time. These are among the most intriguing solid state phase transformations; their full analysis involves consideration of interacting chemical, capillarity and friction

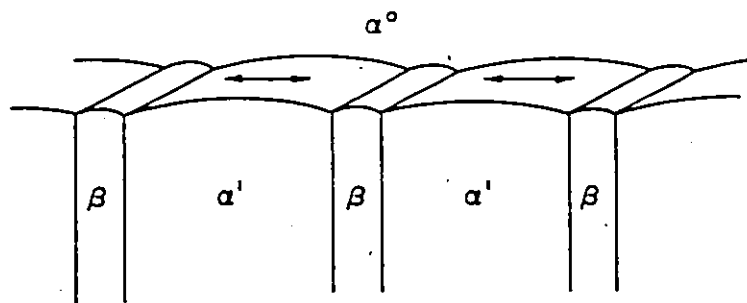


Fig. 1. Ideal discontinuous precipitation of β plates from supersaturated α_0 . The α'/α_0 boundary acts as a high diffusivity path.

terms, all focussed on a moving grain boundary-reaction front. In this regard discontinuous precipitation products differ from other lamellar microstructures (eutectic, eutectoid), most of which can be modeled on the basis of a local equilibrium hypothesis. In contrast, the non-equilibrium aspects of discontinuous precipitation are central to its quantitative description. From the practical point of view, the transformation is of importance since it often relates to the degradation of coherent precipitation hardening phases, wherein

an otherwise long-lived microstructure is discontinuously coarsened by the sweeping grain boundary. As a result the action is generally deleterious to the physical and mechanical properties of a wide range of alloys of commercial interest.

There have been many attempts to understand the basic processes involved in this mode of transformation. In addition, numerous experimental studies on discontinuous precipitation on various alloy systems have yielded an appreciable body of empirical facts. Nevertheless, despite outstanding theoretical contributions, there still remain important unanswered questions related to this reaction, which are in part of fundamental importance.

We shall examine previous models for initiations and for growth kinetics, along with relevant experimental investigations. The extent to which these theories can be tested has been limited essentially by the availability of high spatial resolution experimental information.

In this perspective, the present work attempts to investigate the kinetics of discontinuous precipitation by studying the resulting microstructure and microchemical distribution in the transformation product. The analysis is focussed mainly on the steady state growth process. Further discussion is centered on the diffusion-induced grain boundary

migration event as occasional precursor of the discontinuous process, and on the nature of the driving force. To gain insight into the reaction product characteristics, their post-dissolution microstructures are analyzed.

The alloy system chosen for this investigation, Al-Zn, permits an accurate high resolution X-ray microanalysis in the Scanning Transmission Electron Microscope (STEM). It is therefore an important aim of this work to directly measure the parameter of primary concern and the fine scale composition distributions for specific regions of individual colonies (cells) by means of CTEM and STEM techniques, thereby enabling a better comparison between theory and experiment.

CHAPTER 2

LITERATURE REVIEW

The fuller understanding of a recognized and well studied phenomenon begins with a comprehensive review of the relevant literature. In this section the proposed mechanisms for reaction initiation are briefly described. The more advanced growth models for discontinuous precipitation are summarized. Both theoretical and experimental contributions are reviewed in parallel. In addition, some important questions related to this mode of transformation are raised.

2.1 Occurrence of Reaction

Discontinuous precipitation can now be considered a fairly common event. Recent reviews on this subject^{1,2}, indicate that a wide variety of alloys undergo this kind of transformation; over 80 binary¹ and many ternary² systems are listed. For the first 25 years following its discovery³ in 1930 this precipitation mode was considered a curiosity. After this period, however, the annual number of publications has not ceased its increase¹.

There have been some attempts to rationalize the occurrence of discontinuous precipitation by determining the conditions under which it is favoured. An early suggestion⁴

concerning why the reaction was found in some alloys and not in others is that a minimum particle/matrix misfit of 1% is necessary before the reaction will occur. This implies that the matrix strain energy is a major driving force. The observation of the reaction in systems with much lower precipitate/matrix misfit such as in Al-Li (misfit Al₃Li-0.02%)⁵ does not support this idea. A closely related concept was proposed by Böhm⁶; it is based on the atomic matching, i.e. the difference in solute/solvent atom size and it was applied to Cu-base binary systems. The idea was that a mismatch of 12.5% or more was necessary to cause discontinuous precipitation (DP). The occurrence of DP in eg Cu-Co⁷ (mismatch 2.3%) rules out this criteria. Recently Meyrick⁸ postulated that the driving force for DP has its origin in the change of grain boundary energy with the degree of solute segregation. If this change is high enough, the increase in boundary energy resulting from grain boundary precipitation might be sufficient to induce the boundary to migrate in search of fresh solute. The results of Hillert's and Purdy's experiments⁹, in which grain boundary migration takes place during de-alloying or alloying in the absence of precipitation, has again indicated that the Meyrick proposition cannot be accepted as a general rule. It should be noted that the Meyrick and Böhm criteria are also related since segregation to grain boundaries is expected to increase with the solute/solvent mismatch.

In summary, there is no simple model capable of predicting, unequivocally, the occurrence of DP reactions. As will be seen in the following sections, there are a variety of factors playing a role in the events of D.P. The most important, perhaps, concern the grain boundary reaction front and the chemical supersaturation.

2.2 Initiation Mechanism

The initiation of discontinuous reaction is dependent on two main factors: the occurrence of heterogeneous grain boundary precipitation and the ability of the grain boundary to migrate. Hillert¹⁰ has suggested that the reaction can occur when there is a deviation from local thermodynamic equilibrium. This is illustrated in fig. 2 by means of free-energy-composition diagrams for the alloy matrix γ and the grain boundary B (regarded as thin film of boundary "phase" with its free-energy curve¹⁰). At the bottom of fig. 2 are schematics of the composition profile across the grain boundary of thickness δ . At the upper side of the boundary, the material entering the boundary is transferred to a higher free-energy state as illustrated by the arrow ΔG_u , while on the trailing side the same amount of material is leaving the boundary and being transferred to a lower energy state as indicated by the arrow ΔG_l . The imbalance is thus ΔG_p and it works in favour of pulling the boundary forward in the positive y direction.

The deviation from local equilibrium is thus zero for stationary grain boundaries. The natural question is hence

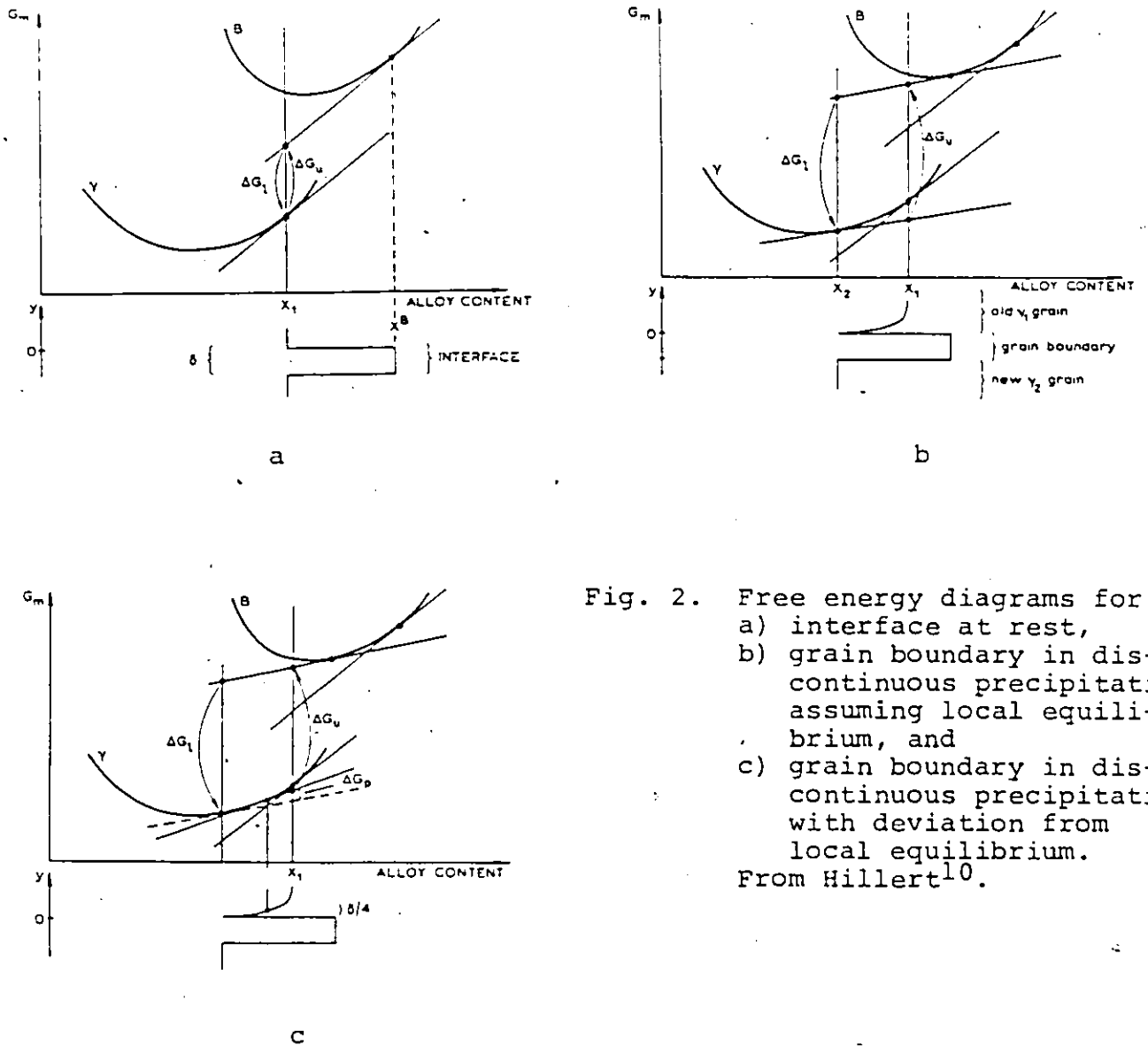


Fig. 2. Free energy diagrams for
 a) interface at rest,
 b) grain boundary in discontinuous precipitation assuming local equilibrium, and
 c) grain boundary in discontinuous precipitation with deviation from local equilibrium.
 From Hillert¹⁰.

how a stationary grain boundary gets its initial migration rate which leads to a small deviation from thermodynamic equilibrium. There are two relatively extreme approaches concerned with answering this question.

2.2.1 Precipitate induced boundary migration

The first model is due to Tu and Turnbull¹¹. They observed that the first step for cell formation in a Pb-Sn alloy is the nucleation of a β particle at the grain boundary. Further growth of β may be determined by the habit plane with one of the two adjoining grains. Tu and Turnbull supposed that the orientation relationship is that of minimum interfacial energy. The specific interfacial energy of β plate is different in the two grains. This imbalance can be eliminated by the migration of the grain boundary around the β plate in order to replace the higher-energy interface by the lower ("pucker mechanism"). This kind of boundary motion imbeds the β plate in one grain, the other being consumed by the first, leaving the precipitate attached to the grain boundary at its tip. During the course of boundary motion a second β plate may be formed lying parallel to the first one. In the same manner a third plate, a fourth and so on would appear successively, constituting a precipitation cell. This mechanism is illustrated sequentially in fig. 3.

Aaronson et al.^{12,13} extended the treatment of the

puckering mechanism by studying other related forms of precipitate/boundary interactions. Faceting of the grain boundary precipitate and the establishment of a local equilibrium geometry with the grain boundary are postulated to favour the mechanism.

A different form of precursor grain boundary precipitation in discontinuous reactions has been postulated by Lange and Purdy¹⁴. These authors have studied the initiation of cellular precipitation in Fe-Zn alloys and observed that the reaction is preceded by the nucleation, growth and coarsening of a metastable equilibrium grain boundary phase. It was deduced that a significant amount of volume diffusion must have occurred thereby reducing the local chemical driving force. Based on approximate stability calculations it was thought that the coarsening process itself can lead to grain boundary displacement of the appropriate magnitude through the abrupt release of portions of the grain boundary into regions of large and increasing supersaturation. Fig. 4 illustrates three stages in an hypothetical ageing sequence. The authors emphasize that this kind of behaviour is perhaps atypical for systems that will evolve to discontinuous mode of precipitation.

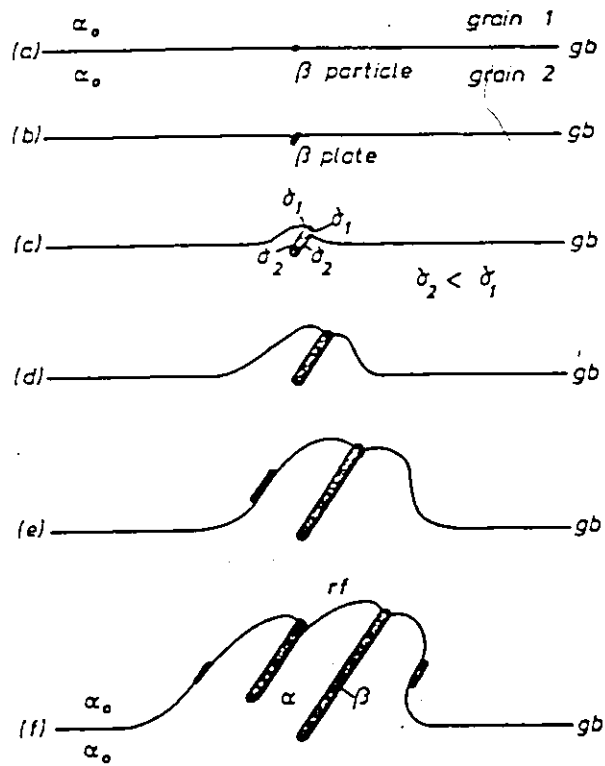


Fig. 3. The pucker mechanism for initiation reaction after Tu and Turnbull¹¹. For explanation see text.

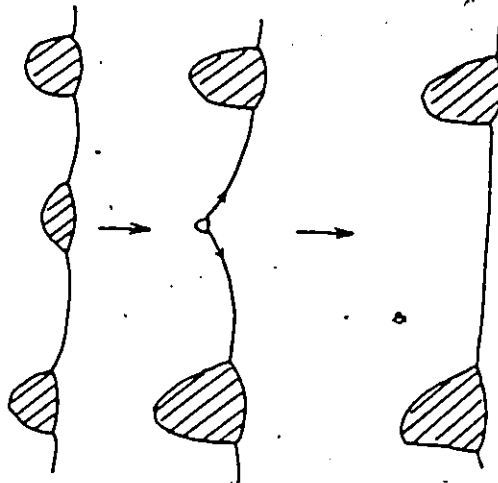


Fig. 4. Three stages in a possible aging sequence. In state 2, the equal size precipitates of stage 1 have coarsened, such that the outer precipitates have grown carrying the grain boundary forward with them. When the boundary is released from the center (shrinking) precipitate it will straighten abruptly. After Lange and Purdy¹⁴.

2.2.2 Precipitation on migrating boundaries

Fournelle and Clark¹⁵ considered the migration of a grain boundary due to its curvature and advanced a model for the development of a cell nucleus. The authors assumed that the migrating grain boundary depletes the area behind it of solute atoms by forming precipitates. Further migration of the boundary in the same direction is now favoured because of the composition gradient across the boundary, but is possible only if it bows between the precipitates. With further ageing the precipitates lengthen following the bowing reaction front. In this manner a lamellar discontinuous product is initiated. This model is illustrated in fig. 5. A clear distinction between this mechanism and that of Tu and Turnbull is that the precipitate/matrix orientation and habit plane is of little importance.

A literature survey indicates that, for a given alloy, it is quite unusual to be able to assign a unique mechanism for reaction initiation. Any system undergoing discontinuous precipitation may show characteristics of more than one mechanism depending on variables such as temperature. In the case of the Pb-Sn system it appears clear that the Tu and Turnbull mechanism operates. For Cu-Be it has been recently suggested¹⁶ that a modified version of the pucker mechanism operates at low ageing temperatures while at higher temperatures the precipitation may be preceded by boundary migration. Initiation of cellular reaction in Al-Li alloys¹⁷ has been explained

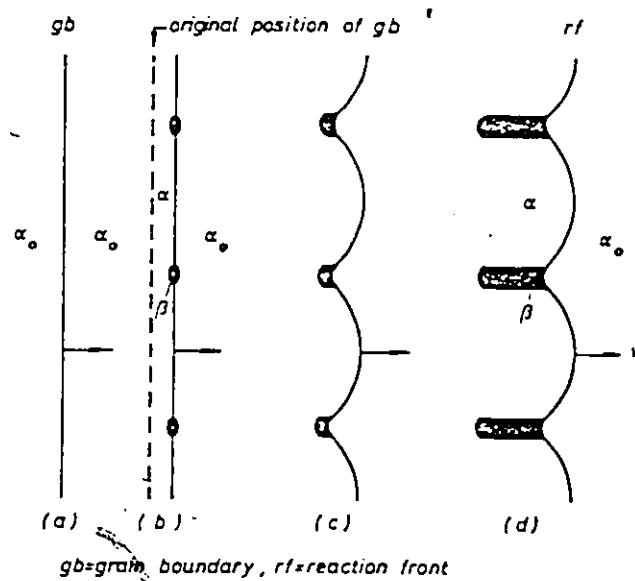


Fig. 5 Development of a precipitation cell after Fournelle and Clark¹⁵. For explanation see text.

by coupling the straightening of concave forward grain boundary (i.e. the critical component of the Fournelle and Clark model) with some competitive coarsening of matrix precipitates. An example of recrystallization-enhanced initiation of DP has been observed in Ni-Cu-Au²; prior to ageing the alloy was cold rolled 1%.

It is worthwhile to emphasize that the theoretical formulations and observations that account for reaction initiation, do not, in general, consider boundary structure. However this process must be affected by the structure of individual boundaries. More about this will be said later.

2.3 The Growth Process

2.3.1 The nature of the driving force

While it is clear that there is a chemical driving force for the precipitation process, the nature of the driving force for grain boundary migration has been the subject of wide conjecture. In this respect, Hillert and Langneborg¹⁸ have noted from the literature four possible sources of this local force:

- a) Stored energy, from plastic deformation, causes grain boundary migration at sufficiently high temperature. (Chronologically this was the first widely accepted mechanism¹⁹.)
- b) The new phase formed at the grain boundary has such an orientation relationship with one of the two grains that the surface energies may then favour the growth of this grain in contact with the precipitated phase²⁰.

- c) The concentration gradient in a depleted zone gives rise to coherency stresses if the lattice parameter varies with the alloy content. This may provide a driving force for the migration of the boundary into the stressed grain²¹.
- d) A driving force may be supplied thermodynamically if the grain boundary migration is sufficiently rapid to make the concentration profile so steep that there is a deviation from local equilibrium between the grain boundary material and the retracting grain¹⁰.

One can see that the suggested "forces" b) and a) above preceded the proposition of the Tu-Turnbull and Fournell-Clark initiation mechanisms, respectively. The force c) was proposed by Sulonen²¹ based upon the observation by Böhm⁶ (already mentioned in section 2.1); rather than invoking solute segregation to the grain boundary as did Meyrick⁸, Sulonen pointed out that there should be a concentration gradient in a thin layer of the retreating grain in front of the transformation front. He suggested that the¹⁰ accompanying coherency strain energy should give a driving force for the growth of the advancing (depleted) grain which would have a uniform solute content. Hillert²² has developed Sulonen's model in more quantitative terms, assuming that grain boundary diffusion is rate controlling, and emphasizing that even if lattice diffusion is not negligible, there may be a discontinuity in composition due to the coherency effect. The latter

point d) has been explored in detail by Hillert^{10,22} who suggested that the driving force is of a pure chemical nature and originates from a discontinuity in the alloy content at the migrating grain boundary. Kirkaldy²³ and Shapiro²⁴ earlier recognized the existence of a chemical driving force but associated it with the existence of a metastable miscibility gap. They were therefore able to treat the reaction as a monotectoid transformation²⁵. However, it is not common to find such miscibility gaps in systems undergoing discontinuous precipitation.

In recent years, the discussion of the driving force has been revitalized²⁶ mainly through the studies of Hillert and Purdy⁹ in 1978. They found that the same kind of boundary migration can occur without the interaction of a second condensed phase. Specimens of Fe or Fe-Zn alloys were treated in an atmosphere of a different Zn activity finding that the grain boundaries would migrate as a result of grain boundary diffusion of Zn into or out of the same specimens. They called the phenomenon chemically induced grain boundary migration, CIGM. However, based on some experimental findings²⁷, Cahn and Balluffi²⁸ have questioned the validity of this nomenclature. Instead they suggested that the driving force comes from the process of grain boundary diffusion itself and depends upon a difference in the diffusivities of the components in an alloy system. Consequently, they called the phenomena diffusion induced grain boundary migration, DIGM. They developed a mechanistic model coupling the climb of secondary grain

boundary dislocations with the transfer of atoms from one side of the boundary to the other. During the last 3 years, the phenomenon has been experimentally documented in other systems^{27,29-33}. The questions of whether the process is DIGM or CIGM resembles a cause/effect paradox. It is possible that the two approaches are not contradictory but rather complementary. How then can both be tied together? It has been recently suggested that the grain boundary experiences a vacancy supersaturation which may be responsible for coupling the chemical driving force with the migration of the boundary. The vacancy excess may arise from either a grain boundary or a bulk-Kirkendall effect³³. It is obvious, however, that additional experimental and theoretical work are necessary if the phenomenon is to be well understood.

2.3.2 Models for Growth kinetics

The diffusion-controlled growth rate of discontinuous precipitation in binary alloys has been treated by many authors over the years. In this section, some of the better-known models will be presented briefly, and in chronological order. Secondly, some important thermodynamical aspects will be pointed out.

- Zener³⁴ proposed the earliest model which assumed a volume diffusion-controlled reaction. This leads to the following expression for growth velocity

$$v = \frac{x_o - x_e}{x_o} \cdot \frac{2D_v}{S} \equiv k_1 \frac{2D_v}{S} \quad (1)$$

where x_o is the initial concentration in the parent matrix α_o and x_e is the equilibrium concentration in the depleted lamellae α' . D_v is the volume diffusivity and S the inter-lamellar spacing. Actually, there is scant experimental support for this theory³⁵.

Turnbull³⁶ modified Zener's formulation and obtained the first, very crude, kinetic expression based on interface diffusion-control, as

$$v = \frac{x_o - x_m}{x_o} \frac{\delta D_b}{S^2} \equiv k_2 \frac{\delta D_b}{S^2} \quad (2)$$

where δ is the boundary width and x_m the average (metastable) concentration in α' . Due to its simplicity, eq. (2) has been very widely used in experimental work seeking to evaluate the parameter δD_b in discontinuous precipitation (e.g. references 37,38) or in moving grain boundaries (e.g. ref. 39).

Cahn⁴⁰ considered that diffusion cannot be the only determining factor for the precipitation reaction and proposed a model which, in addition to grain boundary diffusion-control, assumes that the reaction front moves with a velocity proportional to the change in the Gibbs free energy. Cahn wrote the diffusion equation for the moving planar interface in a lamellar cell structure as:

$$D_b \delta \frac{d^2 x_b}{dt^2} + v(x_o - x_p) = 0 \quad (3)$$

with solution:

$$\frac{x_o - x}{x_o - x_3} = \frac{\cosh(\sqrt{a} z/S)}{\cosh(\sqrt{a}/2)} \quad (4)$$

where:

$$a \equiv \frac{vS^2}{k_c D_b \delta} \quad (5)$$

$k_c = x_p/x_B$ is the distribution coefficient which relates the equilibrium boundary composition x_B to the depleted lamellae compositions x_p , x_3 is the composition at the triple junction $\alpha_0/\beta/\alpha'$, v is the growth velocity and z is the coordinate perpendicular to both the growth direction and the plane interface α'/β with origin at the center line of the α' lamella. An essential consequence of Cahn's expression, eq. (4), is that it predicts a concentration profile in the α' lamellae which is higher in the middle as illustrated in fig. 6. It should be noted that, since the interlamellar spacing is, generally, submicron, detailed experimental information on the solute distribution over the width of the α' lamella requires high resolution microanalysis capability. In this connection, the only work reported in the literature is due to Porter and Edington⁴¹ and has proved to be a significant advance in the understanding of the discontinuous precipitation phenomena.

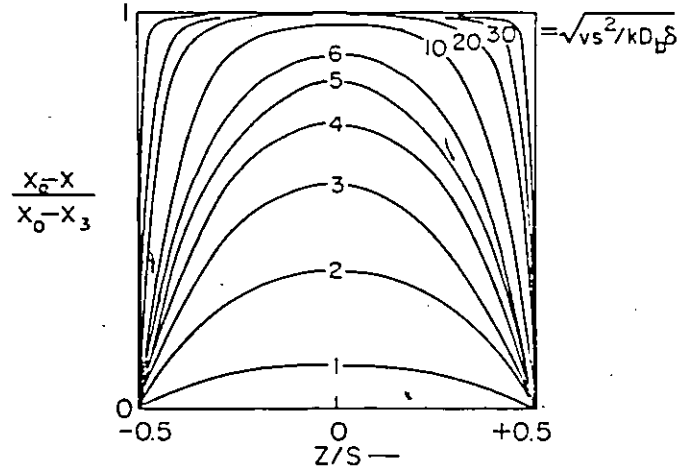


Fig. 6 Cahn's solution of the moving boundary diffusion problem. The numbers on the curves are values of the parameter a .

Aaronson and Liu's⁴² theory also used Zener's theory as its basis, while the relationship between v , S and D_b is derived more exactly than in the Turnbull model. Their analysis resulted in the useful expression:

$$v = 4 \frac{x_0 - x_3}{x_{m\beta} - x_0} \frac{D_b \delta}{S_\alpha \cdot S_\beta} \quad (6)$$

where $x_{m\beta}$ is the average (metastable) composition of the β lamella and S_β its thickness. With the use of the lever rule and upon several approximations the following equation is obtained:

$$v = 4 \frac{x_\beta - x_e}{x_\beta - x_o} \cdot \frac{D_b \delta}{S^2} \quad (7)$$

x_β and x_e are the equilibrium concentrations in the β precipitate and in the α phase respectively. If the relations $x_\beta \gg x_e$ and $x_\beta \gg x_o$ apply the concentration term in eq. (7) can be eliminated and one obtains:

$$v = 4 \frac{D_b \delta}{S^2}$$

which is to be compared with Turnbull's eq. (2).

Shapiro and Kirkaldy⁽²⁵⁾ proposed a model in which the reaction is considered as a metastable monotectoid reaction controlled by interface diffusion and obtained the equation

$$v = 48 \frac{V_m \gamma_{\alpha\beta} (K-1)}{q(0.5-p)^2} \cdot \frac{D_b \delta}{S^3} \quad (8)$$

Here V_m is the molar volume of the precipitated structure and p , q and K are thermodynamic parameters. The value of K is given by

$$K = - \frac{S \cdot \Delta G_c}{2\gamma V_m} \quad (9)$$

where ΔG_c is the change in the Gibbs free-energy and γ the specific interfacial energy of the α/β interface. K is there-

fore a ratio between the actual interlamellar spacing S and the critical spacing

$$S_c = 2\gamma V_m / \Delta G_c \quad (10)$$


as originally derived by Zener³⁴.

- Peterman and Hornbogen⁴³ used as their basis the recrystallization theory developed by Lüke⁴⁴. They found that the reaction front velocity can be expressed by the equation

$$v = - 8 \frac{\Delta G}{RT} \cdot \frac{D_b \delta}{S^2} \quad (11)$$

which contains explicitly the (overall) driving force term, ΔG .

- Sundquist⁴⁵ concerned himself in obtaining a more realistic solution to the moving boundary diffusion problem and considered the non-planar shape of the reaction front. He defined an angle θ between the growth direction and the normal to the local α_0/α' curved interface (fig. 7) and obtained the parameter



$$a_s = \frac{vS^2}{kD_b \delta \cos \theta_{av}} \quad (12)$$

which differs from Cahn's a parameter eq. (5) by the factor

$1/\cos \theta_{av}$ ($\cos \theta_{av}$ is the average value of $\cos \theta$ between the precipitate lamellae). Otherwise, Sundquist's and Cahn's solutions are identical.

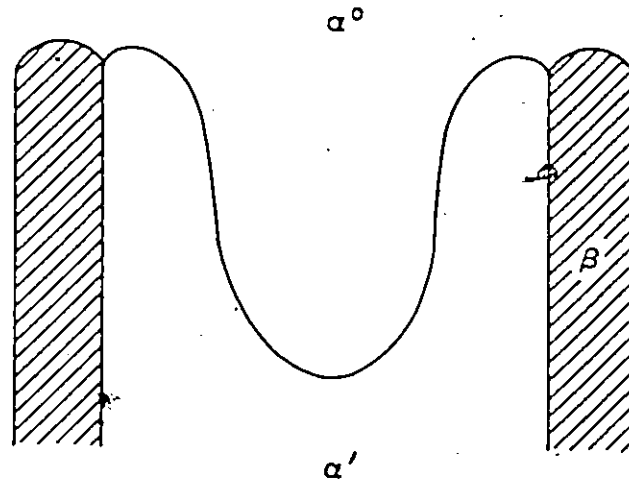


Fig. 7 A non-planar α_0/α' front of the type computed by Sundquist⁴⁵.

Perovic and Purdy⁴⁶ analyzed quantitatively a precipitate configuration different from the lamellar case so far discussed in this section. They extended the solution of the grain boundary diffusion equation to the formation of precipitates with radial symmetry, i.e. rods. Hence, the diffusion equation in cylindrical coordinates is of the form

$$D_b \delta \left(\frac{\partial^2 x_b}{\partial r^2} + \frac{1}{r} \frac{\partial x_b}{\partial r} \right) + v(x_o - x_p) = 0 \quad (13)$$

with solution

$$\frac{x_r - x_o}{x_p - x_o} = \frac{I_0(\sigma r) K_1(\sigma b) + I_1(\sigma b) K_0(\sigma r)}{I_0(\sigma a) K_1(\sigma b) + I_1(\sigma b) K_0(\sigma a)} \quad (14)$$

where I_0 and K_0 are the modified Bessel functions of zero order of the first and second kind respectively, and I_1 and K_1 are

their derivatives, a is the rod radius and $b = s/2$; the parameter σ is given by

$$\sigma = \sqrt{kv/D_b} \quad (15)$$

The other parameter has already been defined above, when Cahn's solution was presented. In fig. 8 it is shown the concentration profiles calculated by these authors for different σ values and for the case of $b \approx 10a$ which corresponds to their experimental condition in Cu-1.5 Co.

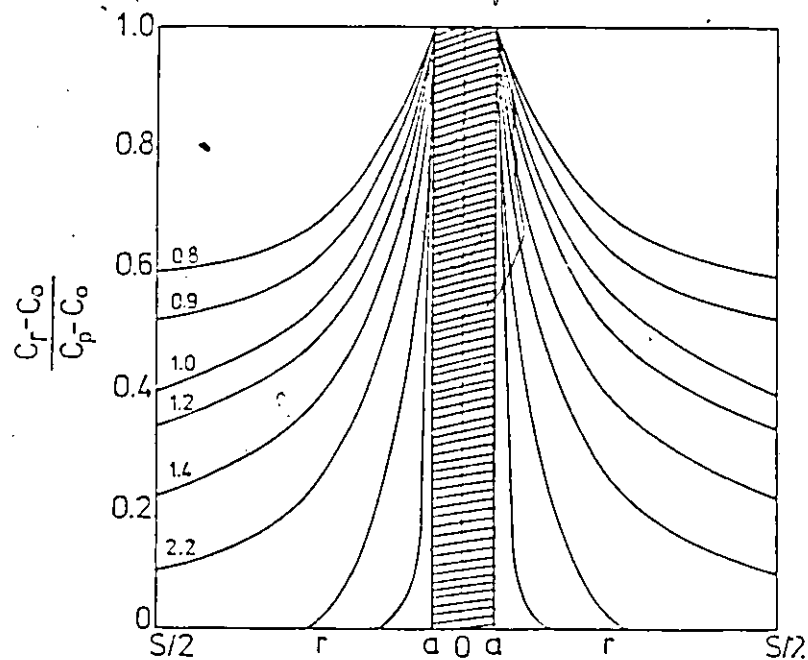


Fig. 8 Calculated concentration profiles for the case of grain boundary diffusion to a rod. The numbers on the curves are values of $\sigma(b-a)$. After Perovic and Purdy⁴⁶.

2.3.3 Thermodynamical treatment of the reaction front

It has been pointed out¹⁰ that both Turnbull and Cahn treated the growth process without taking into account the forces acting on the grain boundary. Consequently they do not provide a detailed indication as to how the reaction occurs. To give a more rigorous treatment to this phenomena requires taking into account the non-planar shape of the boundary and the effect of capillarity. This leads to a thermodynamical treatment of the local forces whose balance is presumed to determine the boundary shape. In this respect the work of Hillert¹¹ is central. In Hillert's formulation the grain boundary is treated as a separate phase with its own thermodynamic properties. A composition step (Δx) at the α_0/α' interface, which arises from the fact that boundary transport is much faster than volume diffusion, results in a chemical force (P_{chem}) available to induce boundary migration. This force, however, will vary locally along the interface since, for nearly planar shapes, Δx will take a minimum value at the center of the α lamellae, varying continuously to a maximum at the α_0/α' interface immediately adjacent to the β lamellae (as can be deduced from fig. 6). For dilute solutions this force is

$$P_{\text{chem}} = f \frac{\Delta G^{\text{diff}}}{V_m} \quad (16)$$

with

$$\Delta G^{\text{diff}} = RT \frac{(x_o - x_e)^2}{2x_o} \quad (17)$$

where f represents the fraction of this force available to move the boundary (since some volume diffusion may moderate the concentration profile), and is estimated as:

$$f = 1 - \exp\left(-\frac{vb}{2D_v}\right) \quad (18)$$

b is an interatomic distance, and the other terms have already been defined in the text. As a corollary, the chemical force induces the boundary to migrate against its curvature.

In addition to the chemical force, there may exist as well a capillary force which should result in migration of the boundary towards the center of curvature. Perovic and Purdy⁴⁶ envisage two kinds of capillarity forces:

- a) a general grain growth force arising from the initial curvature of the boundary
- b) a "traction force" due to the tendency of the growing precipitate to pull the boundary in such a shape that boundary curvature assists growth.

On combining the chemical force with that of capillarity Hillert¹⁰ proposes the following equation for the balance of forces acting at every point along the grain boundary, of a perfectly lamellar structure, moving with constant velocity:

$$\frac{\gamma}{\rho} = P_{\text{chem}} - \frac{v}{M} \quad (19)$$

where γ is the specific interfacial free-energy, ρ the local curvature and M the mobility. In this manner ρ , at any point

in the advancing interface, is such that all the forces balance each other. Hillert has devoted particular attention to the configuration at the $\alpha_0/\alpha'/\beta$ junction. It was assumed that the growth front is held back by the action of the surface tension $\gamma_{\alpha,\beta}$ in the α'/β interface which acts perpendicular to the growth direction. A fraction L is carried by the edge of the α' lamellae and the remaining fraction $(1-L)$ is carried by the edge of the β lamellae as shown in fig. 9. The value of L is, in principle, obtained from a geometrical construction based on the angles of tangency at the particular triple point. This approach has been maintained by Hillert over the years²² and has resulted in rather complex equations for the interlamellar spacing S , always containing the factor L . Recently, however, based on some approximations, a new version of his previous treatment has been offered⁴⁷ and simplified expressions for S have been proposed.

Equation (18), hence, balances capillarity (γ/ρ) with chemical force (P_{chem}) and friction (v/M). The relative predominance of P_{chem} or capillarity gives the different interface shapes. This has been recently discussed by Perovic and Purdy and is illustrated in fig. 10.

Sundquist⁴⁵ extended Hillert's¹⁰ analysis including several additional forces. In an attempt to understand the spacing in a lamellar discontinuous product, he proposes that, at some point, the boundary is required to take a non planar

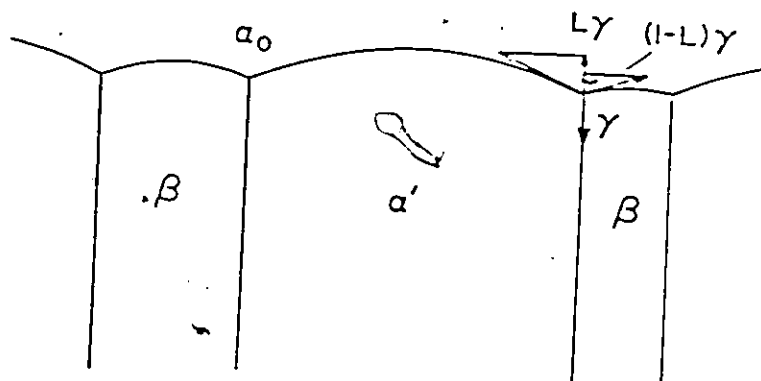


Fig. 9 Interfacial force balance at junctions in a lamellar discontinuous precipitation product¹⁰.

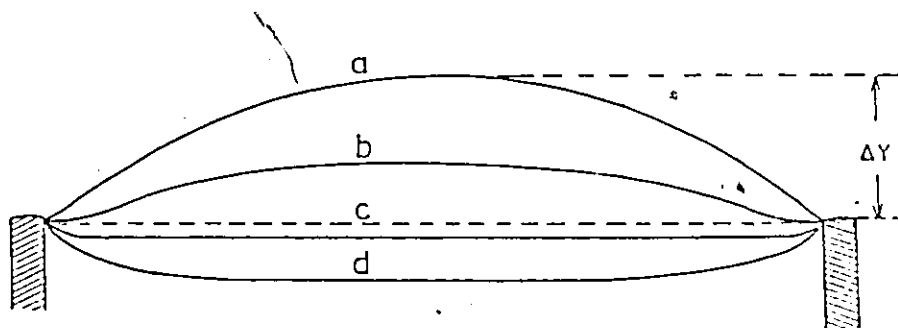


Fig. 10 Schematic shapes the grain boundary can take if a) the full chemical force acts in a high mobility boundary, b) the chemical force is partially offset by a friction term, c) no net force acts on the boundary, and d) precipitate traction aids boundary motion. From reference 46.

shape in order to maintain the steady state. The region of reversed curvature in the middle of the α' lamella, called a recess, is due to the absence of sufficient chemical force and acts as an ideal site for further nucleation of β and subsequent lamellae multiplication (recess mechanism, fig. 11). This point will be discussed in more detail in chapter 5.

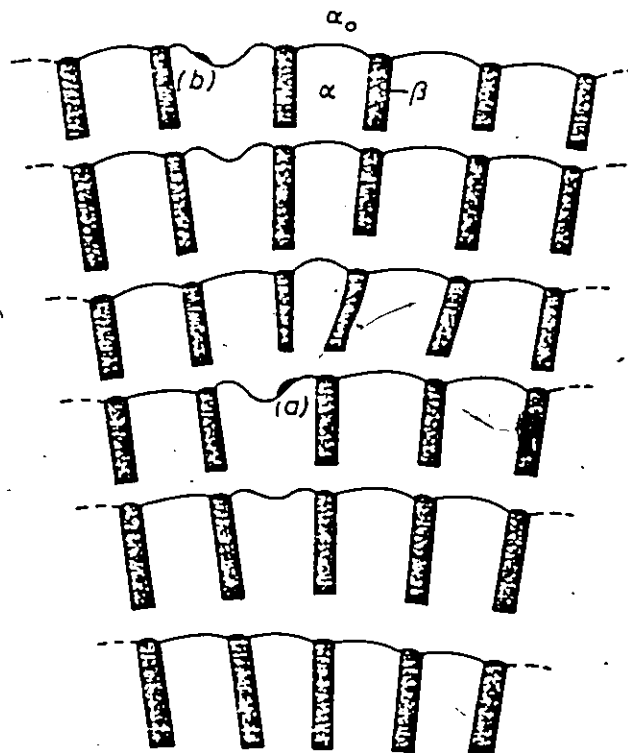


Fig. 11 Proposed mechanism controlling the average inter-lamellar spacing. After Sundquist⁴⁵.

A detailed thermodynamical study is due to Hillert²² who gave an individual treatment for each growing phase. Particular emphasis is placed on how the total free-energy available to drive the reaction is divided into many parts, each part serving a particular purpose. This is schematically shown in fig. 12. The shortcomings to Cahn's theory⁴⁰ are

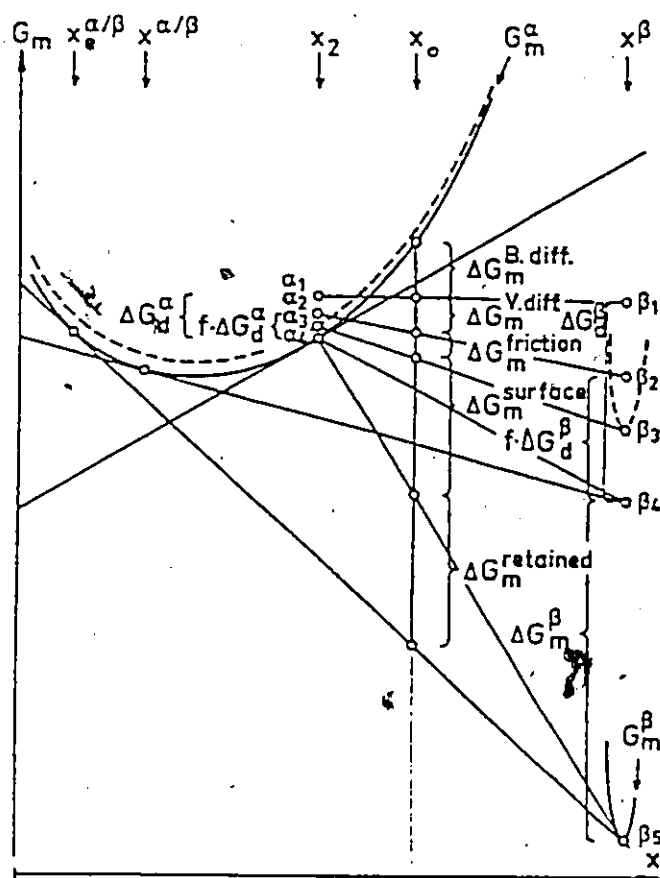


Fig. 12 Free-energy diagram for discontinuous precipitation showing the various sinks for the total driving free-energy, as proposed by Hillert²². The dashed curves apply for the growing α and β phases, x_2 is the composition of the boundary material and of the growing α' phase.

pointed out, particularly Cahn's approximation $x_3 = x_e^{\alpha/\beta}$.
 Indeed, Hillert's theory²² predicts $x_3 \approx x_e^{\alpha/\beta}$ only when cell boundary mobility is very low and most of the driving force for the reaction is consumed in overcoming friction losses.

From the preceding discussion one can appreciate that the non-equilibrium aspect of discontinuous precipitation is essential for its quantitative description. Due to the incompleteness of solute segregation, only a fraction P ($0 < P \leq 1$) of the available ΔG_{chem} is expended during the steady state process. The factor P can be calculated with the aid of equation 4 and integrating the actual Δx along the full width of the α' lamellae. Cahn⁴⁰ first recognized the importance of this factor and obtained for dilute solutions the equations

$$P(a) = \frac{3}{\sqrt{a}} \tanh\left(\frac{\sqrt{a}}{2}\right) - \frac{1}{2} \operatorname{sech}^2\left(\frac{\sqrt{a}}{2}\right) \quad (20)$$

which allows accurate evaluation of the residual supersaturation, $(1-P)$, in α' . While some workers have contented themselves with obtaining values of v and/or S , through average measurements, and have assumed that equilibrium is reached^{37,38,49,50}, others have made an estimate of the average supersaturation in α' ,^{25,51-56}. These estimates have generally been obtained by x-ray diffraction measurements of lattice parameters in bulk specimens and hence some average solute concentration. Conse-

quently such details as concentration profiles have not been provided by this method; the information obtained is in fact more subject to error due to volume diffusion behind the reaction front.

In view of the definition of the parameter a , equation (5), P is determined by the set S , v and $D_b \delta$. Indeed the diffusion equation provides only a relationship between S , v and the degree of segregation. Therefore, for a given spacing, there is a range of velocities within the limits imposed by the thermodynamics. What, then, determines the spacing? No detailed investigation has been devoted to answering this question. Cahn⁴⁰ has postulated that the reaction takes place with that S which maximizes the rate of decrease of free-energy. Puls and Kirkaldy⁵⁷ proposed that the system chooses S which maximizes the entropy production.

Summarizing this section, we differentiate two major categories of theory concerned with the description of discontinuous reactions: a detailed type of analysis as developed by Hillert^{10,22,47} (and Sundquist⁴⁵) and, on the other hand, a global approach due to Cahn⁴⁰ and to Puls and Kirkaldy⁵⁷. The study of the precipitation process has benefitted from the availability of exact solutions for the formation of either plates^{40,45} or rods⁴⁶. From the experimental point of view, however, close comparison with the theory has been initiated only recently⁴¹, with the advent of high resolution micro-analytical instruments.

2.4 Reaction Morphology

2.4.1 Reaction classification

In a review paper, Hornbogen⁵⁸ proposed a classification in which discontinuous precipitation is included as one of six different discontinuous transformations because they make use of grain boundaries as reaction fronts. Furthermore, grain boundary D.P. reactions possess singularities that deserve their own classification. Although there are numerous characteristics which differentiate some systems from others, there has been no rigorous classification in the published literature. The presence of general precipitation in the matrix is an important factor and on this basis Thompson⁵⁹ proposes the following classification:

Type 1: $\alpha_0 + \alpha' + \beta$

This is the type discussed so far. No general precipitation takes place. It is difficult to find a system undergoing this type of reaction. However, it has been suggested that an example may be Mg-Al⁴¹.

Type 2: $\alpha_0 + \beta + \alpha' + \beta'$

wherein there is a competitive general precipitation ahead of the discontinuous growth front. β is a prior matrix coherent precipitate which transforms to coarser lamellae or rods.

Examples of this type happen in Al-Li¹⁷ and Cu-Co⁴⁶.

Type 3: $\alpha_0 + \delta \rightarrow \alpha' + \beta$

in which a coherent metastable δ phase transforms into a more thermodynamically stable β . Cu-Be and Al-Zn alloys fall into this category. In general, precipitation ahead of the discontinuous growth front will reduce the free-energy available for DP by an amount which is difficult to estimate.

2.4.2 Micromorphology

As mentioned in the previous section, all the theories of discontinuous precipitation are based upon ideal characteristics: a perfect lamellar morphology with a near-planar reaction front and constant interlamellar spacing. However, a survey of the published micrographs shows that it is far more usual to find the reaction front being anything but planar and the interlamellar spacing showing significant variations, even within individual cells. This latter aspect has received comparatively little attention. The work of Gust and co-workers⁶⁰, however, shows that a range of spacings exists within a given specimen and that their distribution is adequately described by a Gaussian. Variations in interface shapes were observed in discontinuous rod formation in Al-Zr by Nes and Billdal⁶¹ who then applied Hillert's model to conclude that this effect is due to a force of the precipitate pulling the boundary and so reducing the interfacial energy. It is worthwhile to recognize here that the thermodynamical analysis for discontinuous

precipitates in rod morphology is more difficult than the lamellar case. This is because of the extra capillary term associated with the cylindrical curvature of the precipitate which, in turn, influences the equilibrium composition of α' in contact with β , as expressed by the Gibbs-Thompson effect. That is to say ΔG_{chem} is dependent on the rod thickness.

Other morphological variations have been reported. Perovic⁷ showed that the discontinuously transformed product presents rod particles as well as columns of spherical precipitates. These latter spheres are thought to form as a consequence of Rayleigh instability. Ainsley et al⁶² have found that in Fe-Mn-V alloys discontinuous fibres precipitate associated with high coincidence site density planar boundaries; in contrast, particle precipitation and non planar growth are associated with boundaries of poor fit.

2.4.3 Macromorphology

From a more macroscopical point of view, the migration of the grain boundary associated with the reaction develops a single and/or double seam morphology, i.e., as the growth process takes place only in one direction or in more than one direction, respectively. This aspect has been studied by Bauman et al¹⁶ who proposed that the lower ageing temperature generally leads to a double seam morphology while the high temperature leads to a single seam fashion. The double seam is, according to these authors, originated by the pucker mechanism¹¹ and formed via an "S"-mechanism proposed indepen-

dently by Frebel and Shank⁶³ for discontinuous precipitation and by Fournelle⁶⁴ for the case of discontinuous coarsening (figure 13). The distinction between higher or lower temperature is related to half of the absolute melting point of the alloy, $T_m/2$. Consequently, the formation of a single seam is thought to be initiated by the thermal migration of the boundary, preceding grain boundary precipitation, and the authors seek support in these observations for high temperature initiation as proposed by Fournelle and Clark¹⁵.

It is perhaps pertinent to mention as a morphological feature, the ways in which lamellae (or rod) multiplication might be accomplished. These fall into two categories: lamellar branching and repeated nucleation of new lamellae at the advancing interface, as represented schematically in figure 14. Several workers have reported observations of branching lamellae^{15,37,66} or rods⁶¹. In contrast, observation of repeated nucleation during isothermal growth (as proposed by Sundquist) has not been reported, although it has been suggested⁶⁷ that it may operate in the Cu-Ti system, where the precipitate habit plane is rigidly defined so branching is energetically unfavourable. Nonetheless, it must be considered that in any two-dimensional microscopic technique, it is very difficult to distinguish repeated nucleation (during isothermal ageing) from sectioning effects.

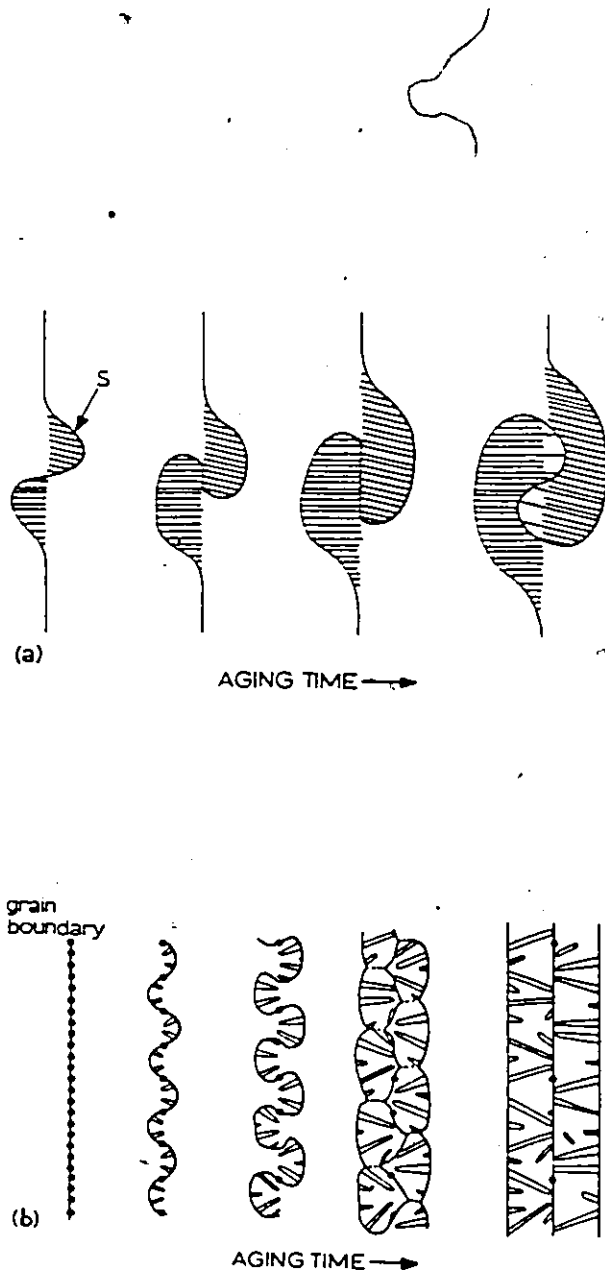


Fig. 13 a) Schematic diagram of S-mechanism, after Fournell⁶⁴
 b) Development of double seams via S-mechanism,
 after Frebel and Shenk⁶³.

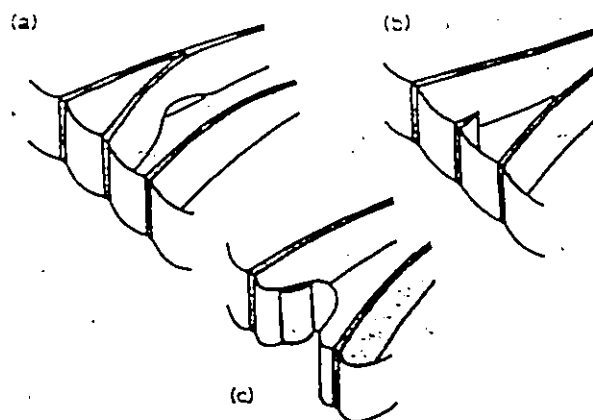


Figure 14 - Possible mechanisms for lamellae multiplication during discontinuous precipitation: a) branching, b) repeated nucleation on cell boundary, c) nucleation in recess of cell boundary. After Butler⁶⁵.

In summary, at present there are reasonable mechanisms to account for the macroscopic morphological variations with some limited evidence for the factors which influence them. Contrarily, the observed microscopic morphological variations both within individual cells and at the matrix/cell interface are far from fully clarified. Current evidence points to the fact that the characteristics of individual colonies are dependent on two key factors; the driving force available in a particular system and the characteristics of the grain boundaries where the reaction is taking place.

2.5 Effect of Grain Boundary Structure on Kinetics

Since discontinuous precipitation occurs with high angle grain boundaries, a brief account for these boundaries is appropriate here. Judging from recent reviews on the topic⁶⁸, a comprehensive description of a grain boundary is a particular and difficult task. For the present purpose, a grain boundary can be conceived as a thin slab⁶⁹, having a general structure which can be understood through geometrical modelling⁷⁰ and which accounts for properties such as energy, impurity segregation level and diffusivity⁷¹. Grain boundary diffusion on its own exhibits anisotropy as recently reviewed by Peterson⁷². Indirect evidence for this effect, in Zn diffusion along well characterized grain boundaries in Al, has been presented by Herbeuval et al⁷³ whose results are shown in figure 15.

The recent contributions of Balluffi^{74,75} have particular relevance to the discussion of the conjugate grain boundary structure-diffusion-migration. A central role in Balluffi's model⁷⁴ is assigned to the climb of secondary grain boundary dislocations as the sources/sinks for the point defects necessary for atomic transport. The model has been extended for application to the mechanisms operating during DIGM²⁸. Although DIGM is a recently recognized phenomena, Purdy⁷⁶ has reviewed its characteristics and examined the areas of uncertainty. For instance, considering that diffusion is a structure-sensitive

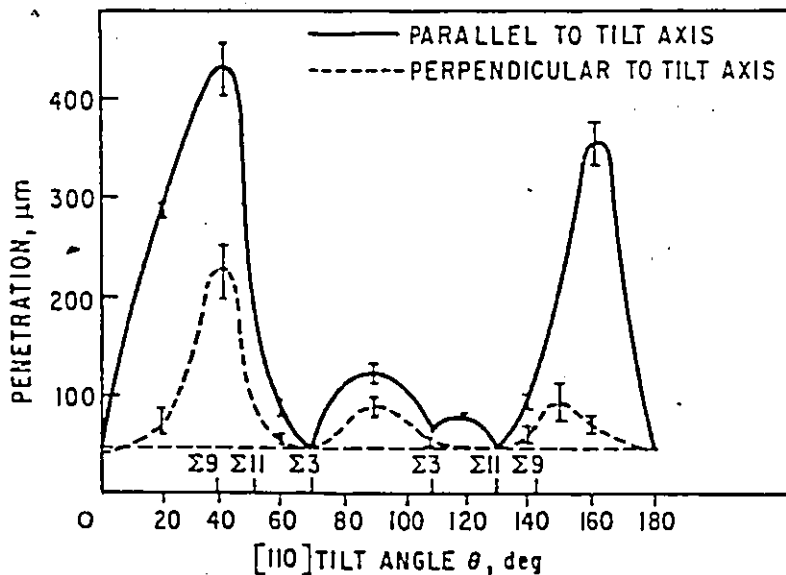


Fig. 15. Penetration depth of Zn along $[110]$ tilt boundaries in Al at 250°C as function of misorientation angle. After Herbeval et al.⁷³.

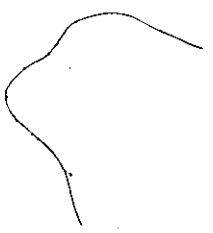
process, then it is obvious that the rates of grain boundary diffusion will depend upon the parameters that determine the structure. With this premise Hillert and Purdy⁹ postulated that a grain boundary which, as a result of DIGM, is found to depart from its (local) equilibrium configuration may therefore be characterized by a set of structural parameters not typical of the majority of grain boundaries in the annealed polycrystal⁷⁶. That is to say: the structure of migrating

grain boundaries is not the same as that of stationary ones.

A further major question concerning DIGM relates to enhanced grain boundary diffusivity. The first study due to Hillert and Purdy⁹ in Fe-Zn measured diffusivities in DIGM 2 and 4 orders of magnitude higher than in discontinuous precipitation⁵⁴ and in stationary grain boundaries in the same system, respectively. About the same level of enhancement of $D_b \delta$ in moving boundaries has been reported by Smidoda, Gotschalk and Gleiter³⁹ and by Hillert and Li³⁰. The original conclusion⁹ was that grain boundary diffusivity is greatly enhanced by its motion. However, recent experimental work of Gust et al⁷⁹ suggests the inverse. These workers measured diffusion penetration of indium in static grain boundaries in nickel bicrystals and found very large values of $D_b \delta$ (comparable with those obtained by Hillert and Purdy and by Smidoda et al) suggesting that DIGM may occur at high energy and therefore high diffusivity grain boundaries.

On the other hand, precipitation on grain boundaries has been proved to be influenced by the inclination⁷⁸ and misorientation of the boundary^{79,80}, the orientation of the grain boundary plane with respect to the habit plane of the precipitate and the existence of grain boundary steps or ledges⁸¹. All these factors account for the observed very widely different distributions of precipitates from one grain boundary to another in the same sample. In this regard, the detailed, high resolution electron microscopy investigation

undertaken by Gronski and co-workers⁸²⁻⁸⁴ is of interest. Studies of the relationship grain boundary structure vs. grain boundary precipitation in Al-Zn and Al-Zn-Mg alloys⁸² have indicated that intrinsic grain boundary defects have significant effects on the precipitation sequence and that a hierarchy of structural influences exists. In an attempt to determine the exact correlation of grain boundary structure and nucleation in these alloys, a high resolution microanalysis was performed in order to study the behaviour of Zn solute in Al bicrystals⁸³. Specimens subjected to short annealing times at 500°C are found to exhibit a periodic distribution of Zn along the g.b. plane prior to the appearance of any evidence for precipitation itself. The authors noted that the segregation periodicity bears no relationship with the transition lattice models of boundary structure but its behaviour as a function of misorientation angle does agree with the expected intervals of atomic relaxation in the O-lattice, Figure 16. (the same diffusion system at lower temperatures and extensive annealing times undergoes DIGM³³). Smith noted earlier⁸⁵ that discontinuous precipitation did not occur on twin boundaries because coincident site positions prevent precipitate nucleation. Hornbogen⁵⁸ later proposed that discontinuous growth and not precipitate nucleation is retarded because of low mobility at twin interface.



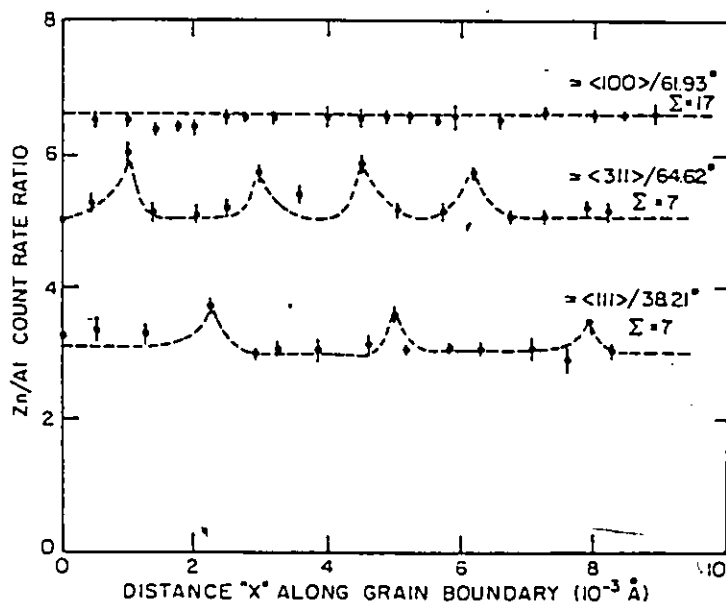


Figure 16 - Plot of the Zn/Al count rate as a function of distance along the grain boundary plane for 3 bicrystals, classified by their axis/angle pair. After Briceno-Valero and Gronski⁸³.

The heterogeneity of discontinuous precipitation rates is a common feature in many alloy systems. Melton and Edington⁸⁶ attributed the observed variations in growth rate in an Al-Zn alloy to the temperature dependence of the boundary mobility (rather than to the misorientation). Porter and Edington⁴¹ also found the kinetics of discontinuous precipitation in Mg-Al strongly dependent on grain boundary characteris-

tics. They performed high resolution microanalysis, using electron energy loss spectroscopy, on individual segments of cells and found different composition profiles. How these profiles are related to the characteristic of the particular reaction front was not explained. Frebel and Shenk⁶³ reported that in Fe-Au there was a tendency for the reaction to be inhibited at boundaries with high density of coincident sites (low Σ) and concluded that the grain boundary influences both kinetics and morphology. In an Fe-Mn-V alloy Ainsley et al⁶² also concluded that precipitate morphology depends on the structure, indexed by Σ , and curvature of the boundary, although their experimental data indicates that at low Σ boundaries, the growth rate was fastest.

The effects of structure-sensitive grain boundary properties on discontinuous precipitation are obviously not simple. If boundary diffusion is not a limiting factor, then the growth rate may be determined by boundary mobility. Conversely, if boundary diffusion is a limiting factor, then low CSL boundaries, although able to move more easily^{87,88}, may not supply enough solute to generate the necessary chemical driving force.

In an attempt to obtain a better understanding of the influence of grain boundary structure on D.P., Gust and co-workers⁸⁹⁻⁹¹ have started a systematic investigation of this reaction in synthetic Cu-In bicrystals of known and predetermined misorientation^{90,91} and in naturally grown tricrystals of Ag-Cu. Their results show that the morphology, the growth

velocity, the interlamellar spacing and the activation energy, depends on both the misorientation of the two neighbouring crystals and on the inclination of the grain boundary plane. More recently Wirth and Gleiter⁹², attempted to investigate the effect of the atomic structure at the reaction front on discontinuous precipitation resulting from sintering experiments in Cu-Ag. Their conclusions are similar to those of Ainsley et al with respect to the relationship between λ and the degree of precipitation but they propose that a structural transformation in a static boundary is a prerequisite in order for it to become a discontinuous reaction front. This idea was extended in a second paper⁹³ in which is reported the effect of pressure on discontinuous precipitation in the same system. The reaction rate was found to decrease at high pressures (about 10^9 Pa) by about two orders of magnitude, depending on the temperature. However, no significant effect on crystallography and on morphology, particularly on lamellar spacing, was reported. The authors assume that the transport of an atom along or across the reaction front interface requires a local free volume fluctuation. With increasing pressure this fluctuation occurs less frequently. Thus, the idea of a pressure-impeded structural transformation of the boundary seems consistent with the reported constant lamellar spacing at high and low pressures.

2.6 Dissolution of the Discontinuous Product

This subject has received less attention than the isothermal growth process. It is expected that volume diffusion will control the dissolution process at high temperature ranges⁹⁴, but in some cases the alloy solvus temperature, T_s , may be low enough for the short circuit effect of boundary diffusion to predominate in dissolution at temperatures around T_s . Only a few experimental studies have been reported in the literature. These are, nonetheless, summarized, again, in chronological order.

- Sulonen⁹⁵ provided the first evidence for discontinuous dissolution in Cu-Cd alloys in a range of temperatures above and below, but close to, T_s . He studied the dissolution kinetics, applying the Johnson-Mehl-Avrami equation and by means of quantitative metallography. It was also shown that at $T = T_s + 20$ K the process is volume diffusion controlled.
- Larikov and Yurchenko⁹⁶ submitted to prolonged annealing at $T > T_s$ discontinuous microstructures in Ni-Be and in Pb-Cd single crystals. The information deduced from this paper is that the precipitate dissolution is volume diffusion-controlled and involves some period of recrystallization.
- Bogacheva et al⁹⁷ report a similar kind of experiments in Cu-Ti, and in Fe-Ni-Ti, and also similar observations. With the second alloy, however, discontinuous dissolution occurs at

970°C but is rapidly overcome by continuous mode of dissolution.

Tu and Turnbull^{98,99} have investigated the dissolution of lamellar precipitates in a Pb-Sn alloy. This investigation was quite detailed, and has been correlated with their previous studies on discontinuous precipitation in this system. It was shown, by optical microscopy, that the cell boundary, acting as a fast diffusion path, recedes, thereby dissolving the precipitates. A critical temperature, T_{cr} , defined as the temperature at which the receding boundary ceased moving, was found to exist slightly below T_s , figure 17. Con-

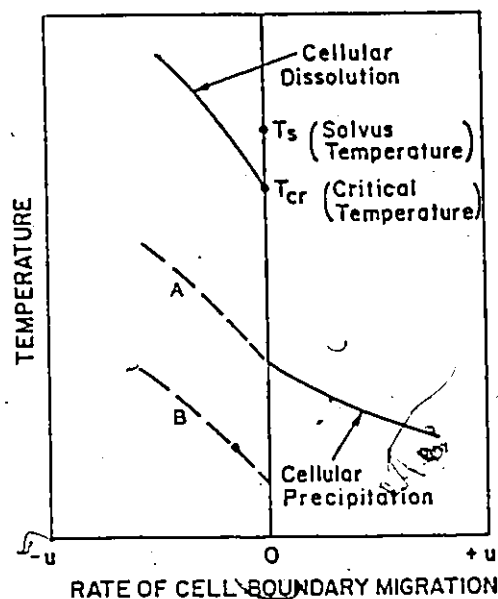


Figure 17 - Schematic curves of cellular reaction rate vs. temperature, after Tu⁹⁹.

sideration of this fact was central in their analysis of the balance of forces on both sides of the cell boundary at the critical temperature. It should be stressed that, in the Pb-Sn alloys under consideration, at $T = T_{cr} < T_s$ there exists thermodynamic conditions appropriate for discontinuous precipitation. Tu and Turnbull⁹⁸ obtained the following equation which in principle permits the estimation of the upper bound for the interlamellar surface energy $\gamma_{\alpha\beta}$:

$$\gamma_{\alpha\beta} < \frac{SRT_{cr}}{2V_m} \left\{ x_o \ln \frac{x_e}{x_o} + (1-x_o) \ln \frac{(1-x_e)}{(1-x_o)} \right\} . \quad (21)$$

Equation (21) is the result of equating the chemical free energy, assuming ideal solution behaviour, with that spent in creating the interfaces involved at T_{cr} . $\gamma_{\alpha\beta}$ is therefore extremely sensitive to the accuracy in determining T_{cr} . Gupta¹⁰⁰, taking advantage of the migration of the boundary involved in discontinuous precipitation, promoted a grain refinement in Cu-In alloys through thermal cycling: precipitation in the $\alpha+\delta$ region followed by dissolution in the α region. The dissolution process was evidently volume diffusion controlled. Referring to the Tu and Turnbull's publication, cited above⁹⁸, he expected but did not show, discontinuous dissolution to take place in this alloy at $T < T_s$.

Frebel and Shenk¹⁰¹ have found polygonization and recrystallization accompanying precipitation and dissolution in Au-Fe.

Discontinuous precipitation in this system is controlled by volume diffusion³⁵. The authors proposed that lattice defects produced by the growing α Fe plates are the reason for the observed recrystallization phenomena.

- Gust and coworkers^{102,103} have also explored in the dissolution of discontinuous precipitates. Cu-Cd alloys were studied as well as Cu-Sb single crystals. In the latter¹⁰³, although their micrographs do not show a receding reaction front, they treated the problem as discontinuous dissolution, and compared their extracted results with diffusivities for migrating grain boundaries published by other authors^{9,30,39}. In both cases the dissolution temperature was close to T_s .
- Pawlowski and Truskowski¹⁰⁴ treated an as cast Al-Zn alloy at temperatures where discontinuous precipitation is known to occur^{37,86,105} and anneal them at two higher temperatures, 50K and 90K above T_s . These authors used a variety of experimental techniques such as x-ray diffraction, microhardness tests and electron microscopy and interpreted their results as supporting the mechanism of discontinuous dissolution at $T < 360^\circ\text{C}$ (i.e. $T < (T_s + 50\text{K})$). The critical temperature, as defined by Tu and Turnbull⁹⁶, was estimated, extrapolating a 2-point curve, as 295°C ; then, applying equation (21) they obtain $\gamma_{\alpha\beta} = 120 \text{ erg/cm}^2$, a value smaller by a factor of 4 than the measured $\gamma_{\alpha\beta}$ for lamellar interfaces in this system^{66,106,107}. At 295°C the alloy is in the miscibility gap

$\alpha'+\alpha$ " and therefore no driving force for β precipitation could exist. In consequence the use of eq. (21) is not justified.

2.7 The Role of Interfaces; Some Thermodynamical and Structural Aspects

It is now well recognized that interfaces constitute an integral part of the structure of materials, and so they enter directly into the structure/property/performance linkage which constitutes the central theme of material science and engineering¹⁰⁸. Particularly, in discontinuous precipitation interfaces play an important role in both the thermodynamics and kinetics of the process. In this section, rather than a comprehensive account, some aspects pertinent with the scope of the present investigation will be underlined.

2.7.1 Interfacial equilibria

Our problem is situated in the context of precipitation from supersaturated solid solution. This subject has been reviewed many times (e.g. references 109-111) and treated under particular perspectives (e.g. references 112-115). Precipitation can occur via spinodal decomposition¹¹⁶ or by the nucleation and growth mechanism. In the former case no interface effects are involved but in the latter the formation and motion of an interface are the essential features of the transformation. The classical theory of nucleation requires that, in order to reduce the activation energy of the process, the nucleus forms

with the minimum possible surface energy per unit volume of precipitate. It is customary to consider two cases:

- a) Precipitation homogeneously in the matrix. A precipitation with isotropic interfacial energy γ simply requires a spherical nucleus shape by the Gibbs-Wulff theorem^{114,117}. In the usual cases of solid state precipitation, however, where the two phases have different crystal structures, a low-energy interface occurs only, for particularly well matched planes or directions. As a result a relative orientation relationship between the two phases is established. Figure 18 (Speich and Oriani¹¹⁸) shows the expected variation of γ as a function of the interface orientation, γ -plot, for a BCC-BCC (Cu-Fe) system where a sharp γ cusp at the low γ orientation corresponds to the close packed direction $\langle 111 \rangle_{\text{BCC}}$ and $\langle 110 \rangle_{\text{FCC}}$. In general the precipitate/matrix interfacial structure at the cusp orientation corresponds to a fully, or in some cases, partially coherent (misfit dislocation containing) boundary. For the other part of precipitate/matrix interface in the required OR, there is a poorer atomic fit. It has been shown that even across β/γ Cu-Zn boundaries, where the difference in crystal structure is small, faceting is preferred to continuous curvature, and occurs at several orientations¹¹⁹.
- b) Heterogeneous precipitation:

Nucleation can also occur heterogeneously at grain boundaries, on dislocations or even on preexisting zones^{120,121}. Figure

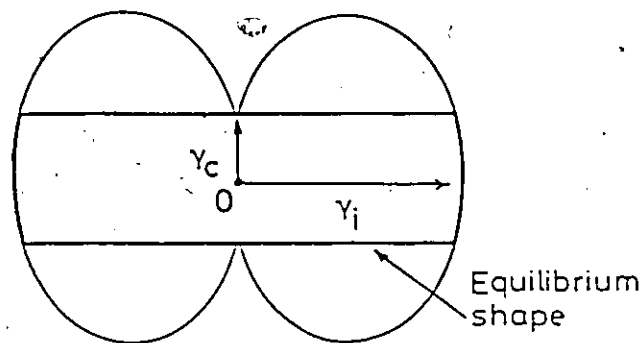


Fig. 18 A section through a γ -plot for a precipitate showing one coherent interface, together with the equilibrium shape (a disc). From ref. 151.

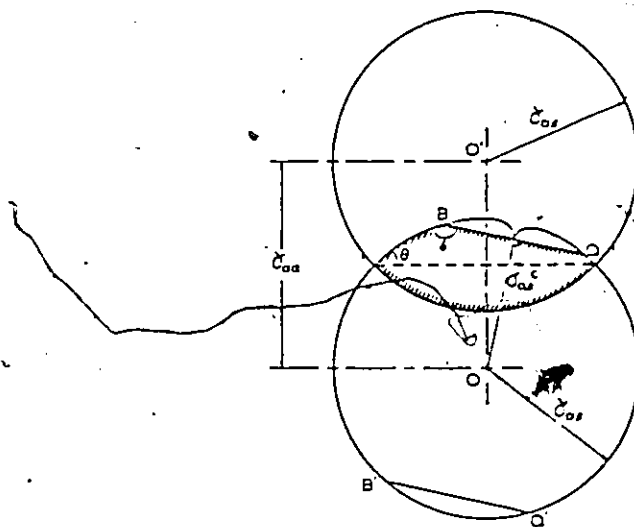


Fig. 19 Wulff construction for one-facet nucleus at a grain boundary. $\gamma_{\alpha\beta}^c < \frac{1}{2} \gamma_{\alpha\alpha}$. From ref. 13.

19 shows the equilibrium shape developed at a planar, disordered grain boundary when the nucleus/matrix boundaries are disordered at all boundary orientations present. A modified version of the Wulff plot is employed in this figure¹³.

A substantial contribution for determining the equilibrium shapes of second phase particles at surfaces and grain boundaries has been given by Cahn and Hoffman^{122,123}. These authors developed a generalized thermodynamic formulation for anisotropic (planar or curved) surfaces. Their treatment is based on a vector $\vec{\xi}$, as an alternative to the scalar function γ with which the free energy of anisotropic surfaces is classically described, defined by

$$\vec{\xi} \equiv \text{grad}(r\gamma) \quad (22)$$

with the following properties:

$$\vec{\xi} \cdot \bar{n} = \gamma \quad (23)$$

$$\xi \cdot d\bar{n} = d\gamma \quad (24)$$

$$\bar{n} \cdot d\vec{\xi} = 0 \quad (25)$$

where r is the magnitude of the position vector \bar{r}_n , and \bar{n} is the unit normal. A consequence of equation (22) is that the component of $\vec{\xi}$ normal to the interface is equal to γ , and the off-component represents the torque which tends to rotate the surface into a lower energy orientation. Equivalent to

eq. (22), there is an expression for the capillarity vector in component form:

$$\vec{\xi} = \gamma \bar{n} + (\partial\gamma/\partial\theta_{\max}) t_0 \quad (26)$$

where t_0 points in the direction of the maximum angular rate of increase of γ as indicated in figure 20. A property of the $\vec{\xi}$ vector is that, at each point along the line of intersection between 3 or more surfaces, the sum of the $\vec{\xi}$ vector of the surfaces is equal to zero. An example of the $\vec{\xi}$ vector development in the general (non symmetric) solution for isotropic surfaces is illustrated in figure 21.a. The case of anisotropic surfaces is illustrated with a particle on a twin boundary in figure 21b. Other applications of the vector formalism include the distribution of torque over equilibrium facets.

In the last of a series of papers about discontinuous precipitation (Pb-Sn alloys), Tu⁹⁹ has reopened the discussion about the initial states of grain boundary motion via the puckering mechanism. Fig. 22 illustrates its characteristics. It is then accepted that the torque term determining the grain boundary results from the sole requirement that the precipitate lies on a habit plane. Electron micrographs of grain boundary precipitates in a configuration similar to that in fig. 22b has since been published in Cu-Be¹⁶ and in Cu-Ti¹²⁴.

Recognizing the matrix/precipitate habit plane specifically as a requirement for the puckering mechanism, Ecob and Ralph¹²⁵ have recently attempted to rationalize its occurrence

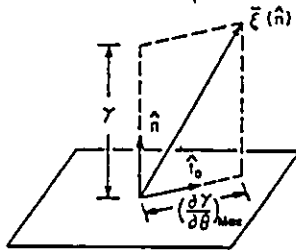
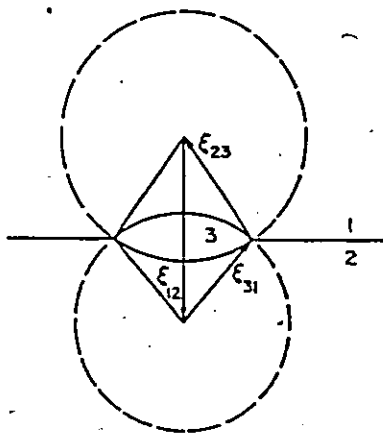
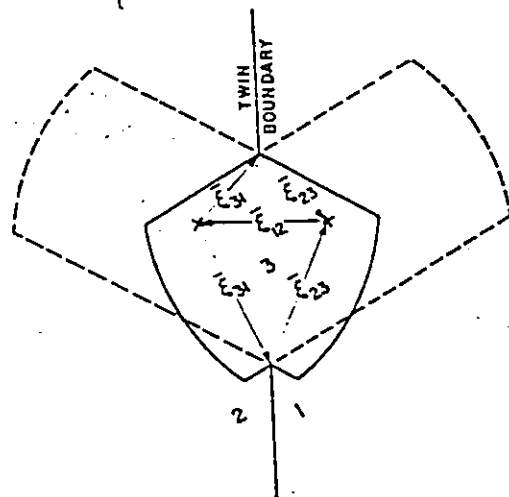


Figure 20 - Illustration of vector $\bar{\xi}$ for anisotropic surface of orientation \hat{n} . After Hoffman and Cahn¹²².



(a)



(b)

Figure 21 - Two graphs of equilibrium construction.
 a) particle with isotropic but unequal surfaces.
 b) particle at a twin boundary. In both cases the equilibrium shape is given by truncation of isolated particles. After Cahn and Hoffman¹²³.

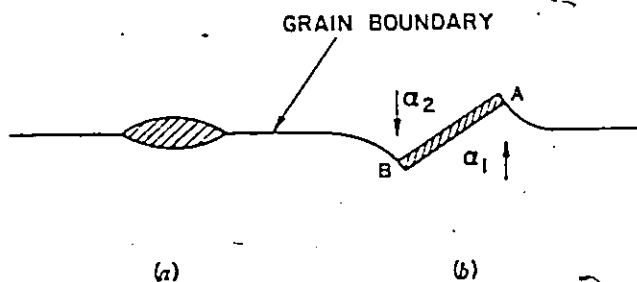


Figure 22 - Precipitates morphology on the plane of a grain boundary. a) the lens type shape, local equilibrium around its circumference is assigned, no torque is exerted by the particle; the grain boundary remains stationary. b) The disc type shape which lies on a habit plane of the lower grain α_1 . The pair of arrows indicates the torque exerted by the precipitate which twists the boundary.

(and also attach it to the method of plate multiplication). These authors have developed a technique from the O-lattice theory¹²⁶ which yields to the computation of a geometrical parameter R linked to the energy of a two-phase semicoherent interface¹²⁷. Typical FCC matrix alloy systems were discussed under this criteria and apparent consistency was shown. This procedure was, however, immediately criticized; the main argument is the use

of the R parameter to indicate the extent of free-energy anisotropy while the (large) chemical component is implicitly ignored.

Sargent et al¹²³ have examined the effect of interlaced thermodynamic forces (torques) on the structure of low angle grain boundaries. A variety of geometrical circumstances were considered. It was shown that, often, the resulting configuration can be properly estimated by considering virtual displacement at constant structure.

2.7.2 The structure of two-phase interfaces

In a recent paper, Weatherly¹²⁹ acknowledges that in contrast to the extensive literature on the structure of grain boundaries, there have been few definitive studies on the structure of interphase-interfaces other than those types where the two lattices are related by a simple transformation strain. Difficulties in identifying the defect, especially when the two phases have different structure, and relating them with a plausible dislocation model are the problems associated with characterizing the interface structure.

In present days, however, this subject is an active field of research, motivated by the powerful experimental techniques available, chiefly electron microscopy¹³⁰. A review of the contribution relating phase transformation and interfacial structure is an exhaustive task, incompatible with the extent of this section. A synopsis is nevertheless appropriate. This

is outlined below in a schematic form, accompanied by selected references. Then attention will be drawn to some points considered of interest in the present study.

Approach to the study of interphase boundaries.

a) Theoretical studies

Most of the theoretical effort has been concerned with fully equilibrated boundaries, as treated by the Frank-van der Merwe model^{131,132} and by Bollman's theory¹³³. These theories have been recently reviewed by van der Merwe¹³⁴. In regard to non-equilibrated boundaries, the Brown-Woolhouse theory¹³⁵ of misfit dislocations nucleation or acquisition has been an outstanding contribution. Often this theory is reported in agreement with experiment^{136,137}.

b) Experimental Observations

This subject has been reviewed by Aaronson¹³⁶, Murr¹⁰⁸, and by Laird and Sankaran¹³⁷. An increasing body of evidence has emerged. With the objective of observing the structure associated with the accommodation of misfit between crystals, epitaxial film-substrate methods have been used (this topic has been reviewed by Mathews¹³⁸). In the course of phase transformations, however, a variety of interphasial structural singularities have been observed. Here, it is convenient to distinguish two categories; equilibrated microstructures and partially transformed microstructures) produced by diffusional growth.

The former category involves incoherent (averaged) precipitates (relevant studies are due to Hall et al¹³⁹, to Weatherley et al¹⁴⁰) and structures produced by shear transformations (recently reviewed by Christian^{141,142}). In the last category full disordered boundaries (e.g. formed by differential growth rate, Purdy¹⁴³) and partially coherent boundaries.

Misfit dislocations represent in principle (and indeed in practice) an equilibrium component of the structure of partially coherent interphase boundaries. Studies have shown that misfit dislocations can be found under different conditions such as after prolonged annealing of precipitate plates (Sankaran and Laird¹⁴⁵), of precipitates simultaneously aged and plastically deformed under creep conditions (Weatherly and Nicholson¹⁴⁴) and of structure produced by spinodal decomposition (Livak and Thomas¹⁴⁶). Other vital feature of semicoherent interphases are ledges. These are considered as growth or structural ledges (Rigsbee and Aaronson¹⁵⁰). The TEM technique developed by Weatherly and co-workers^{147,149} have greatly facilitated the optimum viewing condition of ledges and misfit dislocations.

The mechanisms for coherency loss by the generation of misfit dislocations have been recently reviewed^{137,151}. The following, illustrated in figure 23, can be distinguished.

- a) When coherency stresses at precipitate/matrix interface are caused by a large misfit (estimated to be > 0.05) this can be relieved by the precipitate punching out prismatic dislocation loops¹³⁵.
- b) The precipitate can attract dislocation from a non-fully annealed matrix¹³⁵.
- c) For plate-like precipitates, the higher stressed region at the edge of the plate can nucleate a dislocation that eventually overlaps the precipitate. The process is repeated as the plate lengthens¹⁴⁵.
- d) Another mechanism observed for plate-like precipitates is the nucleation of dislocation loops within the precipitate. Vacancies can be attracted to coherent interfaces and condense to form a prismatic dislocation loop which can expand across the precipitate¹⁵².

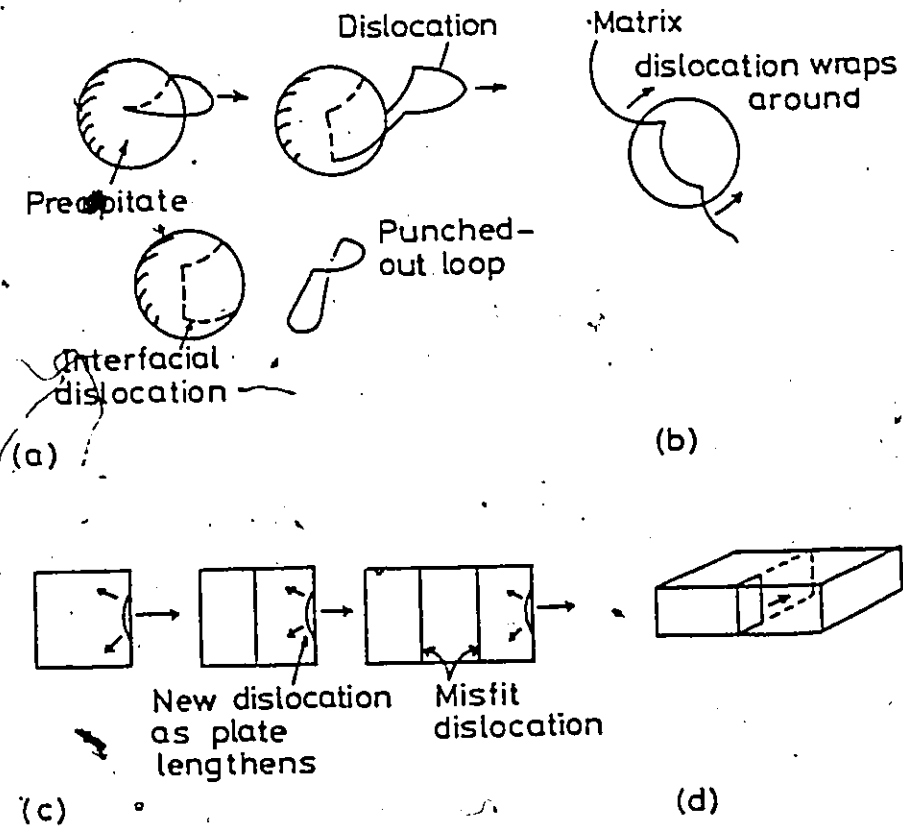


Figure 23 - Mechanisms for coherency loss. a) Dislocation punching from interface. b) Capture of matrix dislocation. c) Nucleation at edge of lengthening plate. d) Loop expansion by vacancy condensation in the precipitate.

The misfit dislocation originally considered by Frank and van der Merwe¹³¹ were pure edge. Incidentally, up to 1973 the dislocations observed were in or fairly near to the edge orientation. Mathews¹⁵³ then discussed the case of two identical orthorhombic crystals joined on (001) faces in such a way that the a axis of one crystal is parallel to the b axis of the other; a is slightly smaller than b; the crystals are strained elastically in order to accommodate the misfit. It was shown that the coherency can be treated as caused by shear without dilation, allowing the misfit to be relieved by two orthogonal sets of screw dislocations.

A more generalized mathematical study has been carried out by Sargent and Purdy. They developed a method for calculating the geometry of misfit dislocations that can completely accommodate the misfit across the interface between epitaxial crystals, and proved that even pure dilational misfit can be accommodated by two or three sets of screw dislocations, fig. 24.

An interesting result has been recently reported by Smith, Champness and Lorimer¹⁵⁵. It is related with observation of loss of coherency of lamellar precipitates in orthopyroxene. The misfit is low, 0.84%. The authors suggest that the dislocations having nucleated at the grain boundary move into their present positions by glide in the interfacial plane.

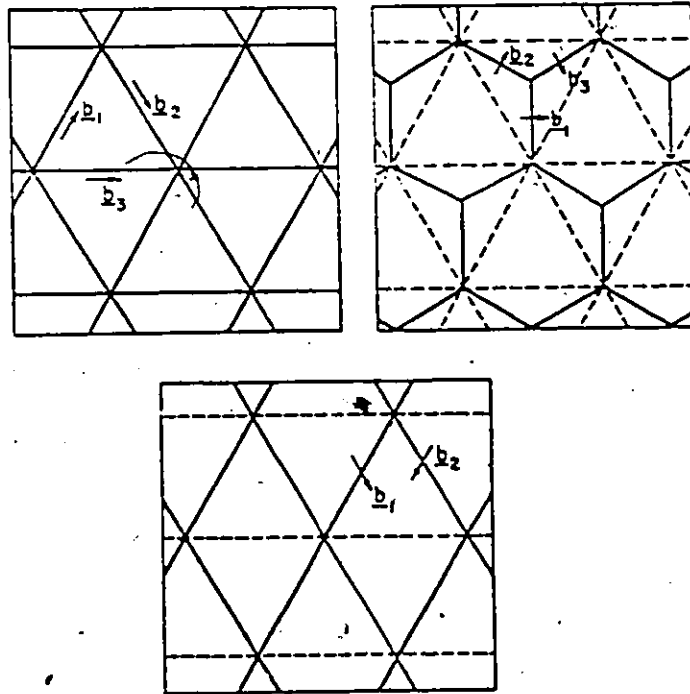


Figure 24 - Equivalent dislocation arrays which fully relieve a dilational misfit. After Sargent and Purdy¹⁵⁴.

CHAPTER 3

EXPERIMENTAL PROCEDURE AND TECHNIQUES

3.1 The Choice of Alloy System

The Al-Zn alloy system was chosen for study for two main reasons:

a) Experimental reasons:

Aluminium and zinc are simple metals, with known physical properties. Their alloys give good contrast for electrons and x-ray experiments, as required for the investigation of discontinuous precipitation reaction in detail. Furthermore, the reaction is known to occur in a number of Al-Zn alloys^{37,86,106}.

b) Practical reasons:

Binary Al-Zn alloys have not been used for commercial purposes, but alloyed with Mg (and Cu), they have extensive applications, mainly in the aeronautical industry^{158,159}. In general, discontinuous reactions can be regarded as highly undesirable since they are related to the degradation of precipitation-hardened microstructures¹⁶⁰. The answers obtained from a better understanding of discontinuous precipitation in Al-Zn might be applicable to other systems facing similar problems.

It is also noted that the Al-Zn system provides a good field for acquiring experience in electron microscopy tech-

niques. This, in turn, will be of great value for the interpretation of and experimental design associated with microstructural features in the very large spectrum of technologically important Al-base alloys.

3.2 The Al-Zn System

The equilibrium phase diagram published by Hansen and Anderko¹⁶¹ (fig. 25a) has become widely accepted over the years. Recent work on dilute alloys^{162,163} and on medium Zn concentration alloys^{104,164}, acknowledges the large extent of solid solubility at high temperatures, as given by this phase diagram. Quoting Hultgren et al¹⁶⁵ (1973): Elliot (1965) and Shenk (1960) report independent high temperature x-ray diffraction studies which indicate that the phases labelled $(Al)_1$ and $(Al)_2$, although they are both fcc, have lattice constants which differ slightly and discontinuously. Their single phase fields are separated by two-phase regions. It is suggested that the high Zn phase may be a superlattice but supporting data have not yet been obtained. Nevertheless, the modified version of the Al-Zn phase diagram is shown in fig. 25b and includes the metastable phase boundaries. (The alloys used in this study were well outside the disputed region of the phase diagram.)

Phase transformations in Al-Zn alloys have received considerable attention and a number of experimental studies have been conducted, typically on precipitation kinetics, con-

tinuous transformations and reversion. It has been generally confirmed¹⁶⁶ that in dilute alloys the precipitate sequence is^{167,168}:

supersat. α_0 + G.P. zones \rightarrow rhombohedral α + cubic α + zinc.

The spherical G.P. zones appear to form by nucleation and growth. In concentrated alloys, decomposition occurs by a spinodal reaction. In this connection, several outstanding studies have been done; we note particularly Rundman and Hillard's¹⁶⁹ study in which Cahn's theory¹⁷⁰ was successfully tested.

In the present investigation, the matrix spinodal decomposition received attention only as it impinges on the central subject of the discontinuous precipitation reaction.

3.3 Alloy Preparation

A series of Al-Zn alloys was prepared from high purity aluminium and zinc by induction melting under purified argon and chill cast into 10 mm diameter rods. The ingots were then sealed with argon for homogenization treatment at 450°C for 500h. Slabs about 1 mm thick were first checked for segregation in the electron microprobe and then cold rolled to 100 μm . The alloys had the following compositions: 6.8 \pm 0.05, 9.49 \pm 0.35, 12.23 \pm 0.05, 22.10 \pm 0.50 and 28.39 \pm 0.69 at % Zn. All the alloys were used in the x-ray microanalysis calibration, the last two for the studies of discontinuous precipitation but only the

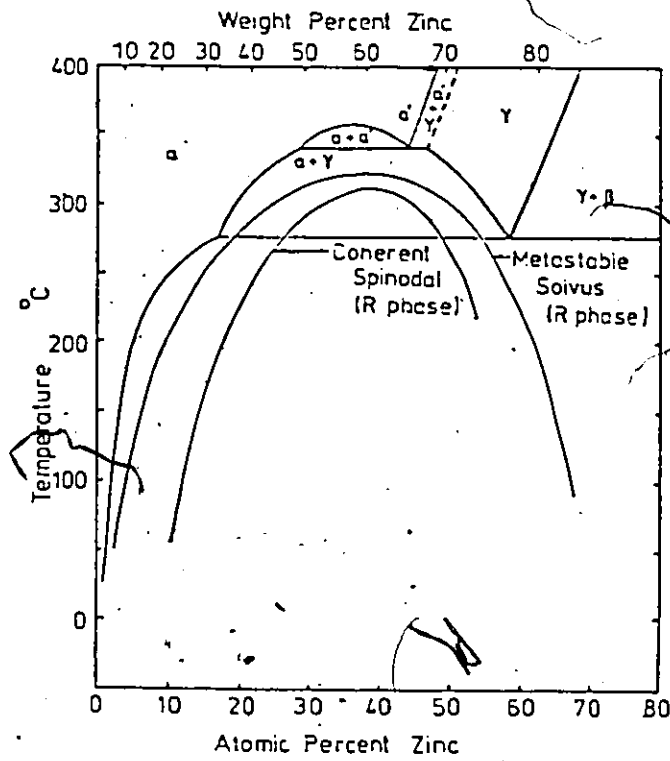
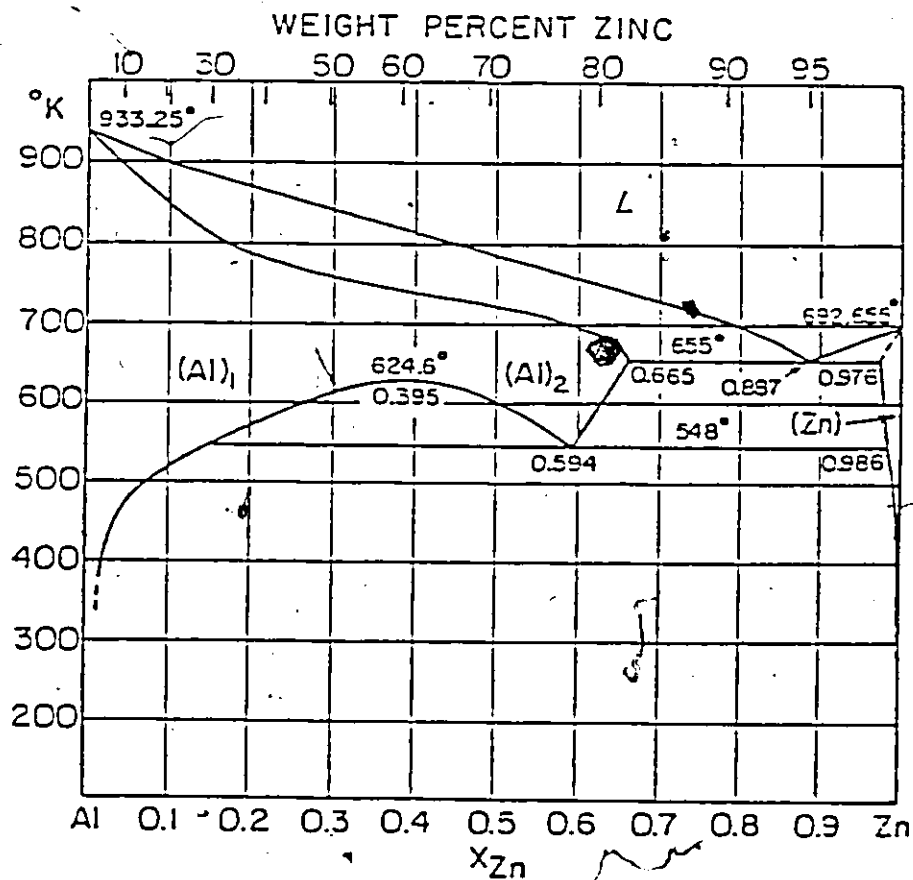


Figure 25-a) The Al-Zn phase diagram published by Hultgren et al 165. b) A modified version, borrowed from ref. 166.

22 at 8 Zn for analytical electron microscopical studies of discontinuous precipitation products.

3.4 Heat Treatment Schedule

The cold rolled strips were solution treated at 370°C during 1h in a fluidized bed furnace controlled to $\pm 1^\circ\text{C}$. A fully recrystallized structure, grain size = 150 μm , was achieved. This low solution temperature was chosen in order to avoid the formation of dislocation loops due to the quenching operation. Various quenching media were tested before the adoption of water at 0°C. In order to reproduce, as closely as possible, isothermal conditions, only fluidized bed furnaces were used. We now distinguish two heat treatment sequences (figure 26):

a) Ageing sequence:

Solution treatment, followed by quenching, and immediate ageing at the desired temperature (ranging from 110°C to 220°C).

b) Dissolution sequence:

As a) but followed by immediate annealing for a few seconds at temperatures slightly above the solvus temperature of the alloys.

After the final quench, because of the known tendency of Al-Zn alloys to decompose at room temperature, they were stored in liquid nitrogen.

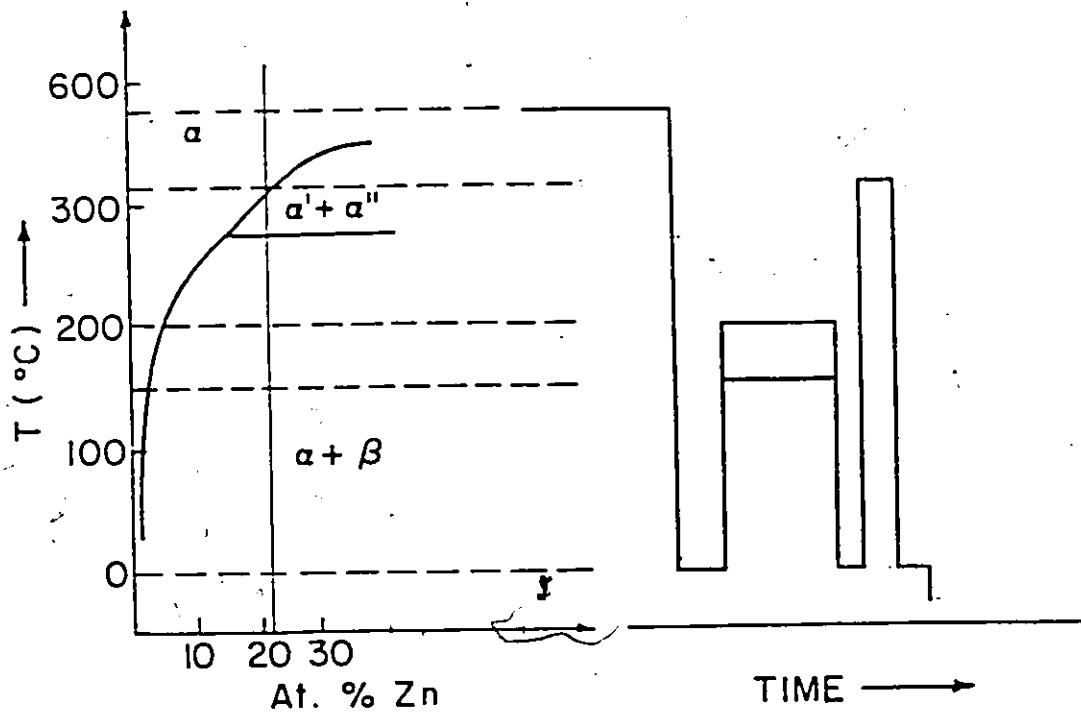


Figure 26 - Schematic illustration of the heat treatment sequences for the Al-22 at % Zn alloys.

3.5 Sample Preparation

This stage proved to be critical for the quality of microanalysis. All samples were first thinned via the window technique. The electrolyte, 22% HNO_3 in methanol, was maintained at -25°C . This method removed the oxide layer and thinned the foil to $\approx 20 \mu\text{m}$. Discs 3 mm in diameter were punched out and immediately thinned with a Struers double jet standard apparatus, using either 30% nitric or 15% perchloric solutions in methanol at -40°C . This operation took a few

minutes in most of the (successful) cases. Thus, it can be considered that the as-aged microstructure has been retained. Details of the electrochemical thinning operations are given in table I.

Table I. Electropolishing conditions

Sample size	Solution	Temperature °C	Current m Amp	Washing Sequence
1 cm ²	Methanol-22% Nitric Acid*	-25	600	Water- Methanol
disc 3 mm diameter	Methanol-30% Nitric Acid †	-40	120	Methanol- Ethanol- Methanol
disc 3mm diameter	Methanol-15% Perchloric acid"	-40	80	idem

* Window method ; † Double jet method.

The ion thinning technique was also tried using argon ions accelerated through a potential of 4 kV. The operation however took hours and the temperature in the stage was around 50°C. In consequence, the as-aged and quenched samples were susceptible to significant microstructural changes. Samples

prepared by this method were not used for microanalysis.

3.6 Electron Microscopy

A Philips 300 transmission electron microscope (TEM) operating at 100 kV was used. Detailed microstructural information was documented by means of photomicrographs along with selected area diffraction patterns, in order to permit determination of foil orientation as well as the diffraction conditions responsible for the contrast effects in the micrograph. Bright field and centered dark field techniques were employed.

The average growth rates were determined from the slope of average cell width versus ageing time, using scanning electron microscopy (SEM). (Cambridge stereoscan). Cell widths were taken as the distance from the start of the cell of the grain boundary to its leading edge with the average cell for each ageing temperature, and time being taken as the average of 10 such measurement effects. Care was taken in order to avoid sectioning effects. Average as well as local values of interlamellar spacing S were measured in the STEM and details are given in the next chapter.

3.7 STEM Microanalysis

In order to measure the Zn composition profile present in the depleted α' , extensive use was made of the energy dispersive x-ray (EDX) microanalytical capabilities offered by Vacuum Generators HB5 dedicated STEM.

The x-ray spectrum consists of two parts:

- i) Characteristic peaks which result from electrons falling into the holes in inner atomic shells; this radiation is isotropic.
- ii) A continuous background (bremsstrahlung) peaked at low energy and arising from deceleration of the fast electrons; this radiation is peaked in the forward direction.

In an ideal system, the x-rays detected come only from the area of interest on the specimen. The peak to background ratio can be maximized by placing the detector on the electron-entrant side of the specimen, so that detected bremsstrahlung is minimized¹⁷¹.

In the present system, the accurate evaluation of the composition profiles on a fine scale requires the maximization of the ~~intensity~~ of the characteristic x-rays produced within the sample while optimizing the spatial resolution.

3.7.1 Principles of characteristic x-rays production

The number of counts per second of characteristic x-ray (k_α or k_β) of an element i generated by electron excitation of a thin specimen of thickness t can be written as^{172,173}

$$(\text{cps})_i = [\phi \gamma \rho \Omega Na Pt] \left[\frac{Q_i \omega_i a_i}{A_i} \right] (\epsilon_i) c_i \quad (27)$$

where ϕ is the electron beam flux, γ the anisotropy factor, ρ the density of the material, Ω the fraction of radiation being

collected, N_A Avogadro's number, P the area of the electron probe spot, Q_i the ionization cross section, w_i the fluorescence yield, a_i the characteristic k_α fraction of total emission ($k_\alpha / [k_\alpha + k_\beta]$), A_i the atomic weight, ϵ_i the detector efficiency and c_i the concentration of i in weight fraction. Thus, the first term in brackets contains parameters depending on the instrument and on the material of specimen, i.e. common to all elements. The second term in brackets contains parameters depending on element i being analyzed only while ϵ_i depends on both the element i and the instrument. Therefore, eq. (27) can be written as

$$\text{cps})_i = B k_i \epsilon_i c_i \quad (28)$$

This is however, a fairly idealized situation since the analysis ignores loss of electron energy, absorption of x-rays in sample and fluorescence (thin film assumption) and does not account for spurious X-ray generation¹⁷⁴. Nevertheless, this approach is very useful in STEM for analysis of the concentration ratio between elements A and B being measured simultaneously. Factor B in eq. (28) cancels out and we arrive at the Cliff-Lorimer¹⁷⁵ equation for non-absorbing systems

$$\frac{C_A}{C_B} = \frac{k_B \epsilon_B}{k_A \epsilon_A} \frac{(\text{cps})_A}{(\text{cps})_B} \equiv k_{AB} \frac{(\text{cps})_A}{(\text{cps})_B} = k_{AB} \frac{I_A}{I_B} \quad (29)$$

where the factor k_{AB} is a constant for a given operating voltage independent of composition and thickness. k_{AB} can be calculated analytically or determined experimentally.

- i) experimentally: need only use of standards
 ii) analytically : from first principles (59)

$$k_{AB}^* = \frac{A_B(Qwa)_A}{A_A(Qwa)_B} \quad (30)$$

This fraction of k_{AB}^* must be corrected for absorption in the solid-state detector by the Be window (BeF), the Au layer (AuF) and the Si dead layer (SiDLF). Thus,

$$k_{AB} = k_{AB}^* \cdot \text{BeF} \cdot \text{AuF} \cdot \text{SiDLF} \quad (31)$$

where

$$\text{BeF} = \frac{\exp(-\mu/\rho \left| \begin{matrix} A \\ \text{Be} \end{matrix} \right. \rho_{\text{Be}} t_w)}{\exp(-\mu/\rho \left| \begin{matrix} A \\ \text{Be} \end{matrix} \right. \rho_{\text{Be}} t_w)} \quad (32)$$

and similar equations hold for AuF and SiDLF. In eq. (32) μ/ρ , is absorption coefficient for A or B x-rays, ρ the bulk density and t the thickness. Thus a major difficulty with the analytical method lies in the need for calibration of the EDX detector.

3.7.2 Resolution limiting factors

In a thin sample the spatial resolution for chemical analysis is dramatically improved compared to the bulk. An accurate account must consider the following factors:

- a) Incident probe diameter, d :

Probe diameter may be estimated using the method of Venables and Janssen¹⁷⁶; beam aberrations contributed to its enlarge-

ment. Estimates of probe diameter produced on the McMaster HBS STEM have been tabulated by Robertson¹⁷⁷ for different operation conditions, table II. The smallest 100 μm virtual objective aperture (VOA) was used and produced a probe diameter of 10 \AA .

Table II. Probe sizes* and angles in the McMaster HB5 STEM

#	Optimum resolution	Objective aperture (OA)			Virtual objective (VOA)		
		1	2	3	1	2	3
diameter (μm)	116 (VOA)	100	50	20	300	200	100
equivalent OA diam.	81 (OA)	100	50	20	210	140	70
probe diameter (\AA)	9.1	37	12	27	300	90	10
probe semi-angle (mr)	6.8	8.6	4.3	1.7	18	12	5.8
relative probe current	1.0	1.6	0.4	0.06	6.9	3.1	0.8

* $\pm 20\%$ approximately

b) Beam spreading; b

Beam spreading in thin foils is currently a lively topic of both experimental investigations¹⁷⁸⁻¹⁸⁰ and theoretical analysis. One approach is to use Monte Carlo simulation methods^{181,182} or use a single scattering model¹⁸³ which yields to a useful expression for the spreading

$$b = 6.25 \times 10^5 \frac{z}{E_0} (\rho/A)^{1/2} t^{3/2} \quad (\text{cm}) \quad (33)$$

where z = average atomic number, A = average atomic weight,

E_0 = energy of electron beam in eV, ρ = density in g/cm^3 , and t = sample thickness in cm. At 100 kV operating potential, equation (33) gives for $t = 100$ nm in Al foils $b = 8.13$ nm. This value is, however, accurate typically to $\pm 30\%$ (approximately).

c) Specimen drift

Thermal or mechanical instabilities may cause the specimen to move during the x-ray acquiring time, thereby reducing the resolution. Drift is detected through the motion of the image and estimated, typically, about 2 nm during 60 s acquiring time.

d) Sectioning effects

This is also a factor to be considered and even of critical importance in the presence of an interface causing the broadening of the composition profile measured across it, as discussed by Wycliff¹⁸⁴.

The accuracy, rather than the spatial resolution, is further dependent on 2 additional factors:

e) X-ray absorption

Analysis in thicker samples requires that absorption correction be applied to equation (20), namely^{183,185}

$$\frac{C_A}{C_B} = k_{AB} \frac{I_A}{I_B} \exp\left\{-\frac{\rho t}{2} \left([\mu/\rho]_{\text{spc}}^B - [\mu/\rho]_{\text{spc}}^A \right) \cos\alpha \right\} \quad (34)$$

In this equation α is the take-off angle. Preferential absorption of x-rays by the specimen (spc) may alter the

ratio of characteristic x-ray intensity. Zaluzec¹⁷³ gives the standard Tixier-Philebert criteria¹⁸⁵ for assuming a thin film sample (i.e. no absorption).

$$\left\{ \left[\frac{\mu}{\rho} \right]_{AB}^A \sin\beta / \cos(\beta - \alpha) \right\} \rho t \leq 0.1 \quad (35)$$

where β is the incidence angle. It should be noted that the absorption path length varies with both the sample tilt and the relative position of the wedge-shaped sample with respect to the incoming beam.

f) Extraneous x-rays

These are x-rays generated from other than the sample region excited by the focussed electron beam, and are caused by two major effects: (1) stray radiation in the illumination system and (2) specimen interaction with the primary electron beam. McMaster's HB5 STEM is equipped with a modified x-ray collimator¹⁸⁶ (fig. 27) which helps to minimize extraneous contributions to EDX spectra and to permit more accurate microchemical analysis¹⁸⁷.

3.7.3 X-ray data collection

X-ray counting statistics are usually assumed to be described by a Poisson distribution, such that, at the 90% confidence level, the relative error in the number of counts I is $\sim 2\sqrt{I}$. Thus, in principle, the relative error in a given analysis time is reduced by maximizing the count rate. There are, however, limitations imposed by the detection system which dis-

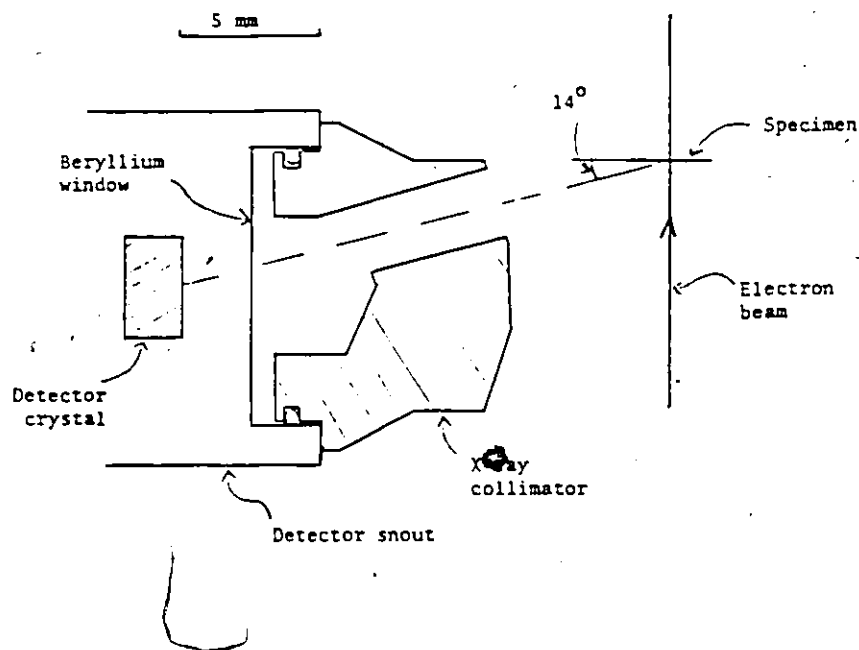


Figure 27 - McMaster HB5 STEM x-ray detector system.

plays undesirable effects at very high input count rates, as discussed in detail by Woldseth¹⁸⁸. On the other hand, the need to maximize the spatial resolution requires the use of the smallest probe size, which, while permitting "safe" count rates, increases the chances of producing specimen-borne contamination build-up due to high current density. Carbon contamination on the sample, influencing the absorption of generated x-rays, has an adverse effect on the quality of the microanalysis.

3.7.4 Operation and interpretation of data

EDX data was obtained from individual lamellae of interest by first imaging at high magnification (500K \times , 1M \times depending on S) to attain thermal stability, then stopping the probe and simultaneously recording the convergent beam diffraction pattern (CBDP) during EDX acquisition. A fixed tilt stage, mean take-off angle 14 $^\circ$ was used.

Composition profiles in α' , close to α_0/α' interface were measured by "manually" stepping the probe at appropriate and measured intervals with the specimen fixed. Since the Zn lamellae were dissolved in the thinning process, microanalysis very close to the α'/β interface was possible. Also, beam broadening and sectioning effects, associated with β , were largely reduced. In order to measure as close as possible the actual composition profiles, the following selection criteria were adopted.

- i) Well defined reaction fronts exhibiting steady state growth conditions were generally chosen (although, for comparative purposes, a few non steady state reaction fronts were also analysed).
 - ii) Due to the limitations imposed by the fixed tilt stage, only lamellae with both α_0/α' and α'/β interfaces fairly parallel to the beam were selected.
 - iii) In order to minimise and equalize foil thickness, in the majority of cases lamellae with α/α' interfaces close to and accompanying the edge of the foil were analyzed.
- This in many cases allowed the adoption of the thin film

condition.

- iv) Foils with orientation such that the x-ray path lay within a' were preferred.
- v) Specimens giving rise to significant contamination build-up were eliminated for analytical purposes.

To fulfil the above requirements, a large number of foils had to be prepared and carefully studied. This gave useful morphological information.

The characteristic x-ray spectra for Al and Zn are relatively simple and well resolved by the kevelex detector system. The characteristic Al k_{α} and Zn k_{α} were used. The backgrounds were subtracted systematically by the computer method provided with the kevek 7000 system. The peak intensities were determined by both the integration over the full peak width and integration over full width at half maximum (FWHM).

Quantifying x-ray information from the STEM through Cliff-Lorimer method requires knowledge of the k_{ZnAl} factor (in the thin film approximation). Diluted standards, whose composition is given in sec. 3.2 were used. All precautions were taken in order to preserve the homogeneous solid solution before the analysis; the samples were solution treated and thinned just prior to observation. The data used for the calibration of the k factor came only from the thin region of the foil, as observed by the CBDP.

The foil thickness measurement by CBDP technique¹⁸⁹ demands a two-beam dynamical diffraction condition being opera-

ting. In view of the lack of tilt, this condition was not controllable and occurred fortuitously when analyzing individual lamellae.

Two other diffraction modes available in the STEM were used.

- i) "Parallel" beam diffraction, aiming to obtain high resolution ($> 100 \text{ \AA}$) misorientation information.
- ii) Grigson selected area diffraction, which is equivalent to the conventional selected area in the CTEM, and was used to obtain information on the parent-product matrix misorientation and to enhance morphological detailed observation by means of dark field techniques.

CHAPTER 4
EXPERIMENTAL RESULTS

The present investigation attempts a description, as fully as possible, of the processes involved in the discontinuous precipitation phenomena occurring in aluminium rich Al-Zn alloys; the objective being the evaluation of the thermokinetic parameters governing the reaction and the microstructure associated with it. The observation of decomposition by mechanisms other than the discontinuous mode are included so that the latter can be properly placed in relation to the thermodynamical considerations. In this perspective, the experimental procedure was conducted with emphasis on the following aspects:

- i) Detailed CTEM and STEM studies, enabling the characterization of the pertinent morphological features;
- ii) Analytical electron microscopy involving STEM x-ray microanalysis and microdiffraction studies of individual lamellae;
- iii) Description of the alternative reactions in relation to the discontinuous precipitation;
- iv) Accounting for the dissolution of β lamellae, when the aged microstructure is annealed slightly above the solvus temperature.

The above points have sufficient autonomy to be described in separate sections. This procedure is adopted here; it will, perhaps, help to simplify the problem. Results will be presented in terms of representative electron micrographs. Only the main feature of the observed microstructure will be pointed out in the text, while details of each micrograph will be given in the figure captions.

4.1 Morphological Features of the Discontinuous Precipitation Product

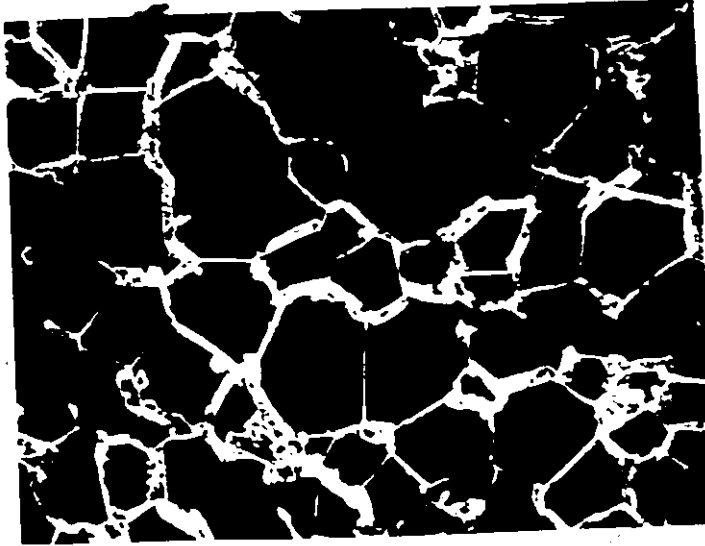
4.1.1 Extent of the reaction

Evidence for discontinuous precipitation was found under all the conditions investigated, table III, in both Al-22 and 28% at.% Zn (previously homogenized as indicated in section 3.4).

Table III. Ageing treatment

Alloy	$T_m/2$	Aging Temperatures	Time
Al-22 at.% Zn	435K	383K to 483K	120 to 600 s
Al-28 at.% Zn	425K	393K to 483K	120 to 600 s

In this range of temperature discontinuous precipitation in these alloys occurs comparatively rapidly. Not all the grain boundaries, however, act as reaction fronts. Typical low magnification features are given in fig. 28. An idea of the extent of the reaction could be given by the average cell growth rate at the dif-

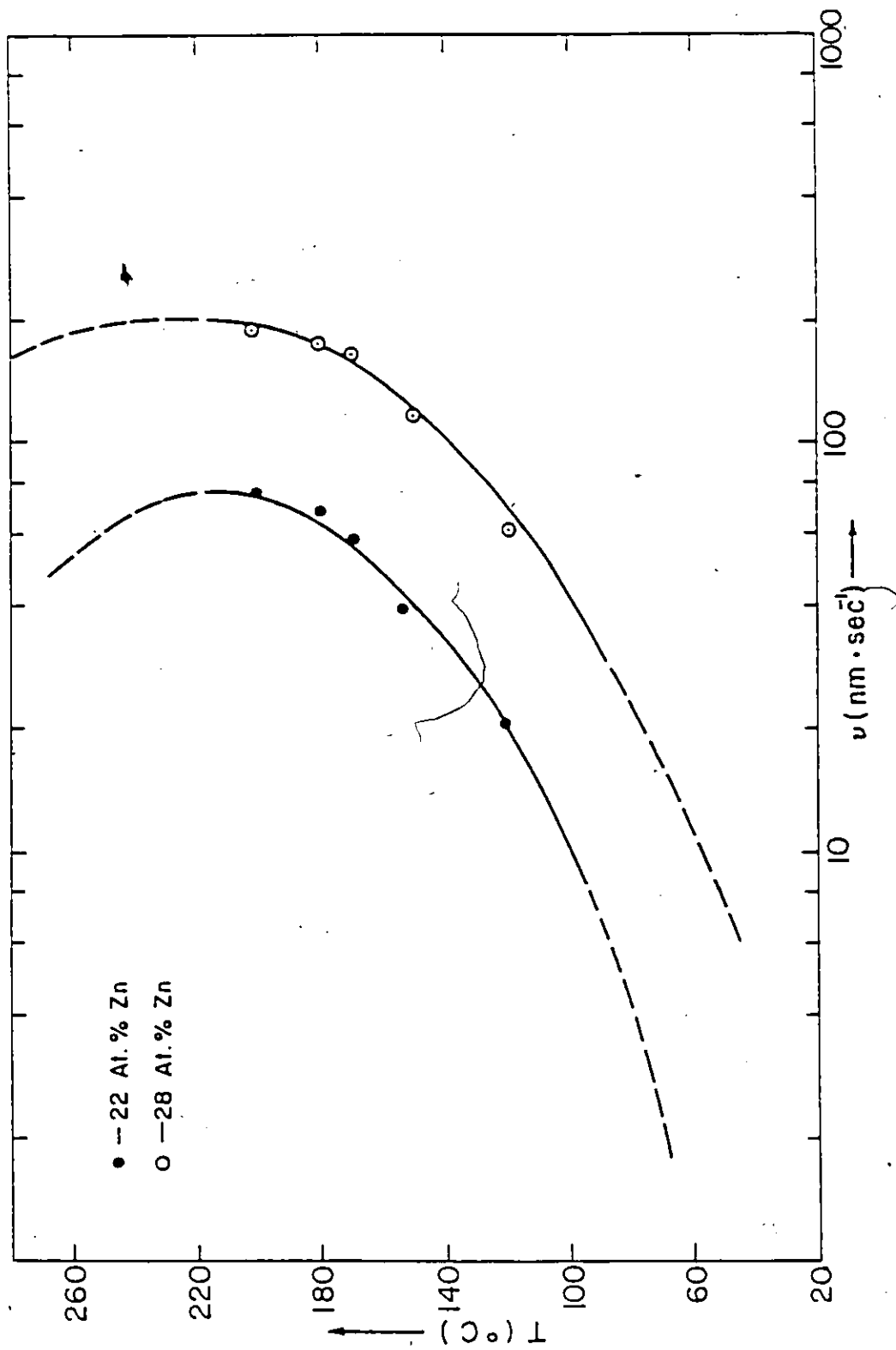


a



b

Fig. 28 a) Al-22 at.% Zn, 473K, 300 s
b) Al-28 at.% Zn, 473K, 300 s
Note high density of discontinuous precipitation
product and some precipitate-free grain boundaries.
SEM micrographs. 170 \times .



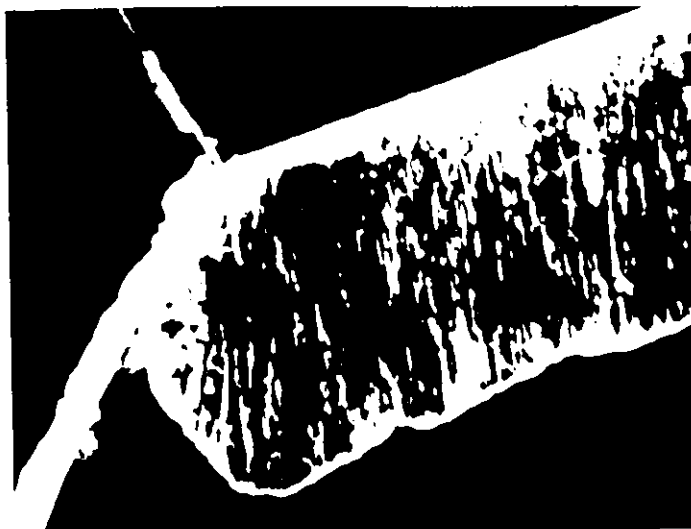


Fig. 30 Al-22 at.% Zn, 423K, 300 s
SEM micrograph 4200 \times .

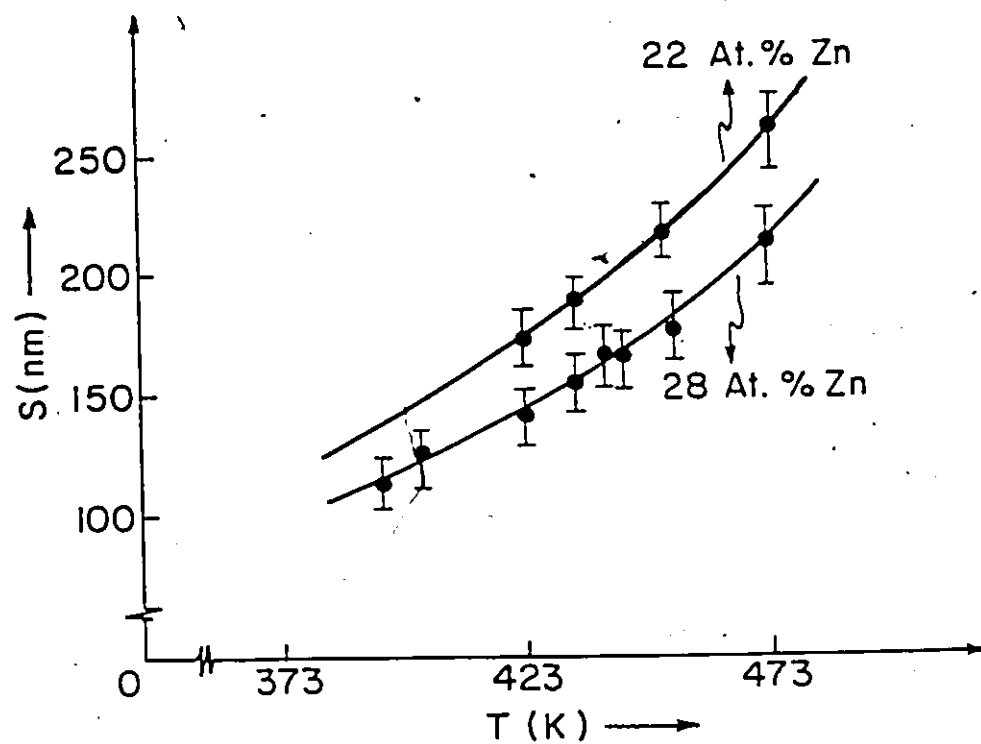


Fig. 31 Average cell spacing versus
ageing temperature.

ferent temperatures. This relation was estimated as described in section 3.6 and is plotted in fig. 29. In order to reduce sectioning effects, cells in which the precipitate lamella lay (fairly) parallel to the sample surface were chosen; an example is given in fig. 30. The average interlamellar spacing as a function of the ageing temperature is given in fig. 31. It should be stressed, however, that such average-overall values are to be regarded cautiously; they merely provide us with a rough idea. As it will become clear from section 4.2, kinetic considerations require local values of these variables.

4.1.2 Modes of grain boundary migration

The essential characteristic of discontinuous precipitation is the concurrent migration of the grain boundary reaction front. As discussed in section 2.4, mechanisms have been proposed to explain the s-shape of the reaction front^{63,64}. Their connection with the double seam morphology and a relation with the ageing temperature¹⁶. The present study shows that a variety of configurations can result:

- i) Development of an s-shape grain boundary migration in the absence of discontinuous precipitation, fig. 32. The process takes place in the bulk.
- ii) The grain boundary initially migrates as in the previous case but in the thin foil, maintained for about 2 h at a lower temperature, develops discontinuous precipitation at both sides of the boundary in an s-shape fashion, fig. 33.

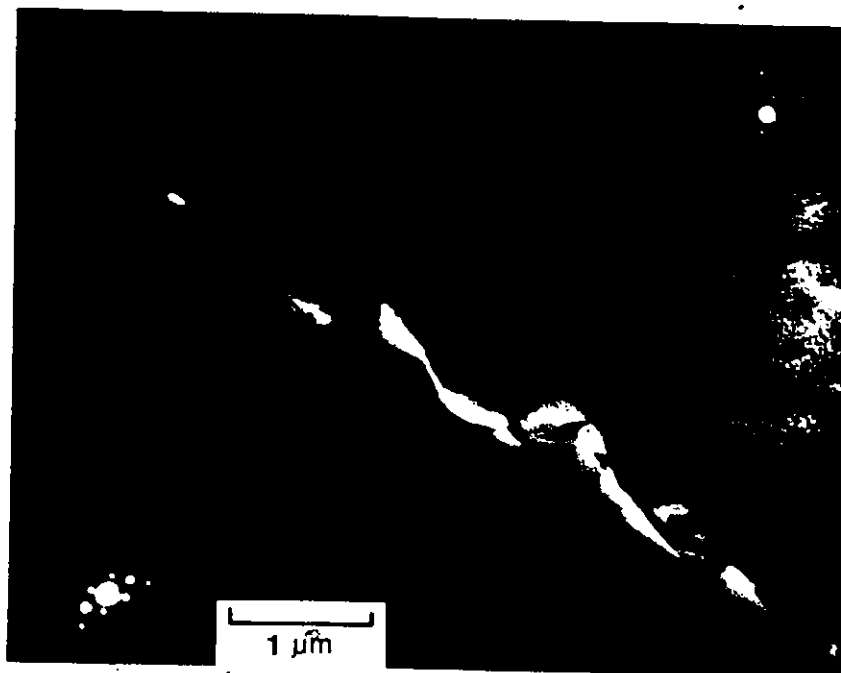


Fig. 32 Al-22 at.% Zn, 478K, 300 s.
The migration of the boundary took place in the bulk. The thin foil was maintained in the TEM stage for about 2 h. The boundary did not continue moving at a measurable speed. The effect of surface diffusion is probably responsible, STEM, bright field, BF, micrograph, 20K \times . Inset the selected area microdiffraction patterns from the two grains showing they are slightly misoriented.

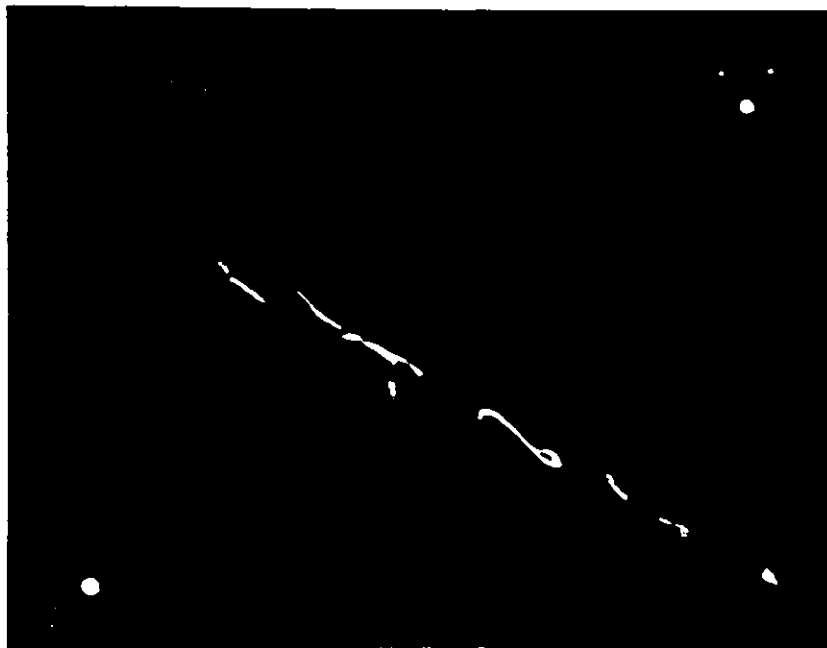


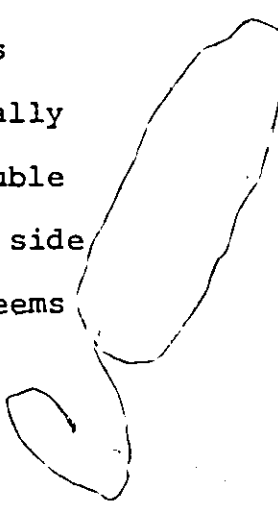
Fig. 33 Same sample as in fig. 31. Different grain boundary. A second stage of boundary migration proceeds in the thin foil but this time, producing discontinuous precipitates. Annular dark field, ADF, STEM micrograph 10k \times . The SADP insert shows that the two parent grains are more misoriented with each other than those in the previous figure.

iii) The precipitation takes place initially at both sides of the original grain boundary, the resulting cell configuration being in s-shape, fig. 34. The transformation took place isothermally in the bulk.

In the three cases above, the alloy is the same and the samples have been identically annealed, 478K, 300 s. In the third case, in contrast with the second, the regular interlamellar spacing at the reaction front suggests that the growth process has attained the steady state.

iv) The grain boundary has migrated in one direction only generating a single seam steady state morphology, fig. 35.

v) The migration of the boundary in two directions has quickly resulted in a double seam morphology growing in steady state, fig. 36. A variety of intermediate configurations has been often observed. In fig. 37, for instance, is shown the growth in opposite directions of two, partially connected single seams. An intriguing topological double seam configuration is shown in fig. 38: while at one side of the boundary it moved regularly, at the other it seems to have occurred in a "discontinuous" fashion. It is interesting to note that neither the resulting single or double seam morphologies are markedly dependent on $T_m/2$. At 478K double seams are formed (figs. 34, 36) while at 428K single seam morphologies are frequently found (figs. 30, 35). Exactly the contrary is to be expected if



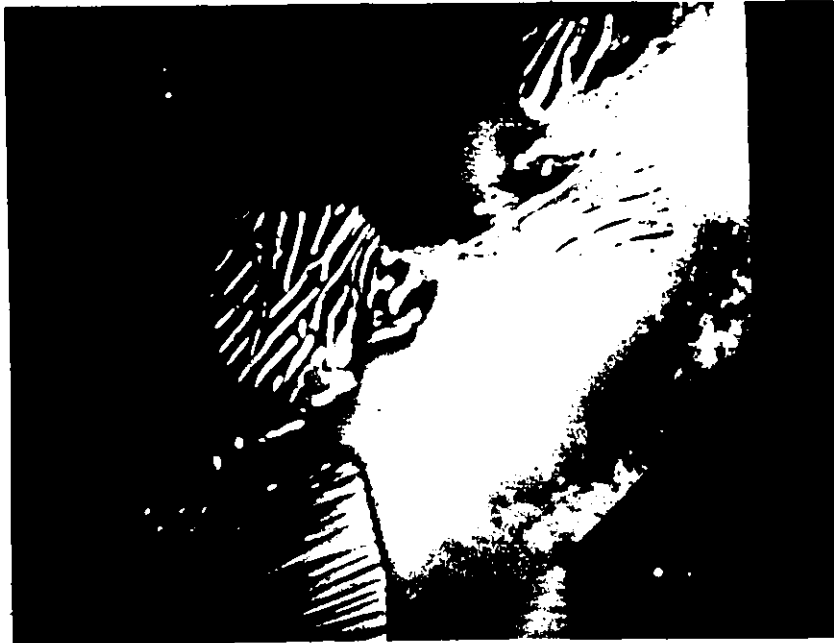


Fig. 34 Development of discontinuous precipitation colonies at both sides of the original grain boundary position. This is an as aged and quenched microstructure, the precipitation; took place isothermally, 478K, 30 s, in the bulk. Al-22 at.% Zn, STEM, ADF micrograph 5k \times .

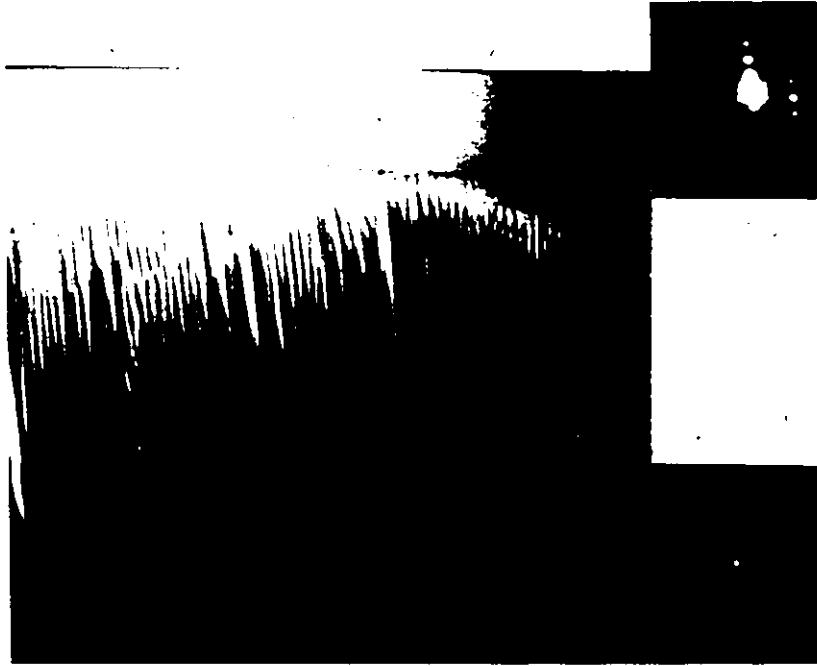


Fig. 35 Al-22 at.% Zn, 428K, 300 s. ADF STEM micrograph showing a regularly formed single seam colony.)

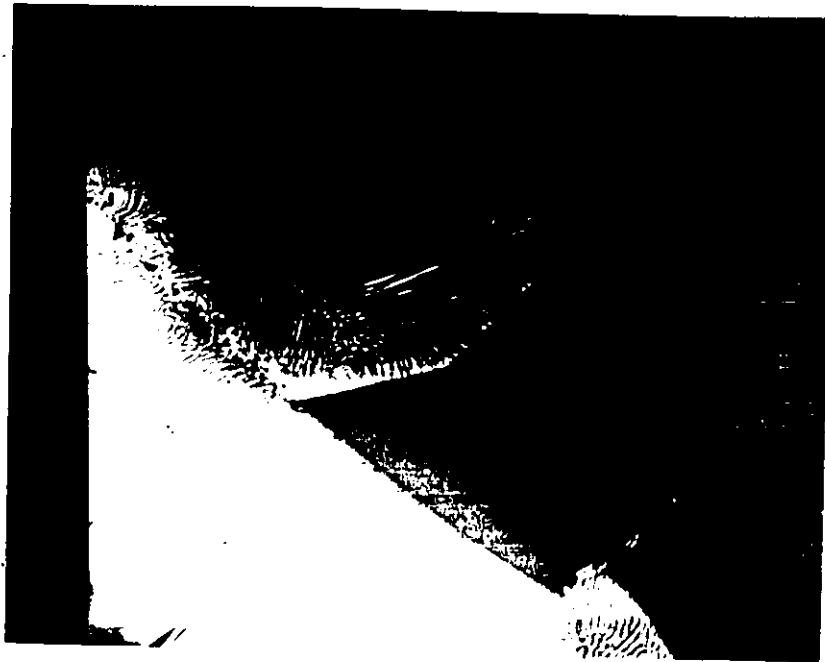


Fig. 36 Al-22 at.% Zn. 478K, 300 s . ADF STEM micrographs showing a large extent of discontinuous precipitation reaction in a partial double seam morphology.

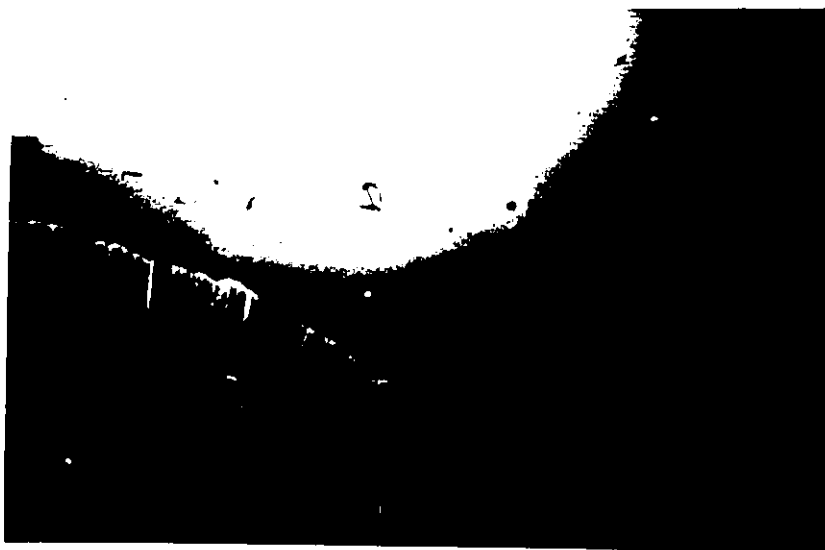


Fig. 37 Al-22 at.% Zn, 428K, 300 s
ADF STEM micrograph, 2K x.



Fig. 38 Al-22 at.% Zn, 428K, 300 s
ADF STEM micrograph 5K x.



Fig. 39 Al-22 at.% Zn, 478K, 180 s.
Single, double seam and intermediate
morphologies are evident. Annular
dark field under low mag image setting
STEM micrograph.

the proposition of Bauman et al.¹⁶ is correct. Indeed, in all the samples observed, annealed at either low or high temperatures, both single and double seam morphologies coexist. However, the double seam was more common than the single seam at low temperature while the inverse is true at higher temperatures, fig. 39.

4.1.3 The reaction front morphology

In what follows all the micrographs are related to the Al-22 at.% Zn alloy. The reaction front morphology could be regarded under two headings:

a) Macroscopic appearance

A wide spectrum was observed, from very irregular, as in fig. 40, to remarkably regular, as in fig. 41, the most typical being an intermediate case of these two extremes, fig. 42. It is readily noted that steady state growth is accompanied by nearly equally-spaced lamellae.

b) Microscopic appearance

Of particular interest are observations of the quenched α_0/α' interface shape, since it is a key to the analysis of the local forces at the reaction front. In the present study on microstructures characterizing the steady state growth the convex-forward or nearly flat (but never concave) α_0/α' interface has become clear. An easy way to image them in the bright field mode is by controlled tilting of the sample, fig. 43. The image may be, however, diffuse.

A more powerful technique is the centered dark field and here the STEM gave better resolution. An example is provided in fig. 44.

4.1.4 Microstructural characteristics of the discontinuous product

a) The early stages

Since discontinuous precipitation in Al-22 at.% Zn takes place with an average high speed, the initial stages are not easily detected. The pucker mechanism was never observed. Some grain boundaries exhibit a bowing character in similar fashion as in DIGM systems, fig. 45. The spacing between the pinning Zn rich pockets is about 5 to 10 times larger than that adopted by the interlamellar spacing of the discontinuous precipitation cell growing in steady state at the same temperature. That the grain boundary has actually migrated maintaining the same orientation is apparent from the dark field image, fig. 46. The migration is evidently not capillarity assisted nor thermally induced, at 423K. The DIGM event is strongly suggested and more support for it will come from the microanalysis results in section 4.2. It was a common feature for most of the cells to exhibit a disorganized, widely spaced, microstructure before the onset of the steady state lamellar structure in either single, fig. 47a, or double-seam morphology, fig. 47b. The migration of the boundary preceding the onset of discontinuous precipitation is seen in fig. 48.



Fig. 40 An irregular cell front, 428K, 300 s.
STEM ADF⁷ micrograph.

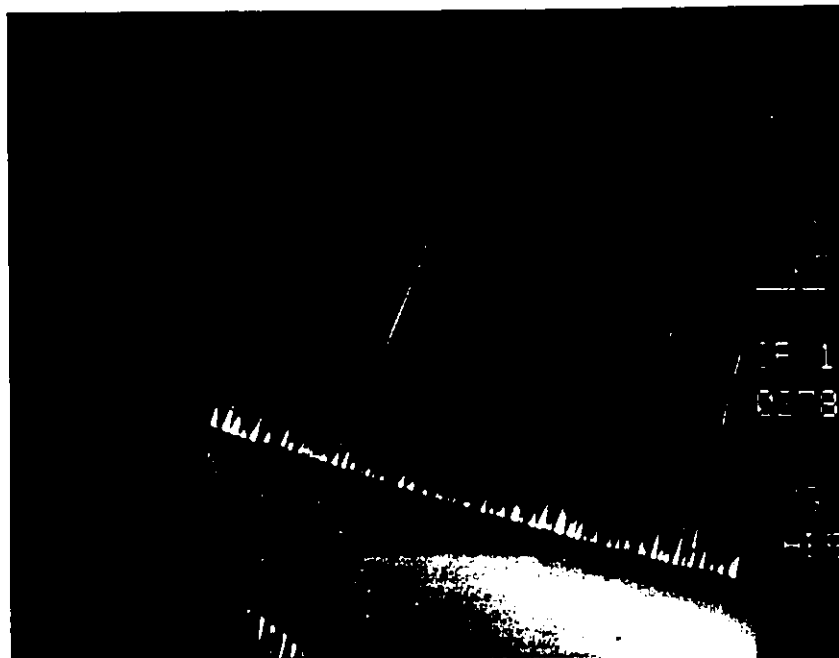
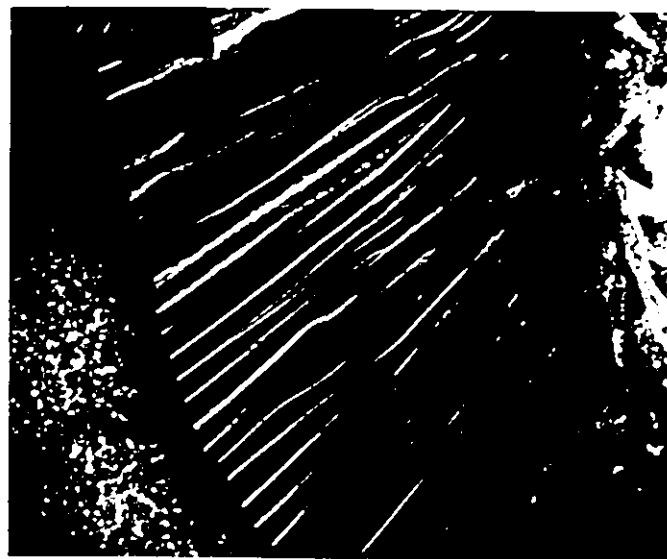
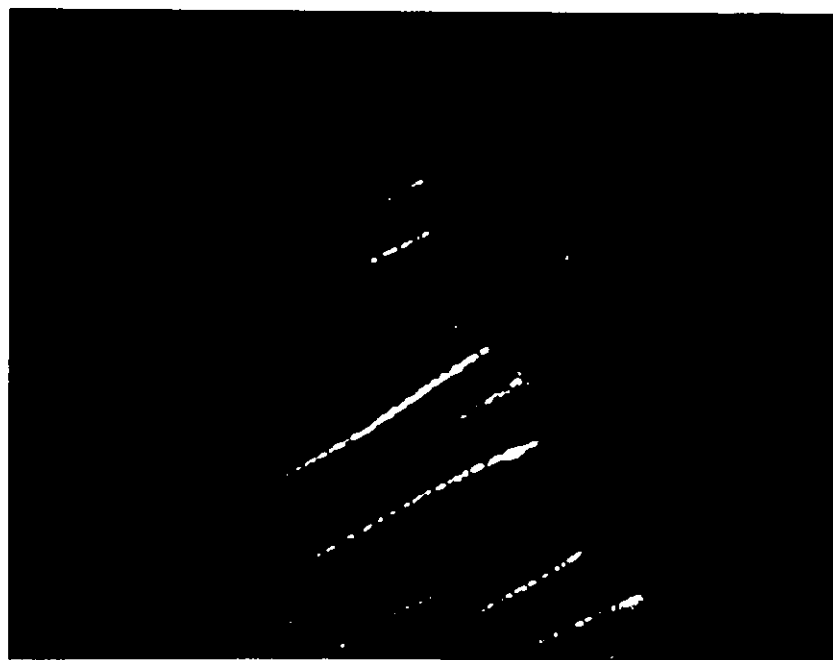


Fig. 41 A regular reaction front, 478K, 300 s.
STEM ADF micrograph

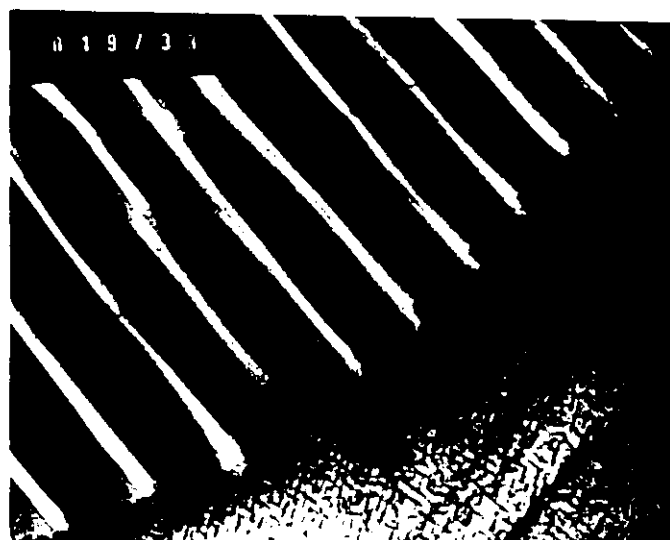


a

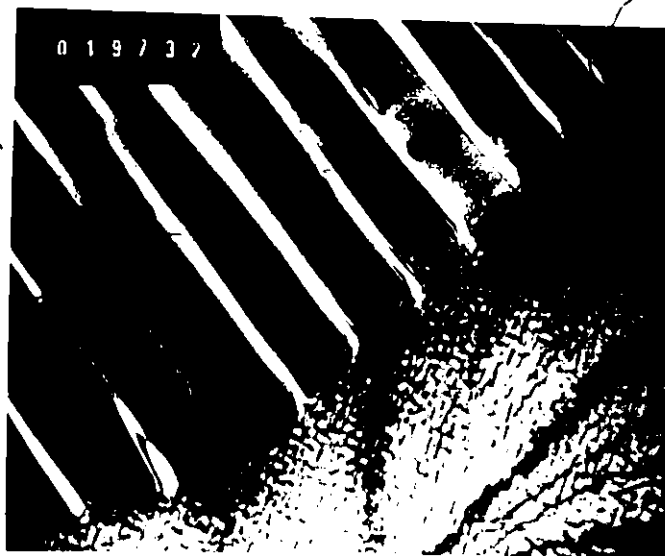


b

Fig. 42 Two typical cell matrix interfaces characteristic of steady state growth. 428K, 300 s
a) TEM micrograph, 25K \times , b) STEM micrograph, 50K \times . Interfacial precipitates occurred after the thinning of the foil, are decorating the reaction front.

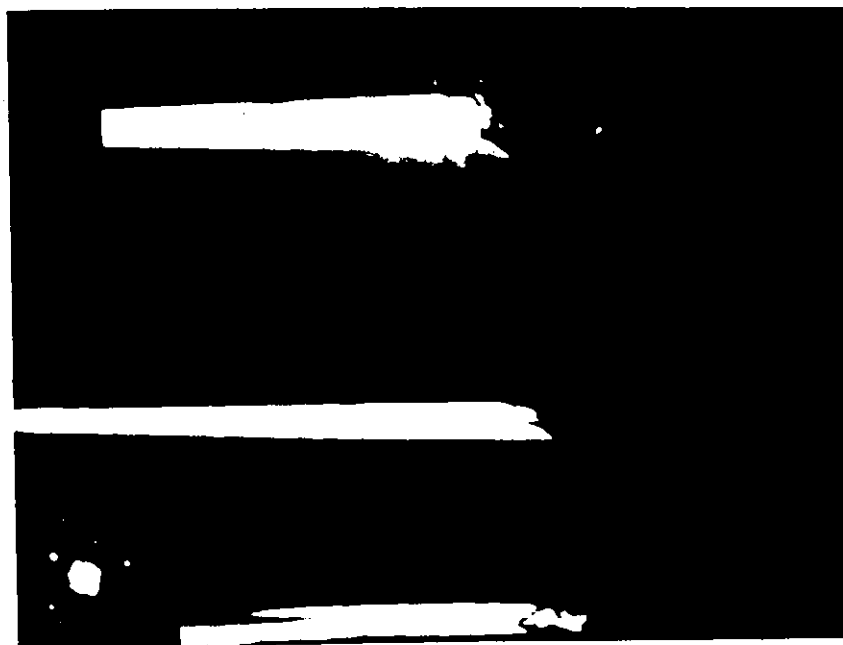


a

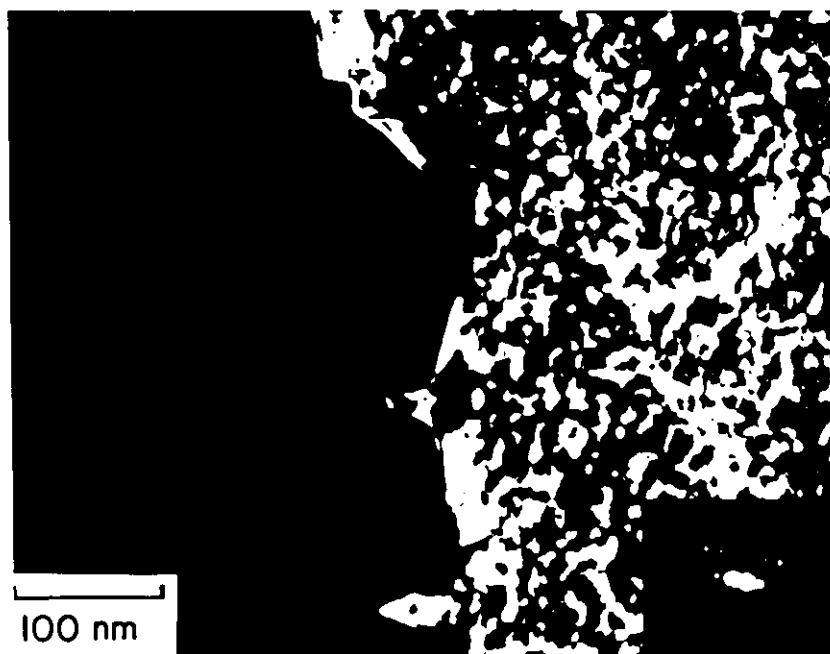


b

Fig. 43 The imaging of the α_0/α' interface
a) No shape is apparent, b) Dynamical
fringes aid its visualization. B.F.
TEM micrographs. 44K \times



a



b

Fig. 44 Imaging of the α_0/α' interface in the STEM
a) BF, b) CDF with a parent grain reflection.
428K, 300 s.

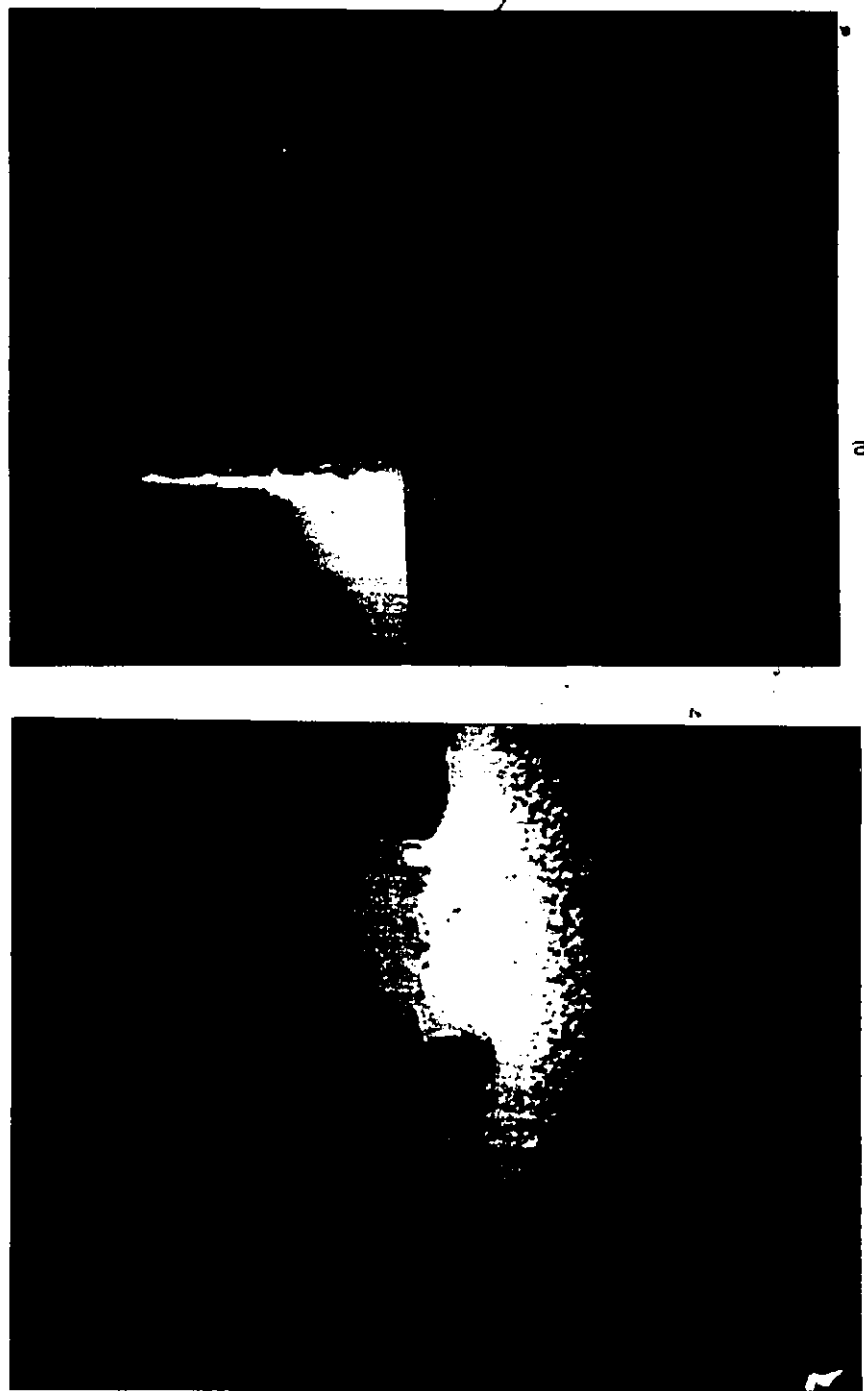


Fig. 45. Sample annealed at 428K, 300 s.
a) in ADF low magnification, where a discontinuous precipitation cell and some bumps are visible.
b) Magnification of the DIGM region. Dark zones are Zn rich pockets.



a



b

Fig. 46 Bowing grain boundary.
a) bright field, b) Centered
dark field with a growing grain
reflection. 428K, 300 s.
• TEM micrograph. 30K x.



a



b

Fig. 47 Disorganized microstructure precedes the steady state lamellar growth in a) single, and b) double seam morphologies. TEM micrographs, 10K \times .



Fig. 48 Grain boundary migration preceding the onset of discontinuous precipitation. 478K, 300 s. STEM micrograph 20K ×.

- b) Discontinuous cell/parent matrix relationship after extensive growth.

The more complex case corresponds to the double seam morphology. Fig. 49a illustrates an example obtained from the STEM. Fig. 49b is a matrix centered dark field. The seam at the left is clearly related to the parent grain at the right from which it was growing. A second example is given in fig. 50. Figs. 50b and 50c are matrix CDF images of each grain. It is clear the discontinuous matrix/untransformed matrix orientation relationship has persisted during growth. The two examples above are from samples isothermally treated in the bulk. The continuity of the orientation is maintained if a preexistent discontinuous cell is allowed to grow in the thin foil, fig. 51. On the other hand, CDF image of the transformed cell has revealed non-uniform diffraction contrast, suggesting that a significant amount of elastic energy is stored, fig. 52.

4.1.5 Mechanisms of lamellae multiplication

In section 2.4 two mechanisms were mentioned and are recalled here. In quenched microstructures characteristic of isothermal steady state growth, the branching mechanism has been observed, e.g. fig. 52a. In cells growing in foils, i.e. under non-isothermal conditions and at lower temperature, the branching is dominant, e.g. fig. 51. Paradoxically, in the same figure there is evidence for renucleation and growth of fresh precipitates.

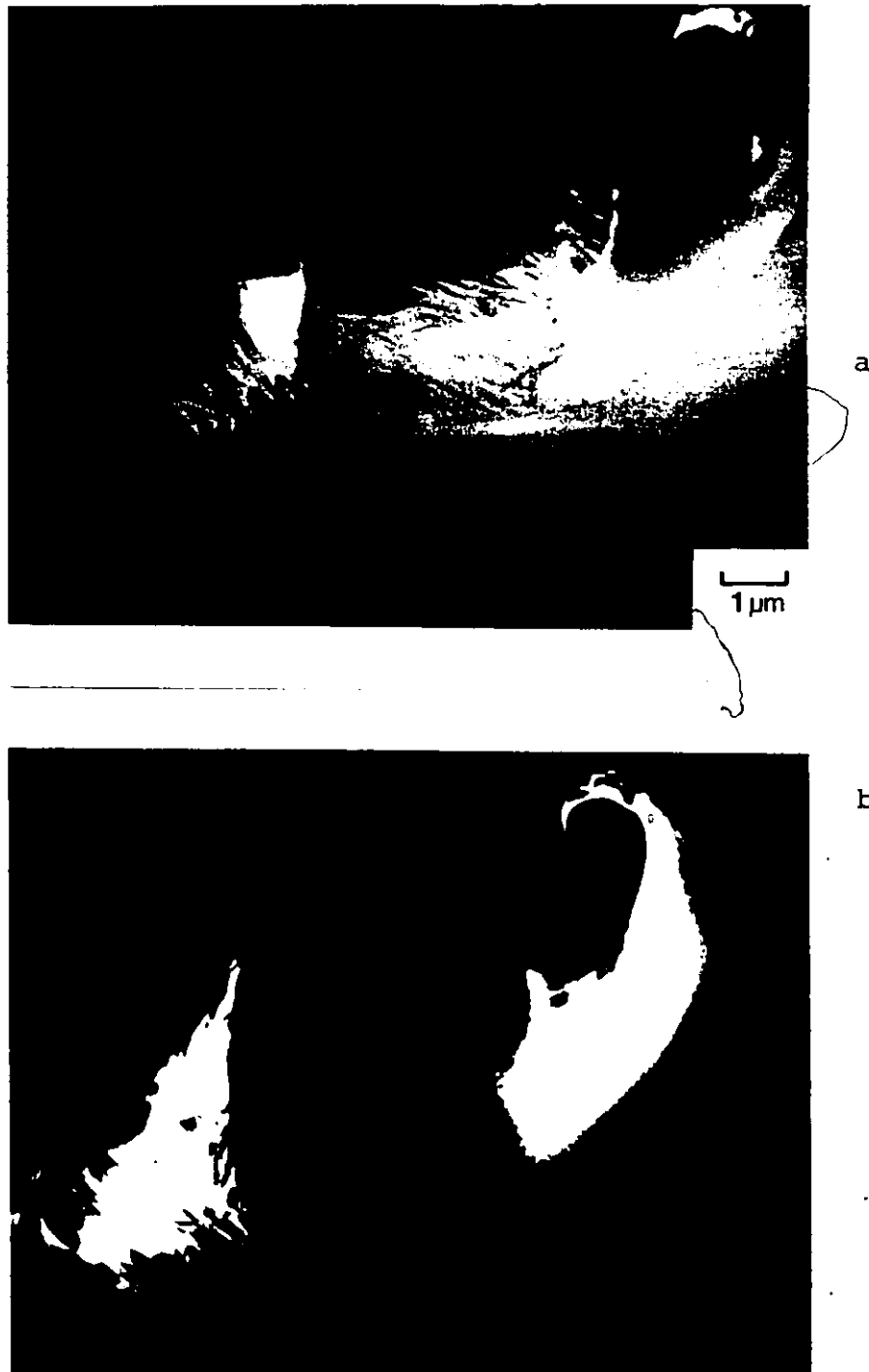
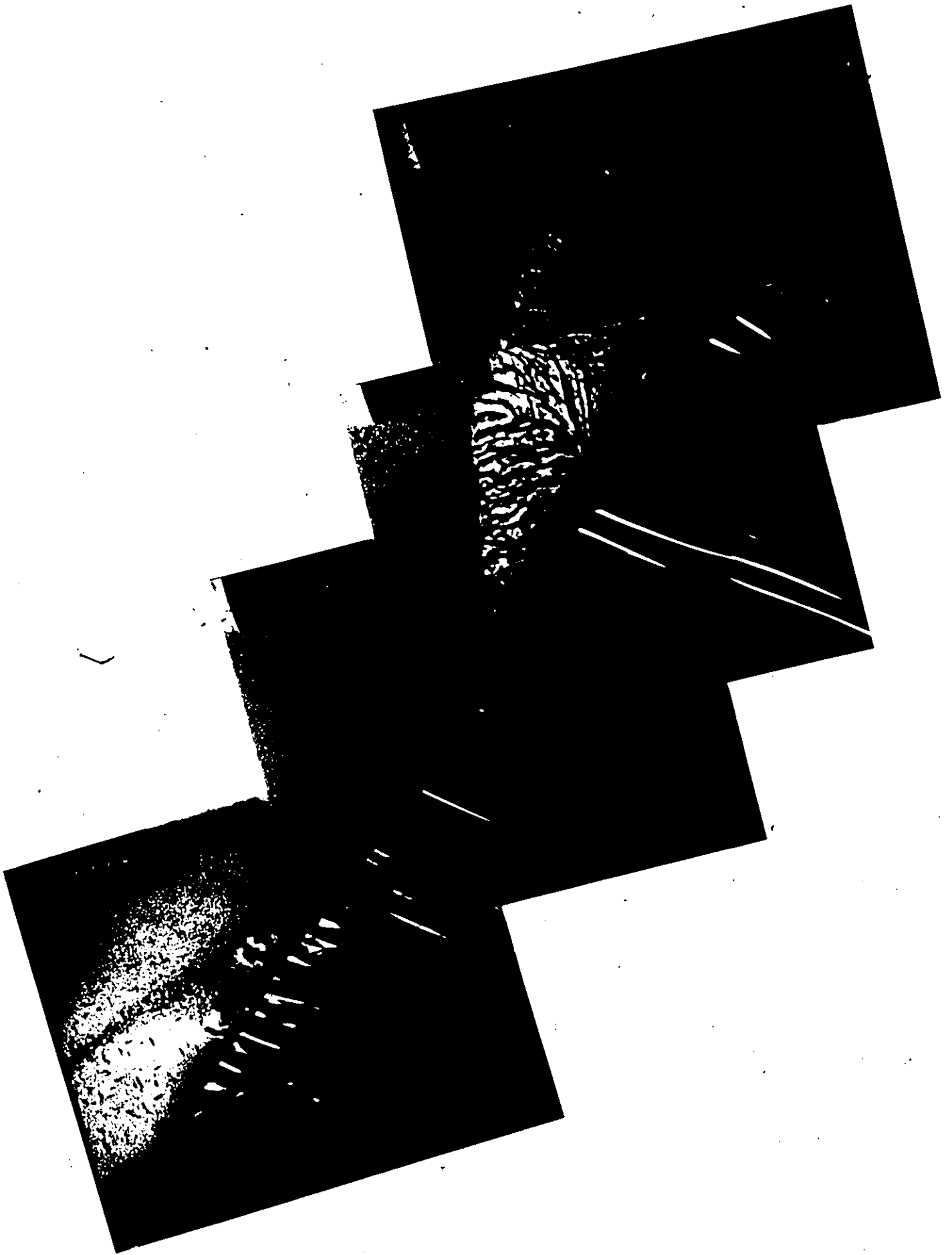


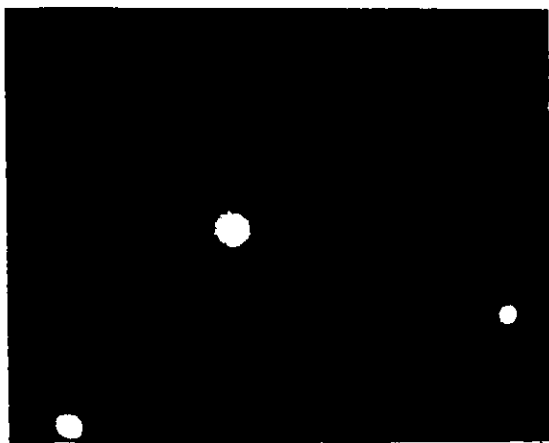
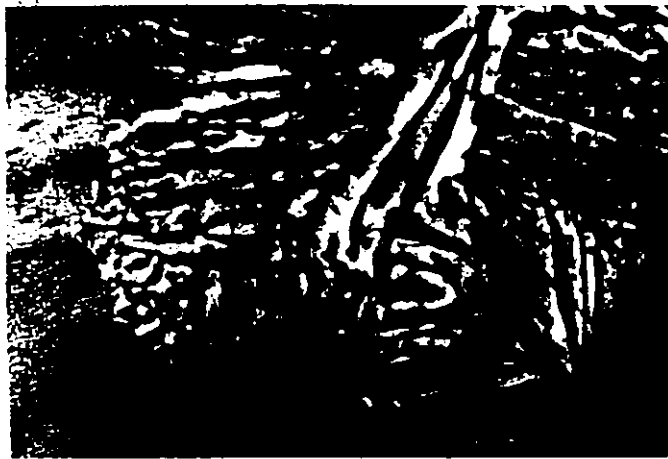
Fig. 49 a) STEM annular dark field image of a double seam morphology. b) Centered dark field image with a right hand parent grain reflection. 478K, 300 s, 5K ×.



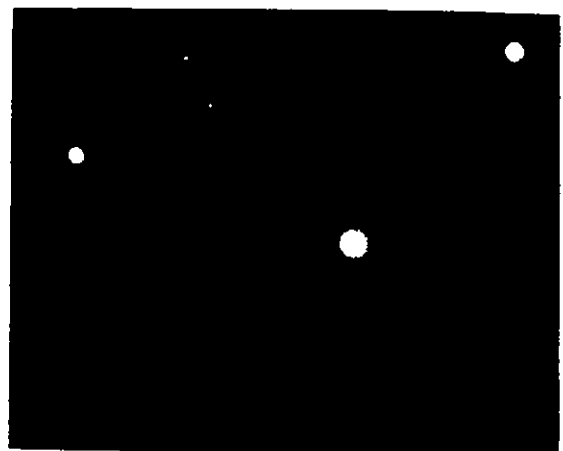
Fig. 50 a), BF image of a double seam morphology b) and c) Matrix CDF from each grain of a) showing crystallographic orientation relationship, between parent grain and discontinuous cell.

Fig. 51 a) A preexistent colony has grown in situ a second stage
20 K x





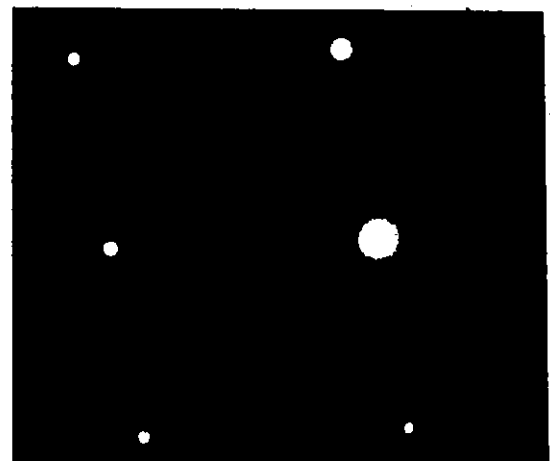
Third stage



Second stage

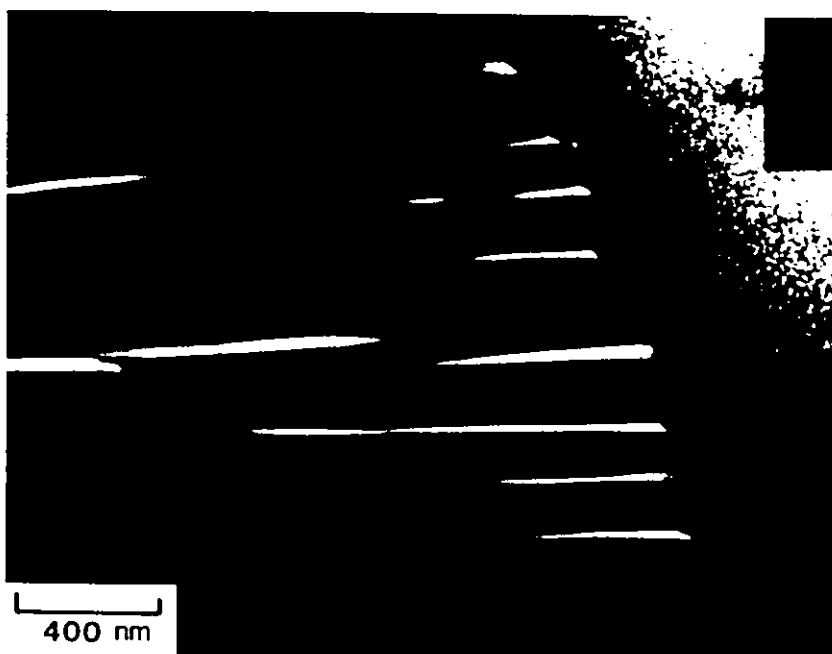


Original cell

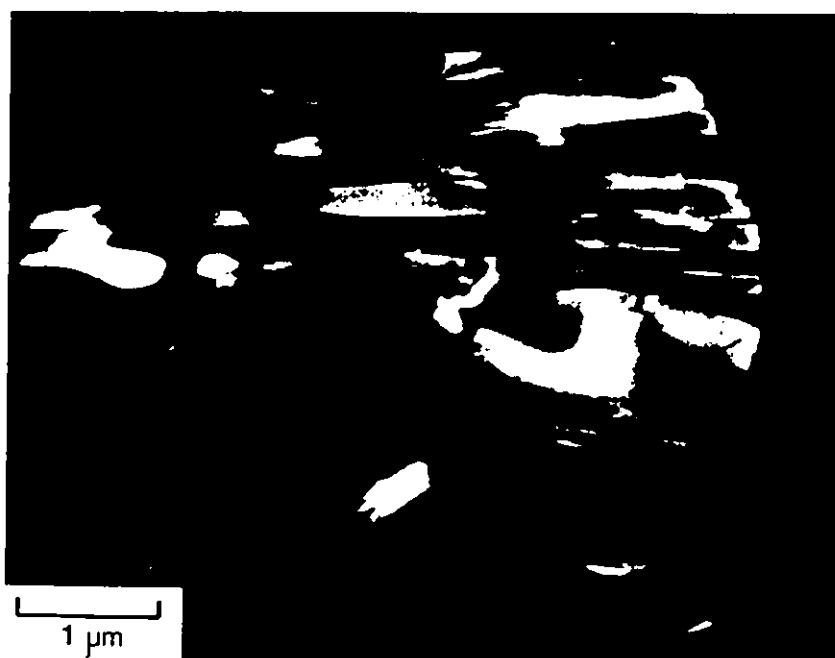


Parent matrix

Fig. 51 b) A third stage. The selected area diffraction patterns show that the cell/matrix orientation has been maintained.



a



b

Fig. 52 a) Bright field; b) Transformed cell centered dark field image showing strain fields.

The renucleation event could also be assigned to microstructures from specimens annealed in the bulk; in this case, however, there is the uncertainty due to sectioning effect.

4.1.6 Stability of the discontinuous product

Two main effects were noted when an annealed and quenched microstructure is reheated (to about 50°C) during the ion thinning process:

- a) Spherodisation of the discontinuous precipitate.
- b) Decomposition of the depleted α' phase. Both these effects are shown in figures 53 and 54.

4.2 Microanalysis and Microdiffraction Results

4.2.1 The steady state lamellar reaction front

Since several lamellae were analyzed, following the procedure outlined in section 3.7.3, the description of individual details is omitted here. Rather, the general conditions are given: Two fixed annealing treatments were chosen, 428K, 300 s, and 478K, 300 s. The analyzed lamellae corresponded to typical cell configurations. In some cases neighbouring lamellae, i.e. belonging to the same colony, were independently analyzed. These cases will be pointed out in the corresponding figure caption. The position of microanalysis (unless otherwise stated in the remainder of the text) accompanied the reaction front at \sim 50 nm from this in the α' lamella.

For the subsequent computation, the parent grain composition

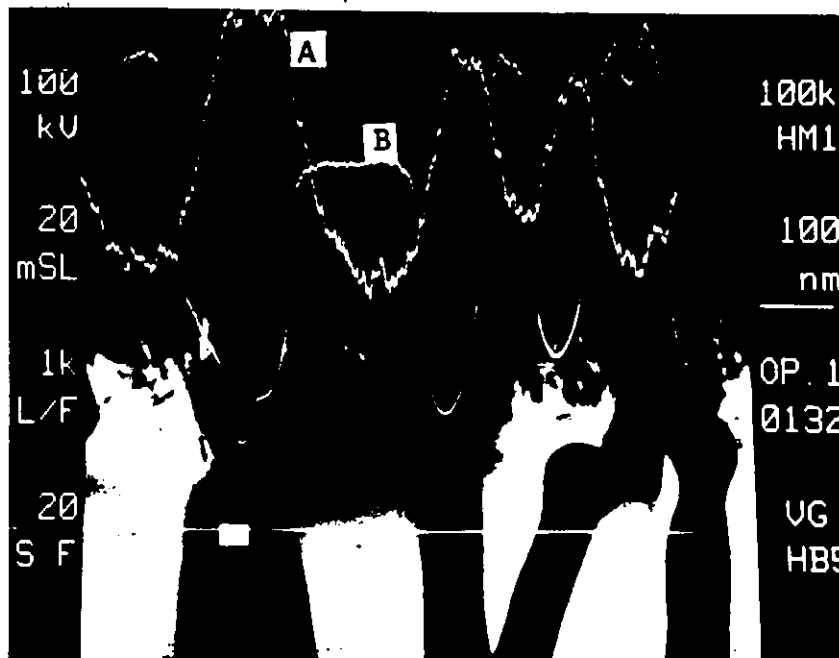


Fig. 53 Al-28 at.% Zn, 473K, 150 s. Ion thinned during 10 h. Spheroidisation is evident. Intensity curves produced by the electron beam traversing the line drawn through the square indicator mark.
A. Zn x-ray intensity.
B. Electron intensity that produced the picture.

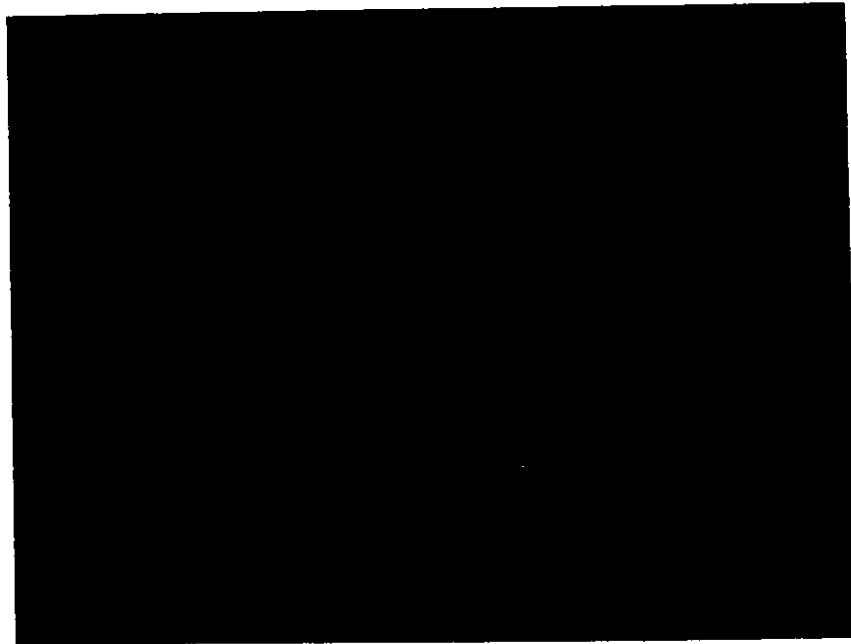


Fig. 54 Al-22 at.% Zn. a) treated and thinned identically as in fig. 53. b) 428K, 240 s and ion thinned. The decomposition of the depleted α' is clear. 200K \times .

during the steady state growth, x_s , was assumed equal to coherent spinoidal equilibria at 428K, and to the chemical spinoidal at 478K. This choice is justified in the next section. The value for the former was taken from Rundman and Hilliard¹⁸⁹ and for the latter from Ungar et al.¹⁶³. The parameters a and x_3 were calculated through non linear regression analysis of Cahn's equation (4) using the measured local values of v , s and $x(z)$ as input data.

The results are summarized in tables IV and V. Next, some typical analyses are illustrated with their corresponding electron micrographs, composition profiles and microdiffraction patterns, each accompanied by a concise explanation.

a) Annealing temperature 428K, $x_0 = 0.143$ (Table IV)

• Lamella No. 7

Its characteristic and composition profile are shown in fig. 55. The CBMD patterns in the same lamella do not change despite the 31% composition difference. There is however, a slight but discontinuous change with respect to the orientation of the two neighbouring lamellae. Fig. 35 gives a low magnification view of the cell containing these lamellae. The regular, steady state character is noted.

• Lamella No. 8

An ADF STEM micrograph of its containing cell and a high magnification image of this lamella along with its composition profile is given in fig. 56.

Table IV. Details of cells studied
428K ageing temperature

Lamella Studied	S_{α} nm	v nms^{-1}	a	X_3 at. % Zn	$KD_b \delta$ $\text{nm}^3 \text{s}^{-1} \times 10^{-4}$	P
1	160	20.1	6.3 ± 0.3	7.4 ± 0.8	8.07	0.874
{ 2	280	14.0	3.7 ± 0.6	6.9 ± 1.5	29.6	0.938
{ 3	310	14.0	3.9 ± 0.8	6.9 ± 1.5	34.5	0.935
4	320	23.4	2.4 ± 0.7	6.6 ± 1.5	99.8	0.969
5	165	43.3	3.7 ± 0.5	7.0 ± 1.2	31.8	0.939
{ 6	200	43.3	3.8 ± 0.2	7.8 ± 0.6	43.3	0.936
{ 7	210	43.3	5.0 ± 0.2	7.6 ± 0.7	38.2	0.908
8	140	16.6	7.2 ± 0.3	6.2 ± 1.0	4.54	0.856
9	175	27.0	7.8 ± 0.6	6.8 ± 1.4	10.6	0.838

Lamellae in the same colony are indicated by the brackets.

Table V. Details of cells studied
478K ageing temperature

Lamella Studied	S_{α} nm	v nms^{-1}	a	X_3 at. % Zn	$KD_b \delta$ $\text{nm}^3 \text{s}^{-1} \times 10^{-4}$	P
1	1065	18.6	0.65±1.45			
2	710	24.0	4.14±0.3	6.7±0.3	29.2	0.929
3	410	24.0	1.3±0.3	7.0±0.6	31.0	0.989
4	430	29.3	2.18±0.3	8.2±0.6	24.8	0.974
5	580	16.0	2.7 ±0.05	7.5±0.3	19.9	0.961
6	500	5.8	0.75±0.3	8.1±0.5	19.3	0.995
7	245	43.3	2.4 ±0.11	7.6±0.4	10.6	0.968
9	200	43.3	2.3 ±0.2	7.4±0.7	7.5	0.970
10	480	44.0	4.0 ±0.3	6.7±0.2	25.3	0.931
11	510	44.0	3.8 ±0.1	7.3±0.5	29.8	0.936
12	510	44.0	3.3 ±0.1	7.3±0.4	34.2	0.948
13	400	40.6	7.6 ±0.8	7.6±1.1	8.5	0.844
14	520	40.6	8.6 ±0.8	7.2±1.7	12.7	0.822
17	280	41.56	4.44±0.3	6.3±0.8	7.35	0.921

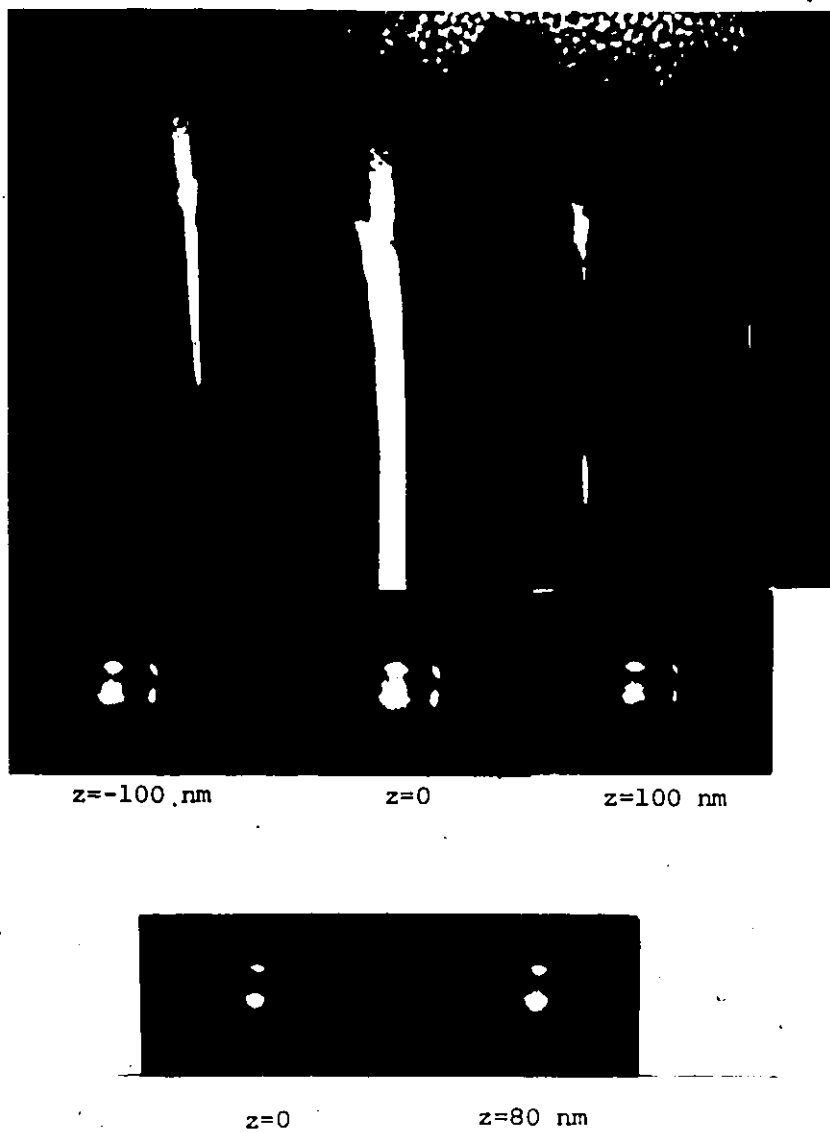


Fig. 55 a) Details of neighbouring lamellae #6 and #7. CBMD patterns of the microanalysis position are shown.

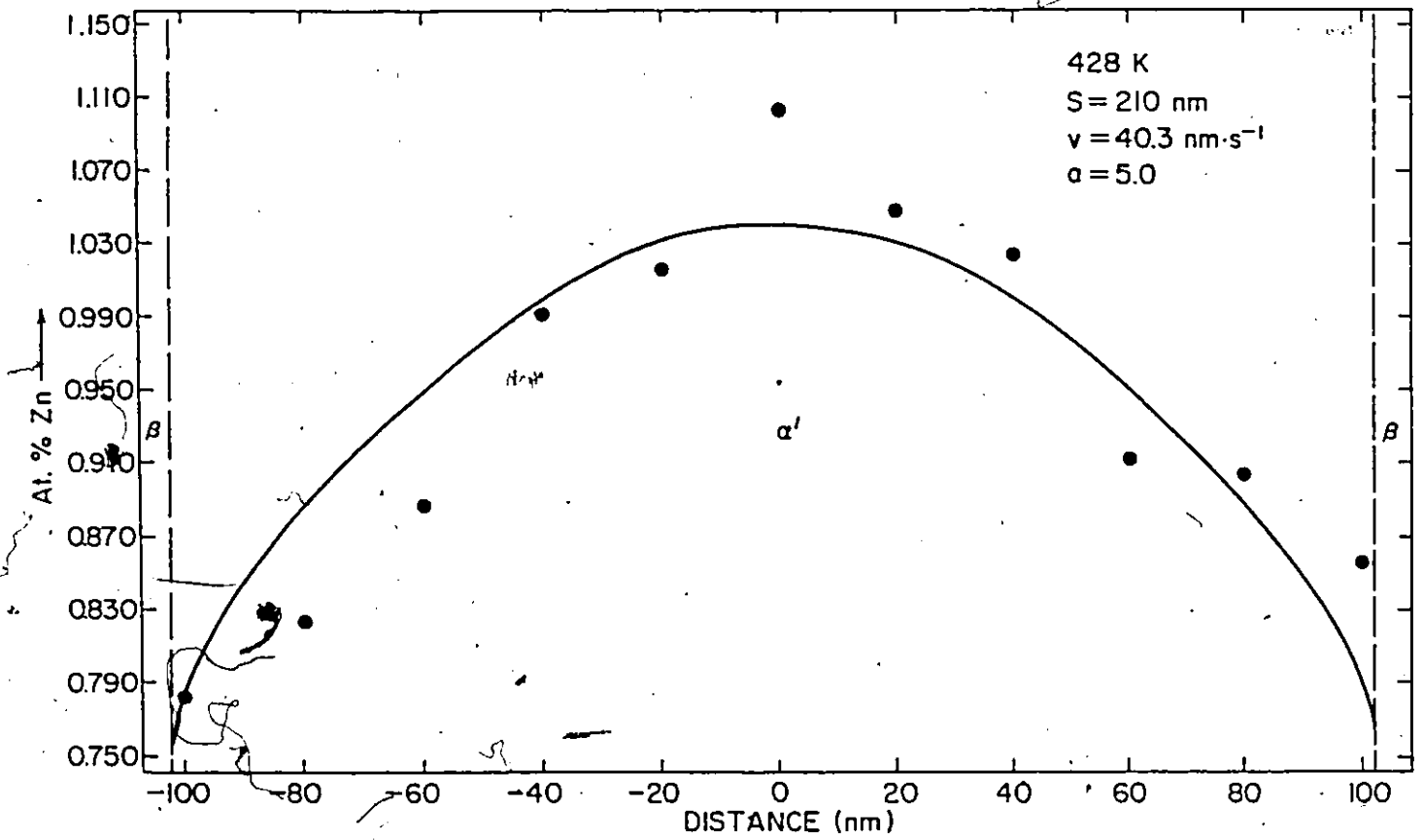


Fig. 55 b) Composition profile of lamellae #7.

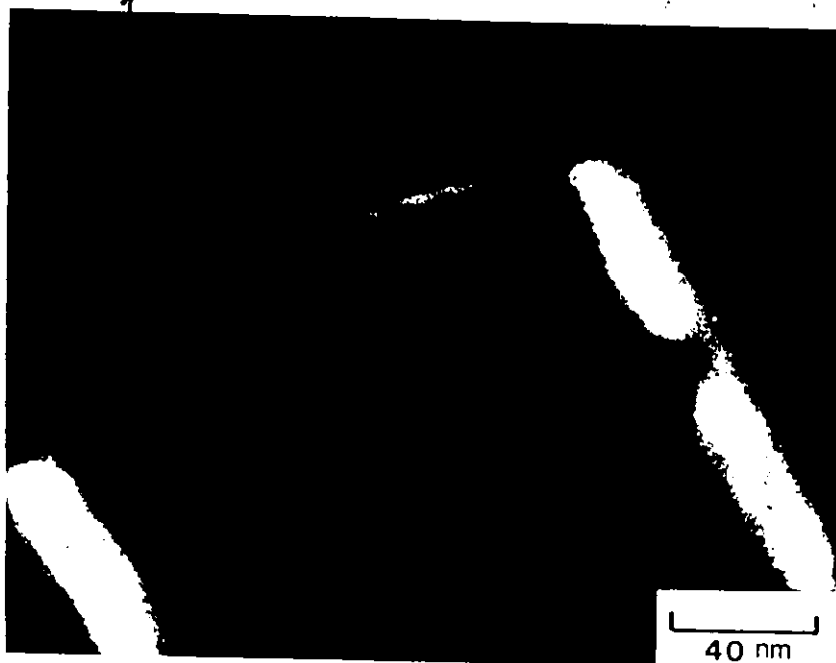
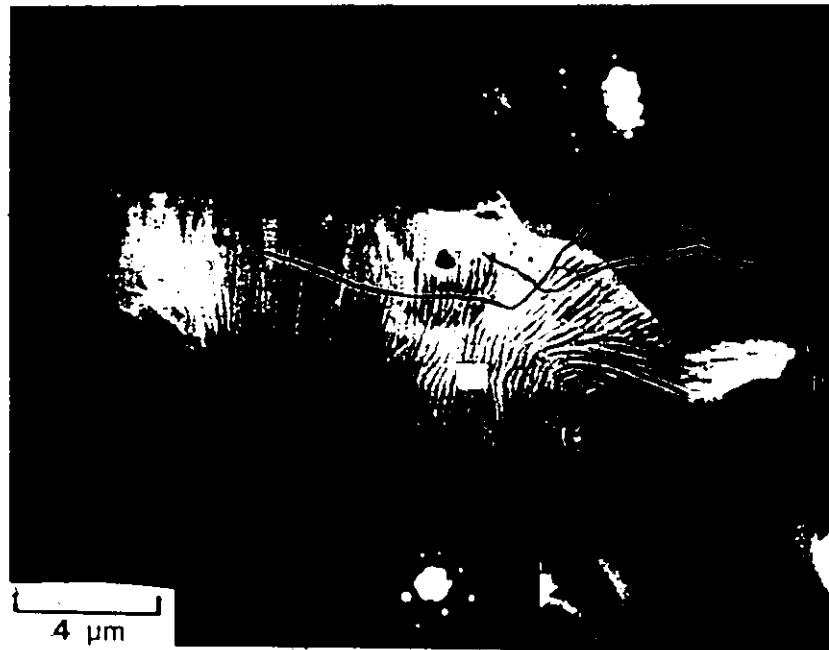


Fig. 56 a) ADF image of cell containing lamella #8, imaged at 500K × in b). Slight contamination of the position of analysis can be observed.

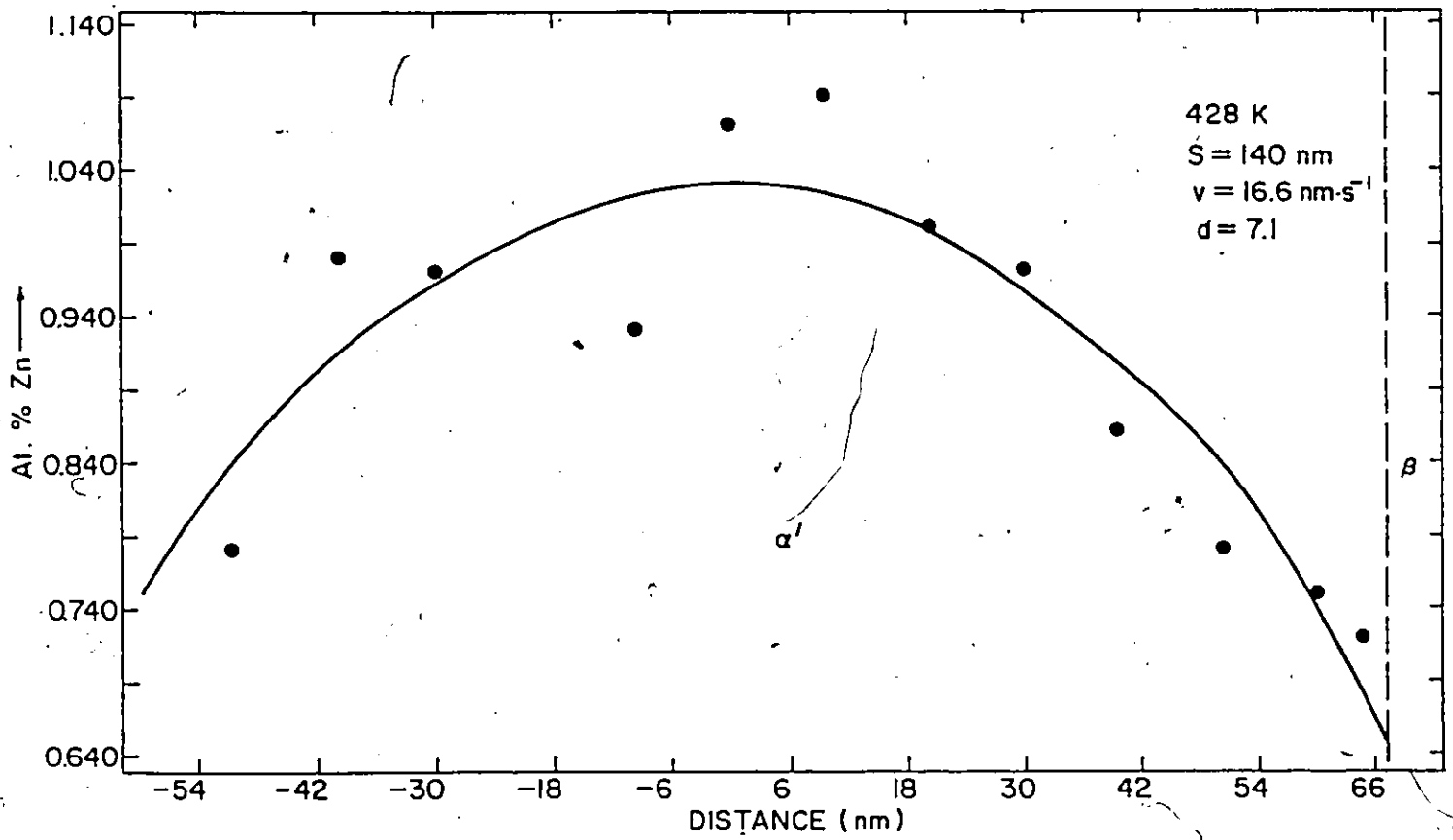


Fig. 56 c) Composition profile of lamella #8.

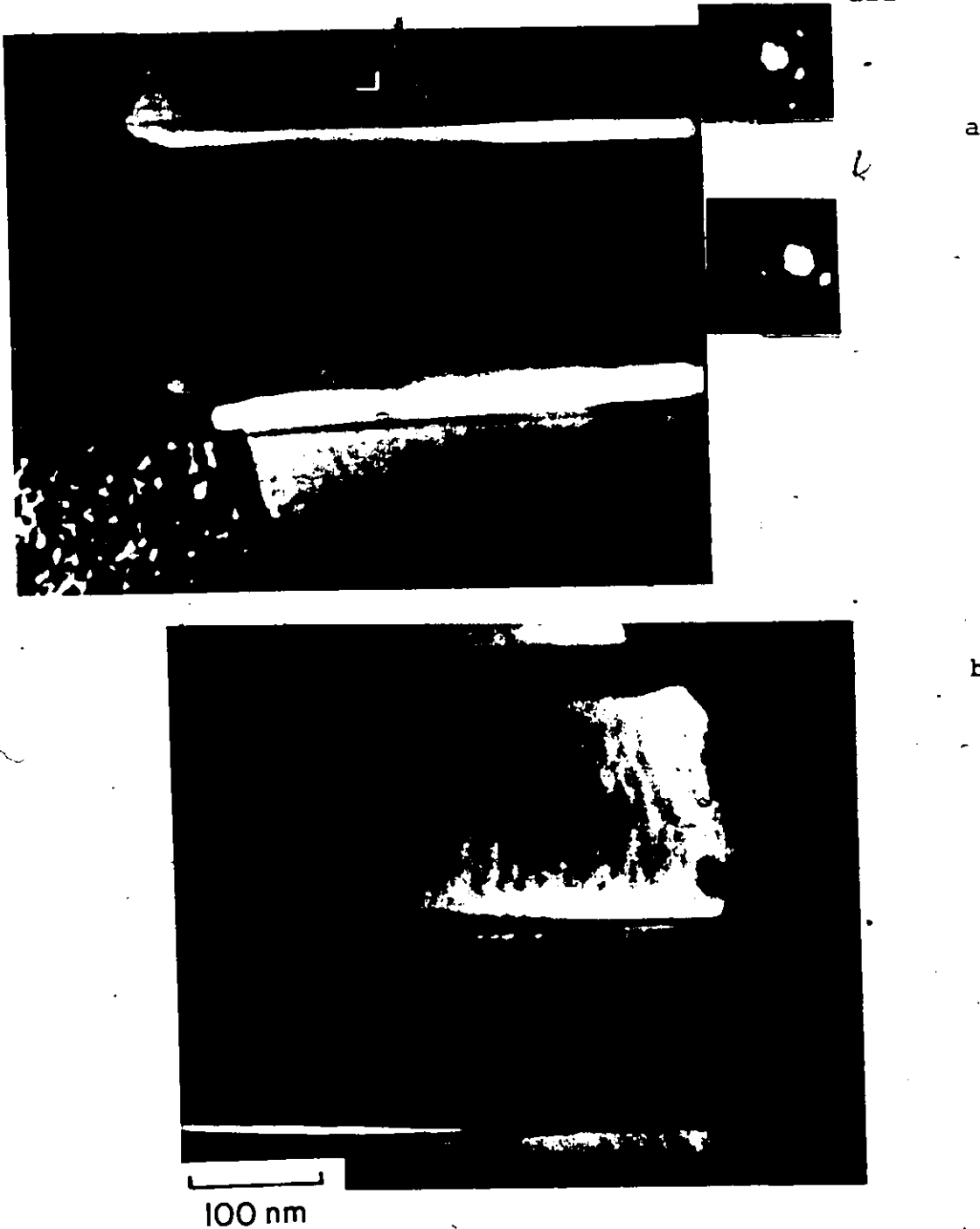


Fig. 57 a) BF image of reaction front containing lamella #9. CBMD pattern from this and from its lower neighbour are included. Note the parent grain spinoidal microstructure.
 b) CDF image with a product matrix reflection emphasizing the sharp change in diffraction contrast.

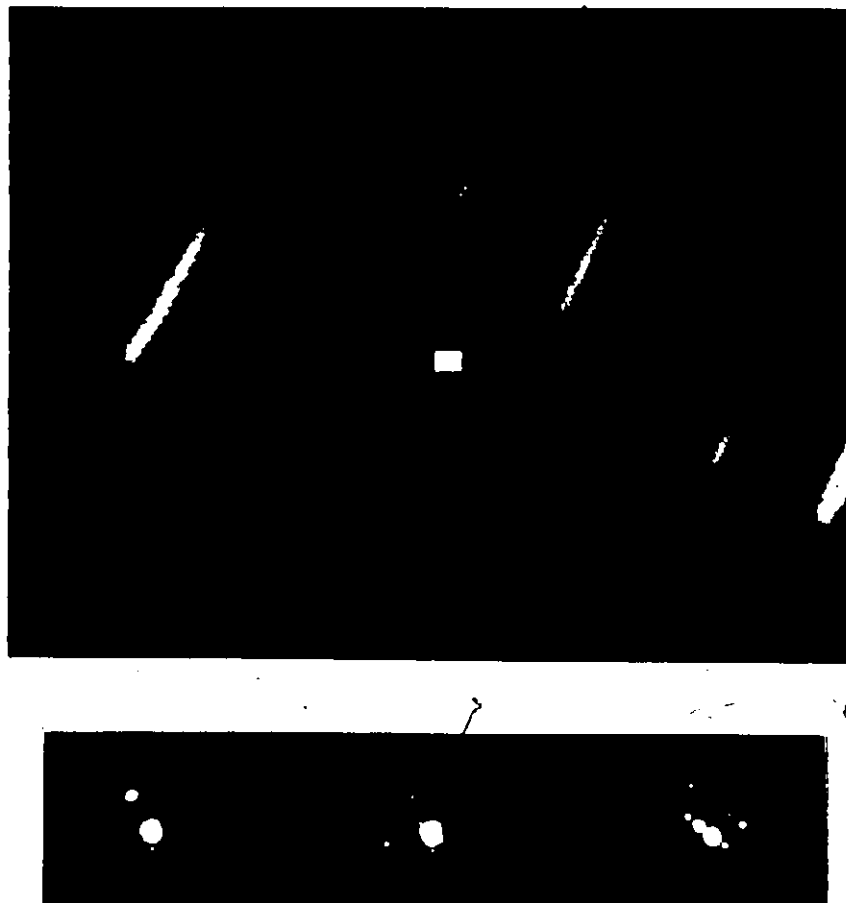


Fig. 57 c) The same reaction front imaged in "low mag mode" (objective lens off) with "parallel beam" microdiffraction patterns from the marked individual lamellae and from the parent grain.

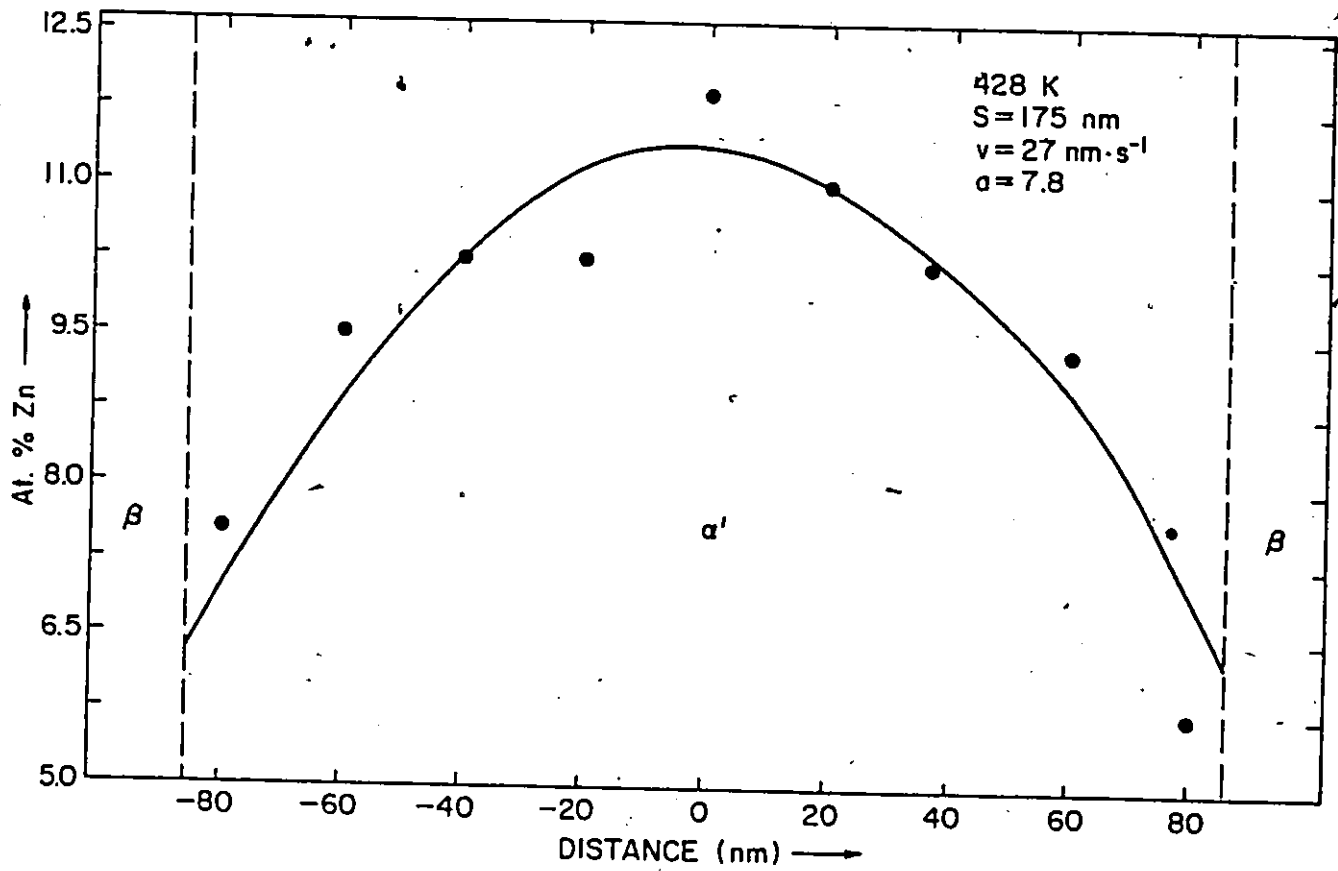


Fig. 57 d) Composition profile of lamella #9.

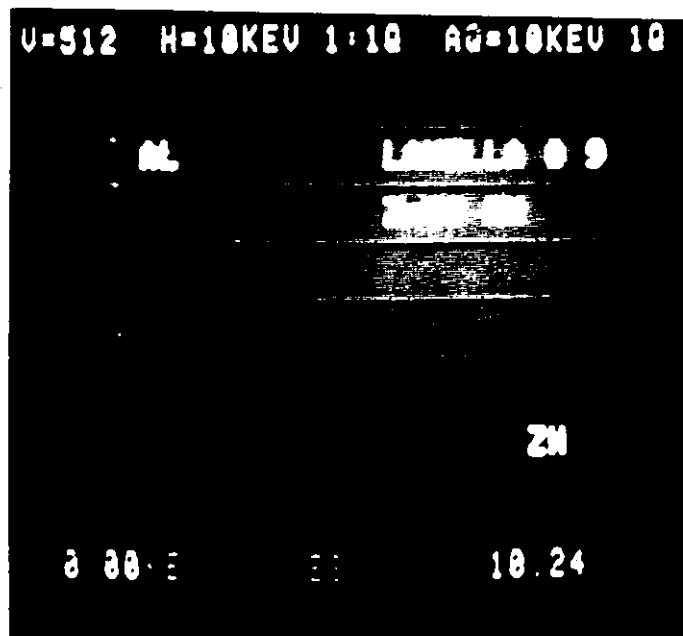
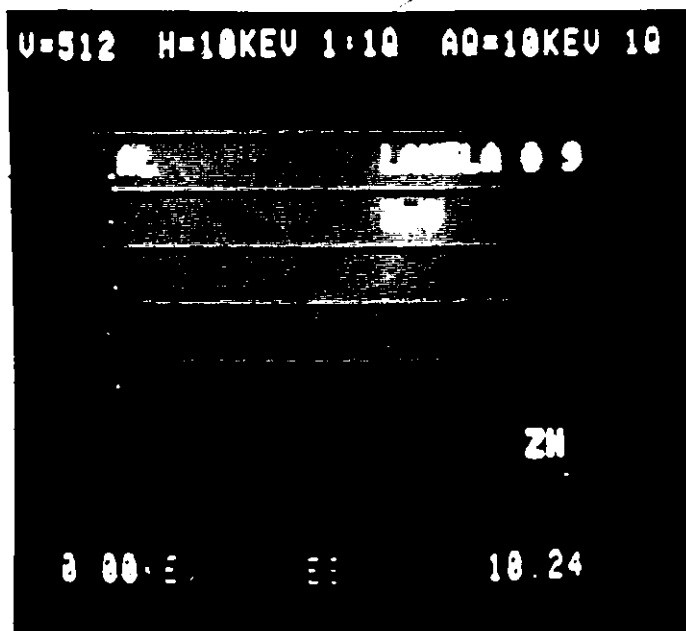


Fig. 57 e) Individual x-ray spectra obtained at center ($z=0$) and close to the edge ($z=80$ nm) of lamella #9

- Lamella #9

Detailed microanalytical, Fig. 57d,e, and microdiffraction results, Fig. 57 a-c, are given. Gridson CDF imaging is used to show evidence for the misorientation between neighbouring lamellae of the reaction front. It is also noted that CBM patterns from these lamellae show loss of detail compared with the "parallel beam" microdiffraction patterns.

- b) Annealing at 478K, $x_0 = 0.138$ (Table V)

A well formed colony is shown in fig. 58a. In fig. 58b, a variety of events are better observed: a steady state spacing is approached by the transforming system with the interface bowing towards the parent grain. Individually marked lamellae were analysed and are shown next.

- Lamella #1

Its spacing at the reaction front is very large, its α_0/α' curvature is bent backwards, its composition profile far from a characteristic steady state, fig. 59.

- Lamella #2

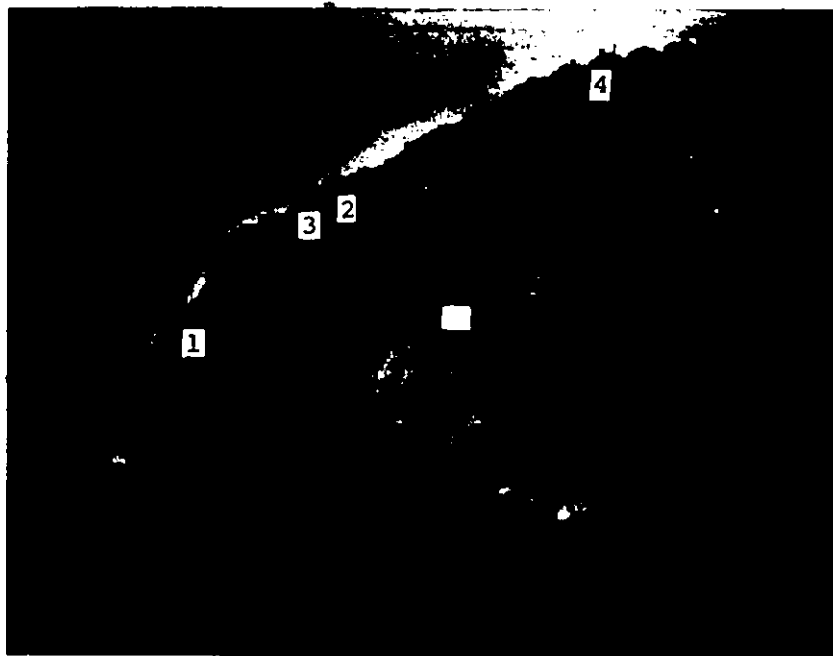
Its interface seems to have adopted a steady state growth shape. This is supported by its composition profile, fig. 60.

- Lamella #4

Was grown at a higher rate than the previous. Its spacing is smaller. Both α_0/α' curvature and composition profiles suggest a steady state growth, fig. 61.



a



b

Fig. 58 a) A well formed colony. Inset SADP are from parent and product grains.
 b) The same cell. The marked lamellae are shown individually with their composition profiles in Figures 59-61.

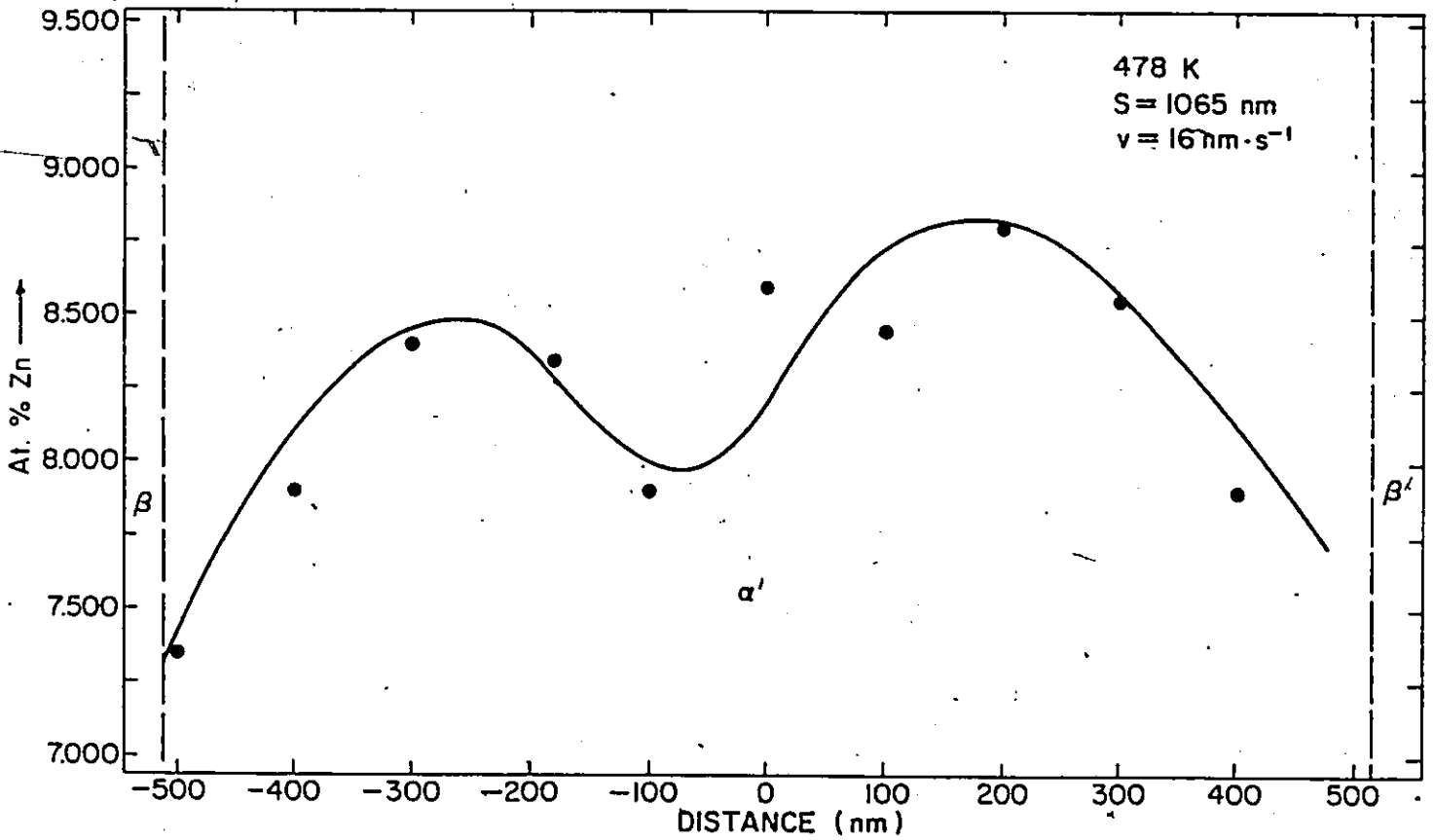
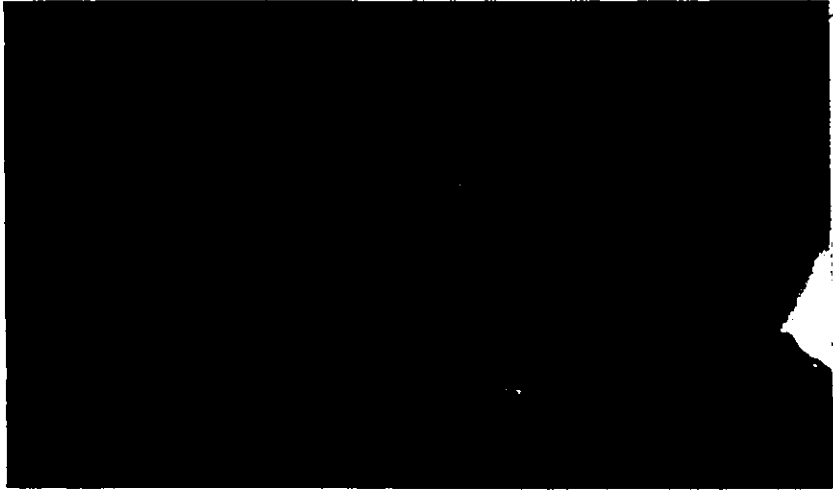


Fig. 59 Lamella #1 and its composition profile. Grain boundary diffusion controlled steady state growth are not applicable to this case.

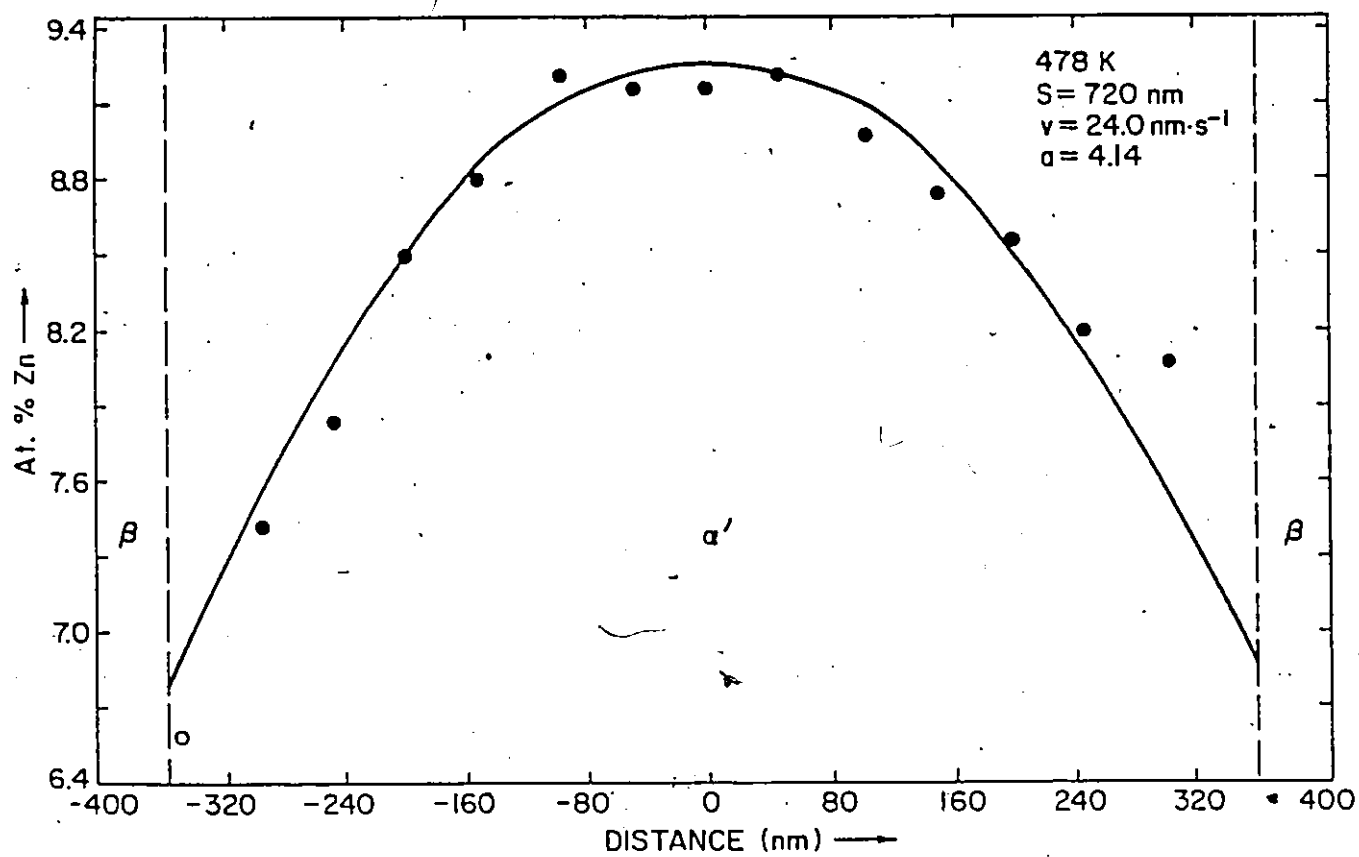


Fig. 60 Lamella #2 and its composition profile. The steady state growth process is well characterized.

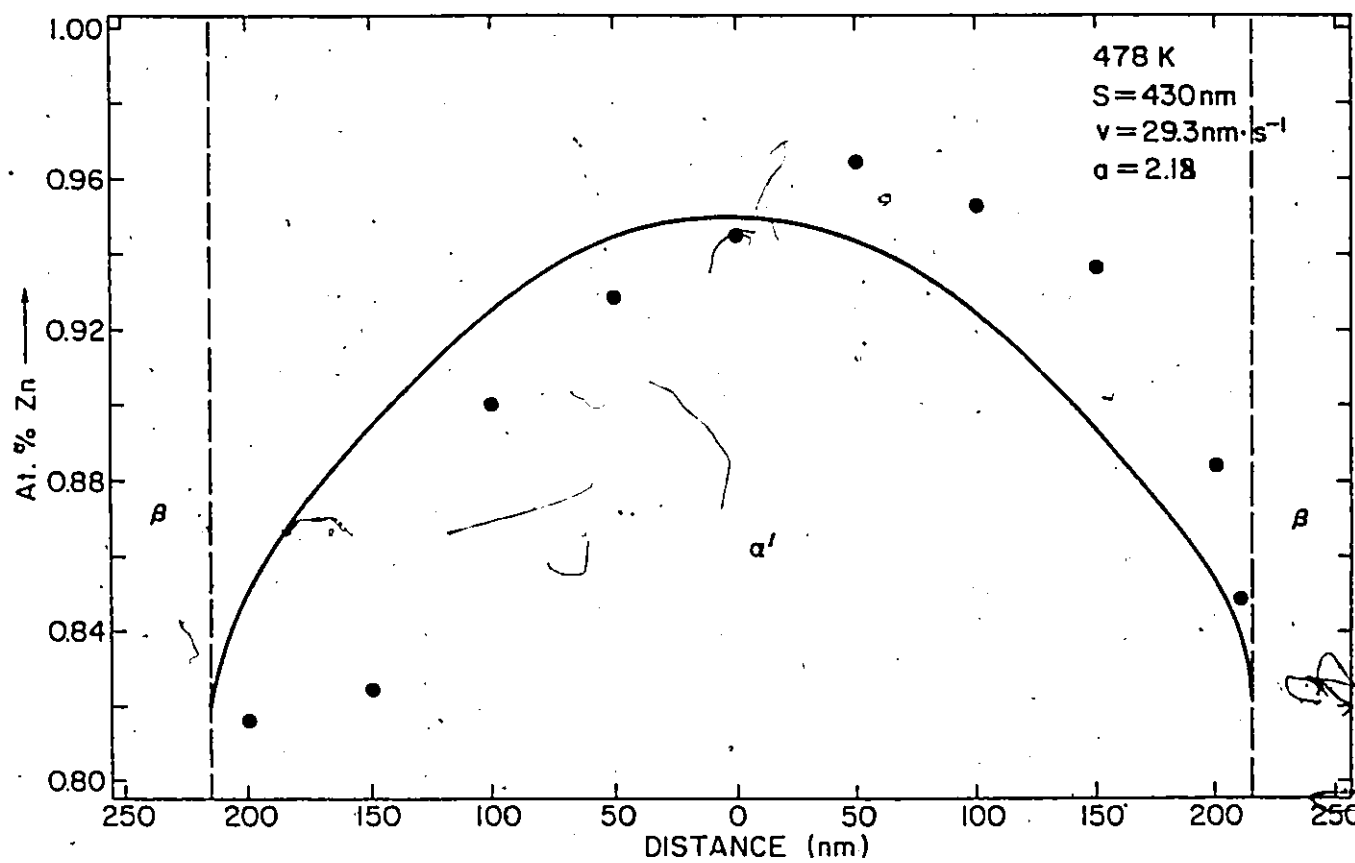


Fig. 61 Lamella #4 and composition profile. Note the coarsened spinodal microstructure in the parent grain.

• Lamella #5

Belongs to the cell shown in figure 34 growing in s-shape. Its composition profile is well characterized by the steady state growth, as shown in fig. 62.

• Lamella #12

From a typical reaction front with steady state spacing, fig. 63a, the composition profile of lamella #10 is shown in fig. 63b.

• Lamella #17

The last example for microanalysis and microdiffraction is given with lamella #17, fig. 64a. The CBMD* patterns are not changed although coming from positions of different Zn concentration as indicated in the composition profile, fig. 64b. The reaction front is shown in BF mode, fig. 64c, and in the CDF mode, with a product matrix, fig. 64d, and parent grain reflection, fig. 64e. The same reaction front is imaged in "low mag" mode (objective lens off) as shown in fig. 64f, along with the "parallel beam" microdiffraction patterns. The misorientation between neighbouring lamellae can be appreciated.

4.2.2 The initial bowing of the grain boundary:

In section 4.1 DIGM precursor for discontinuous precipitation was noted. This suggestion is supported here: microanalysis in the depleted region, fig. 65, shows it is depleted in solute, although not to the equilibrium composition. The average concentration drop across the parent grain/depleted region is about 70%.

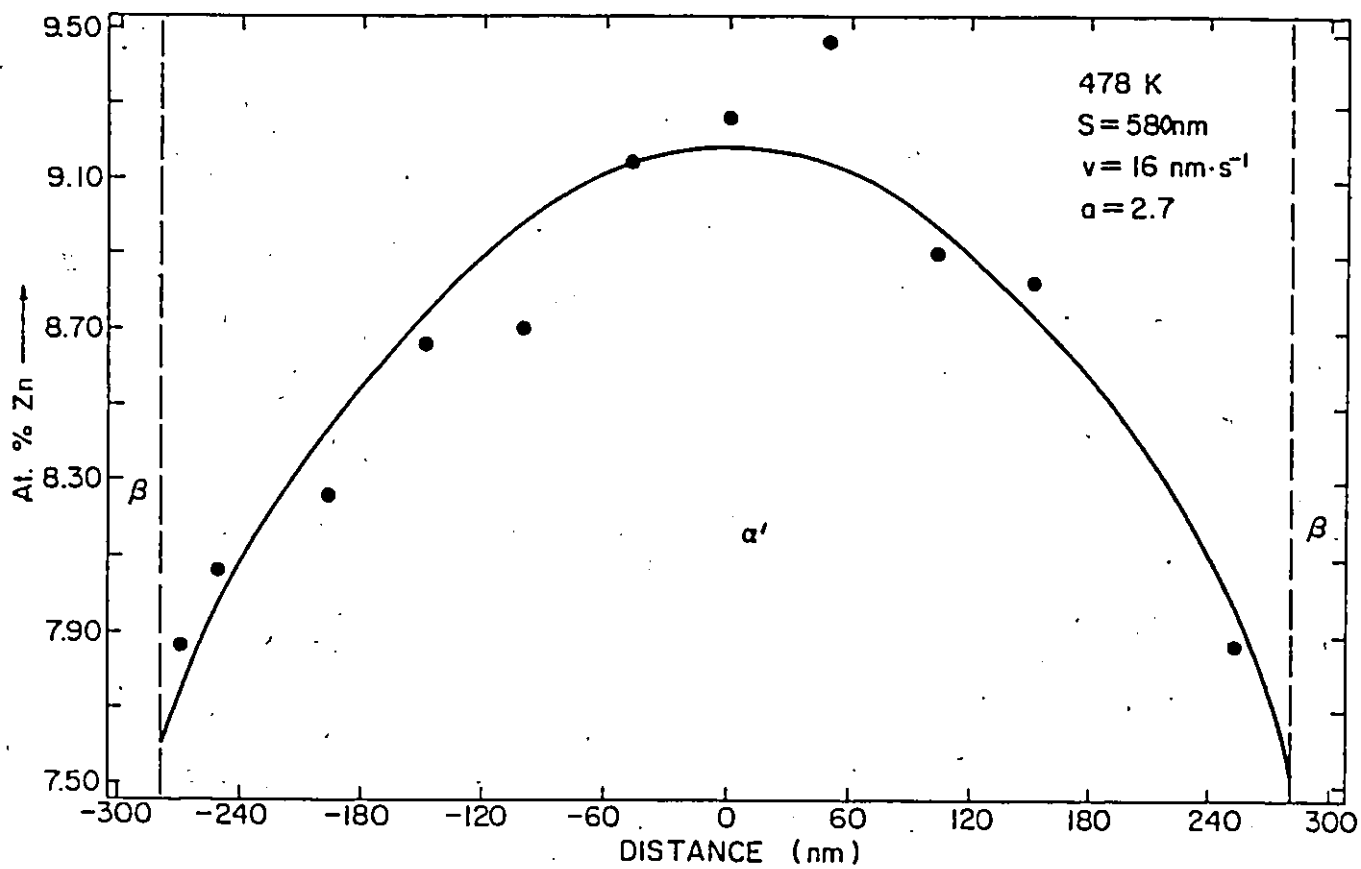


Fig. 62 Lamella #5 and composition profile. The colony containing the lamella is shown in fig. 34.



a

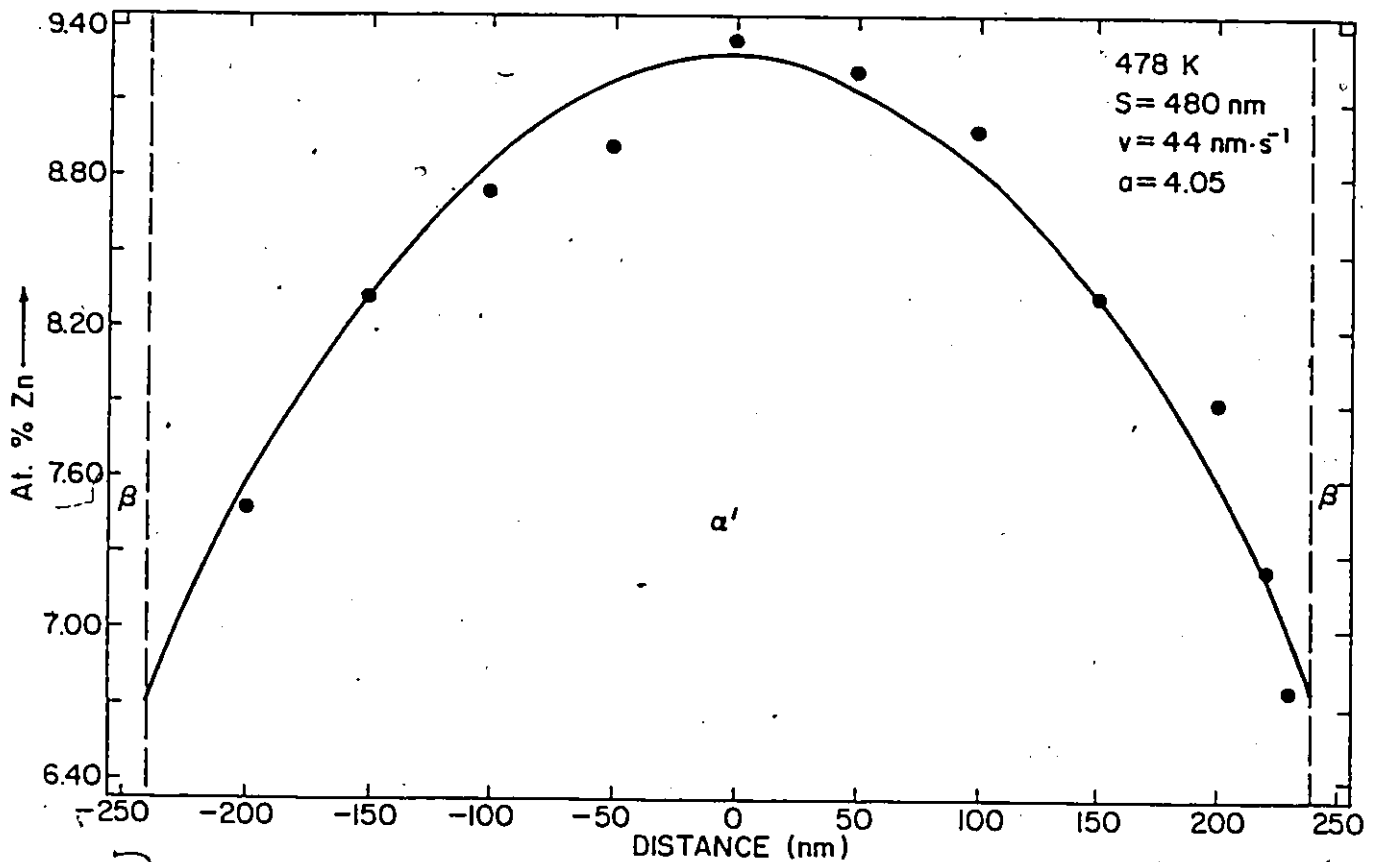


Fig. 63 a) A typical reaction front with steady state spacing. Note the precipitate at the interface which occurred after the preparation of the foil.
 b) The composition profile of lamella #10

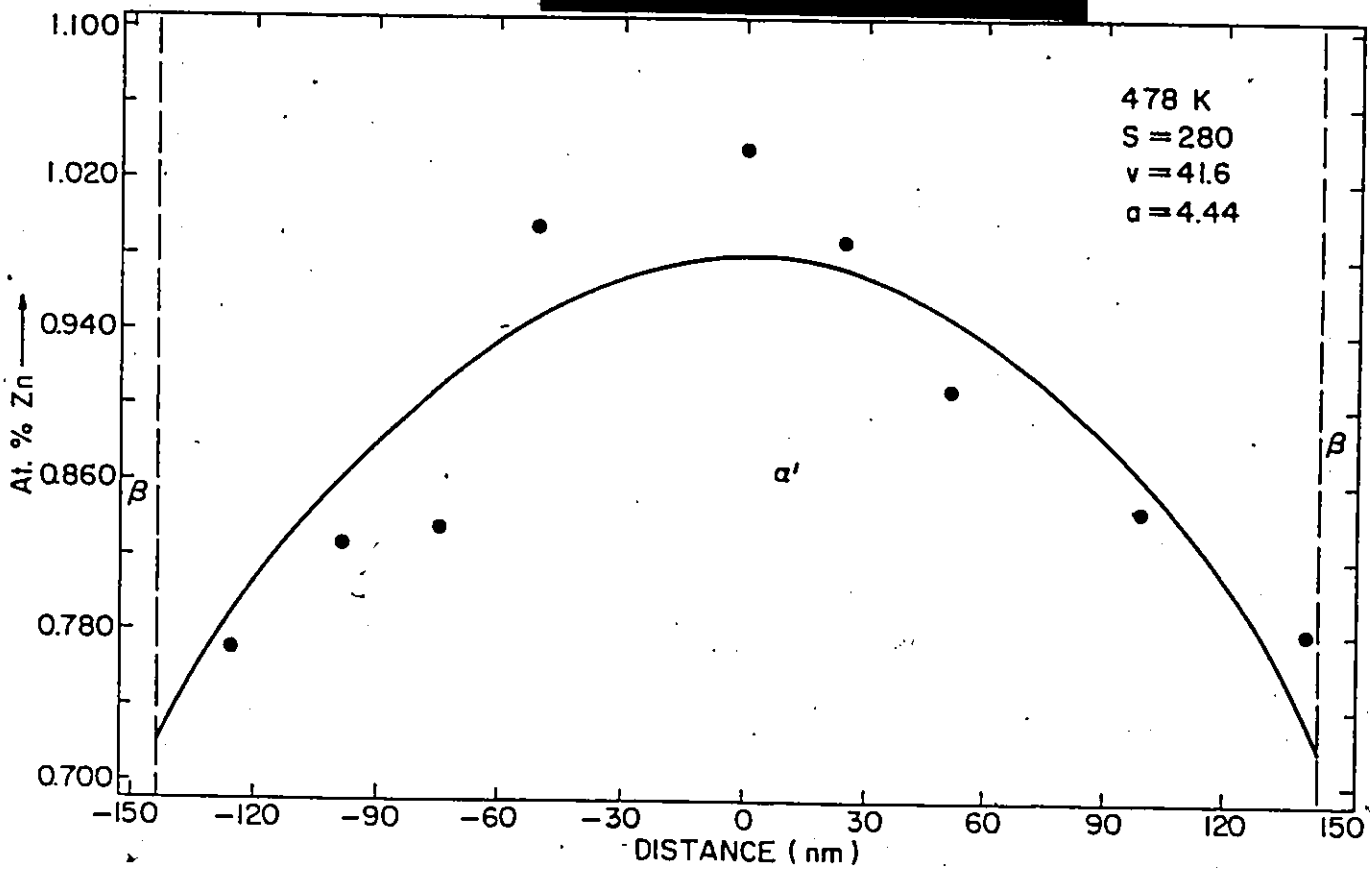
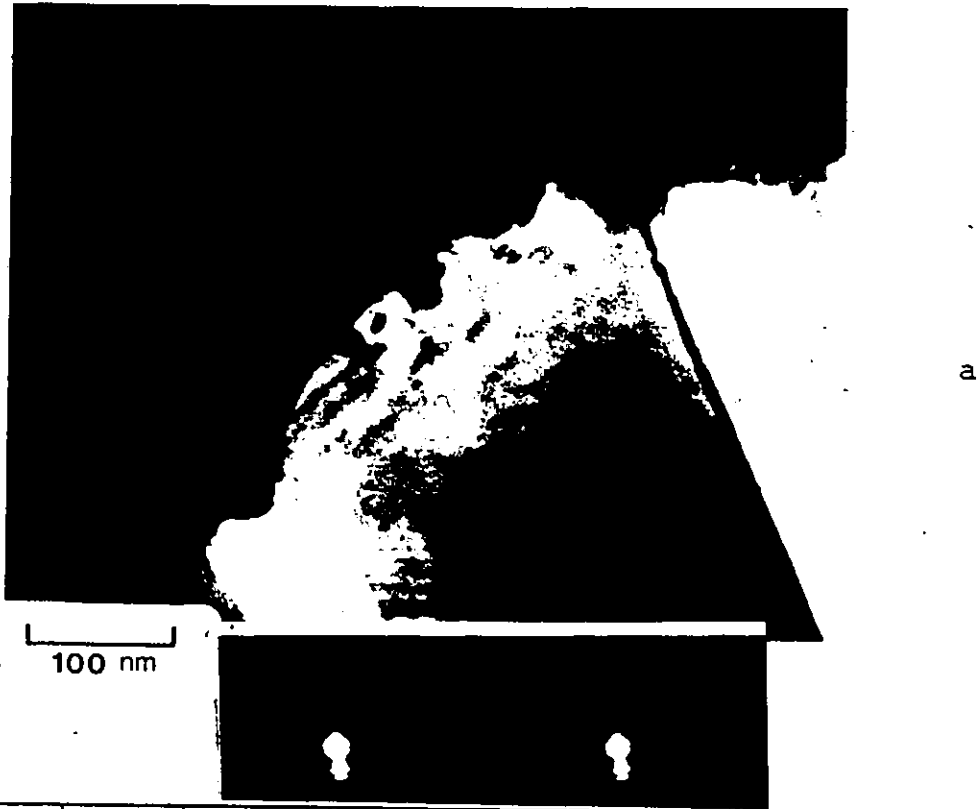
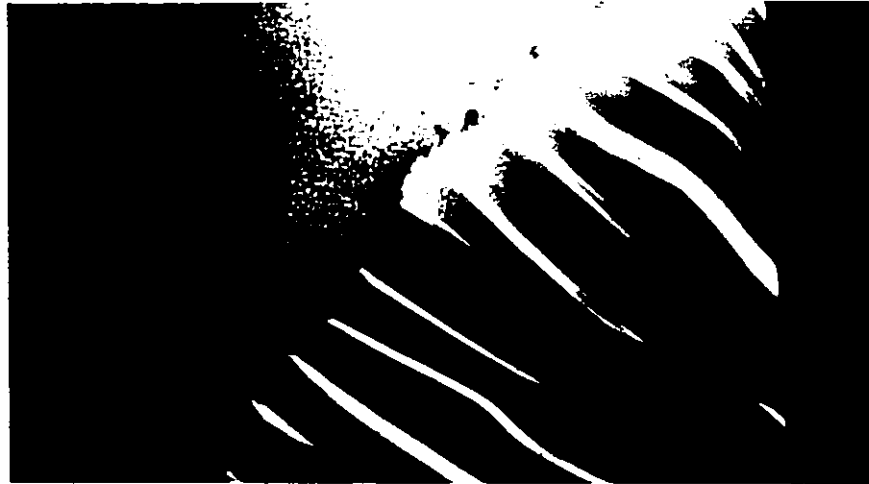
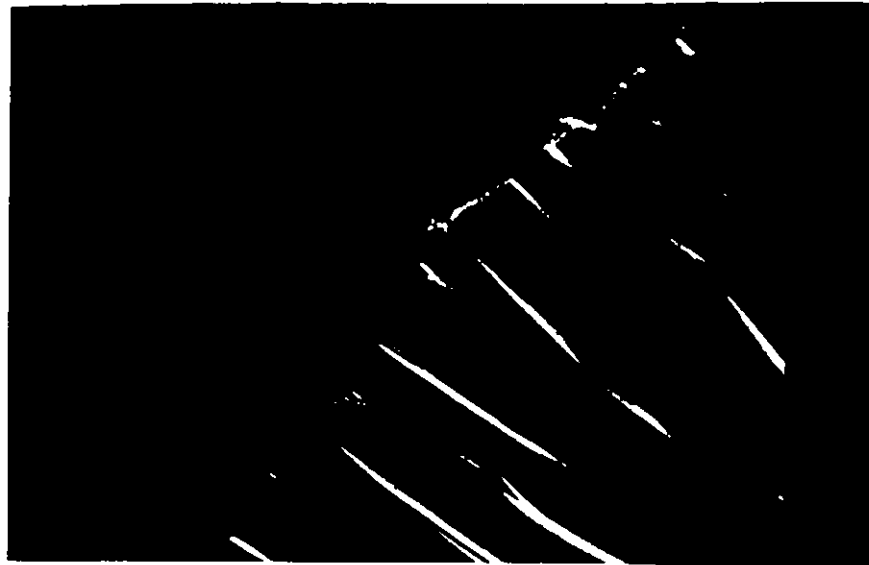


Fig. 64 a) STEM BF image of lamella #17.
b) Its concentration profile.



c



d



e

Fig. 64 c) BF image of colony containing lamella #17. CDF images with a product matrix reflection, fig. d), and with parent grain reflection, fig. e).

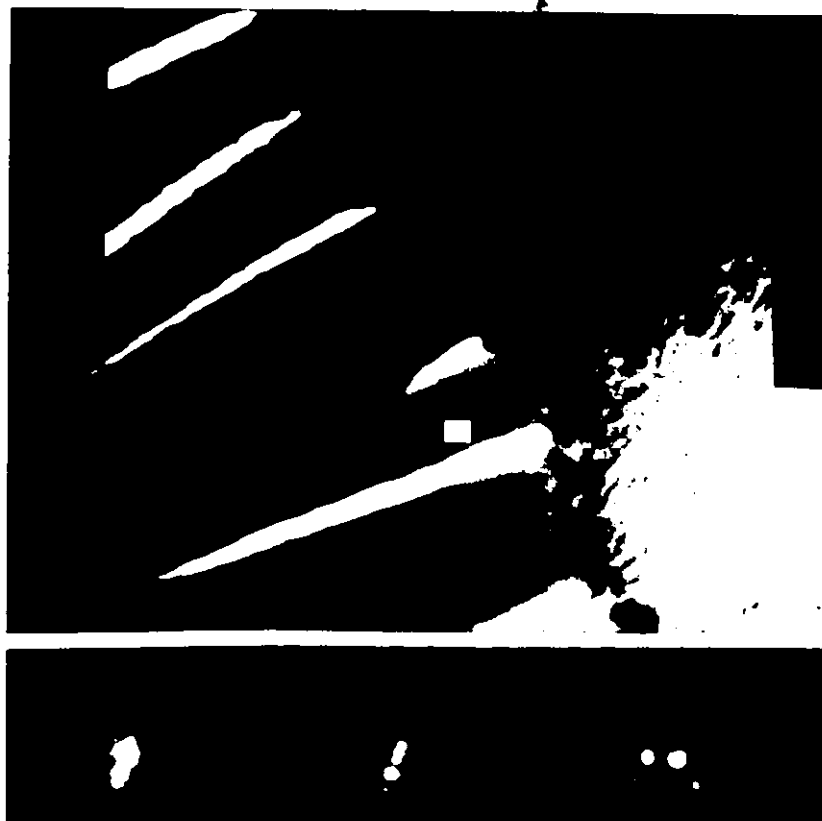
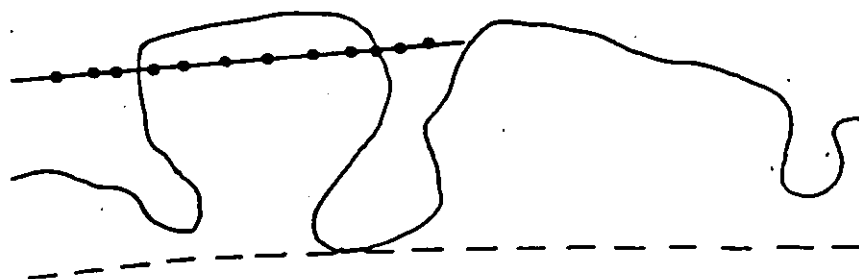


Fig. 64 f "Parallel beam" image and microdiffraction pattern from each marked and neighbouring lamellae or from the parent grain.



a



b

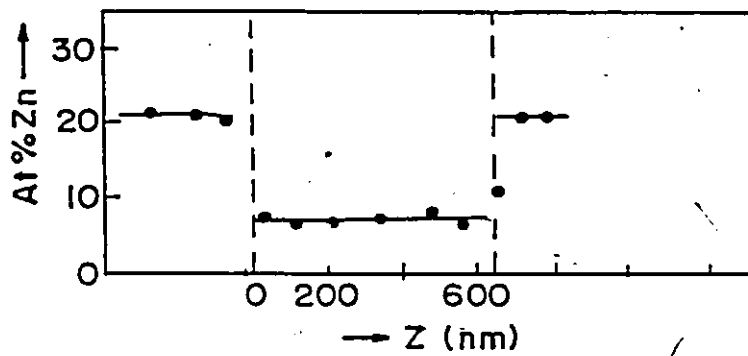


Fig. 65 a) DIGM structure in Al-22 at.% Zn, 428K, 300 s;
 b) Compositional STEM scan across the region
 shown in a).

DIGM during alloying in Al 22 at.% Zn is not frequently observed because the discontinuous precipitation takes place rapidly and the grain boundary then accelerates up to the steady state growth rate. With this factor in mind, well homogenized samples of the Al-12 at.% Zn alloy were examined after isothermal treatment at 428K. Although discontinuous precipitation was not present, boundary bowing was observed (see figures 66,67).

4.3 Other Modes of Decomposition

This section will be brief. First, in order of importance, is the fast, competing spinodal reaction in the parent α_0 which must reduce free energy to drive the discontinuous reaction. In fig. 68 a typical spinodal microstructure resulting from the lower standard annealing treatment, 428K, 300 s is shown. No microanalysis of the depleted α_0 is possible. It is reasonable, however, to assume that it gets depleted to, at least, the solubility given by the coherent spinodal. In fig. 69 it is shown that at the higher standard temperature, 478K, a coarsened spinodal microstructure has replaced the homogeneous α_0 . Microanalysis in the depleted region has been done and gives $x = 12$ at.% Zn which is lower than the spinodal value given by the curve proposed by Ungar et al., at this temperature, but close to the value in the coherent solubility curve proposed by Ardell et al.¹⁹⁰

The second mechanism of decomposition refers to the granular precipitation initiated at static grain boundaries. This is illustrated with two examples.

- 1) Granular precipitation initiated at a static grain boundary.

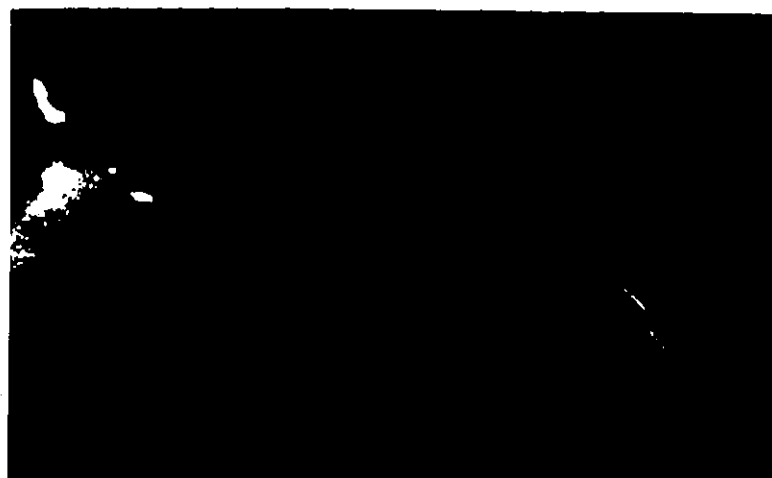
This is the case of low misorientation grain boundary,



a



b



c

Fig. 66 a) BF STEM image of dealloyed zone resulting from DIGM in Al-12 at.% Zn, 428K, 300 s.
b,c) CDF images showing the migration of the boundary.

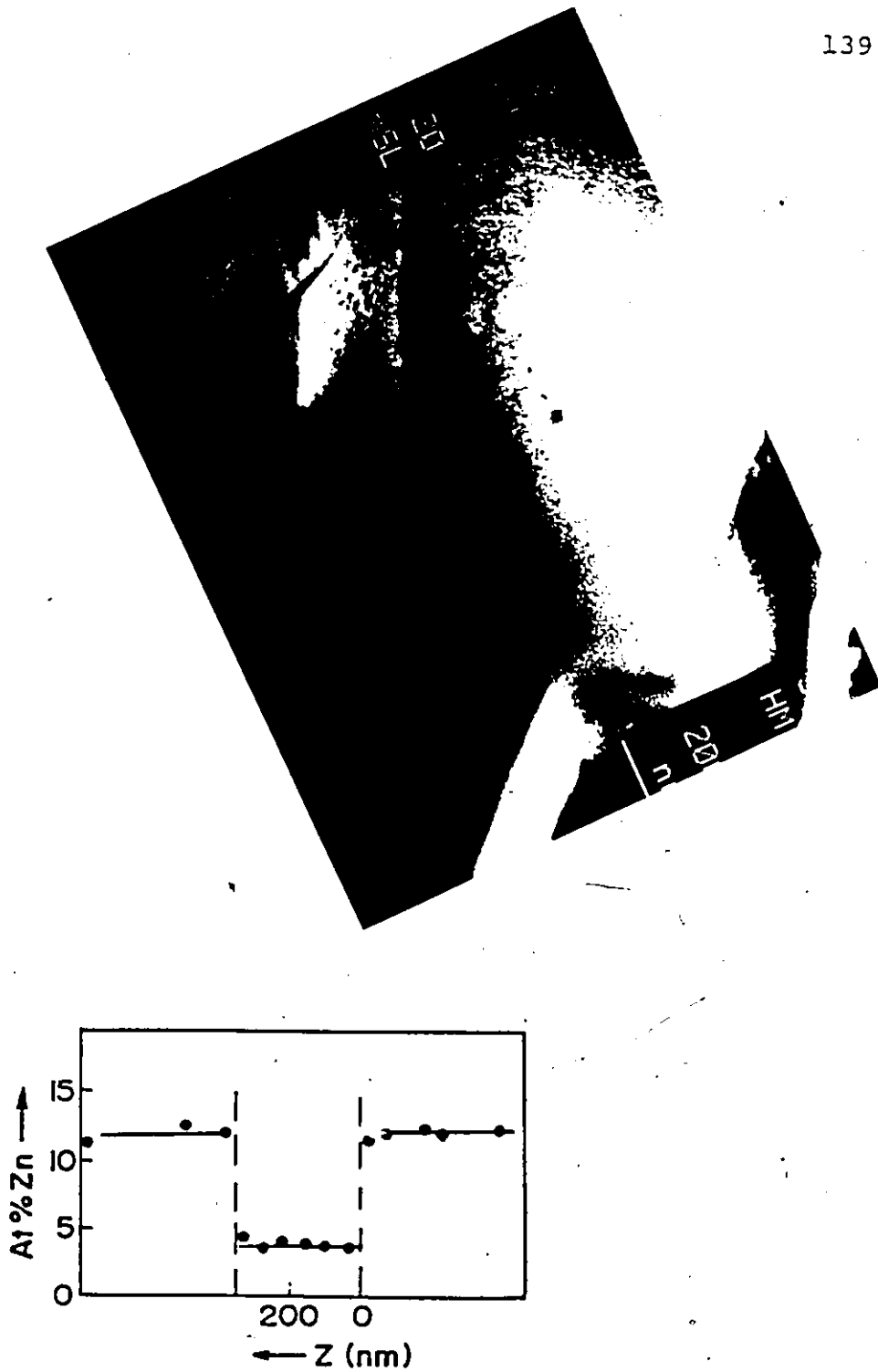


Fig. 67. Compositional STEM scan across alloyed zone. Note that Zn concentration in this case is closer to the equilibrium value, 0.035, than in the example in fig. 65.

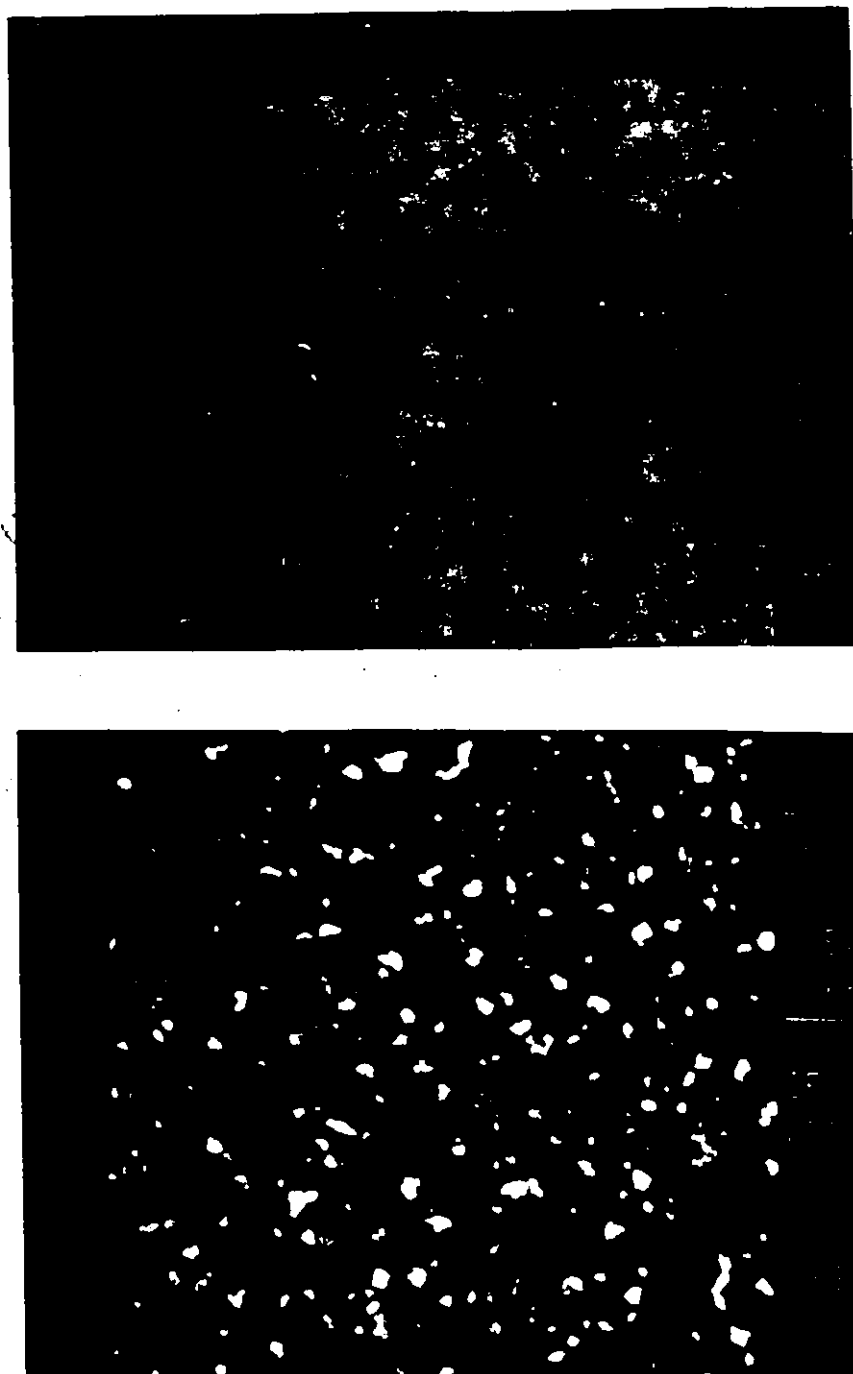


Fig. 68. Spinodal microstructure in Al-22 at.% Zn annealed 428K, 300 s and maintained at room temperature for 5 h.
a) bright field, b) centered dark field images.

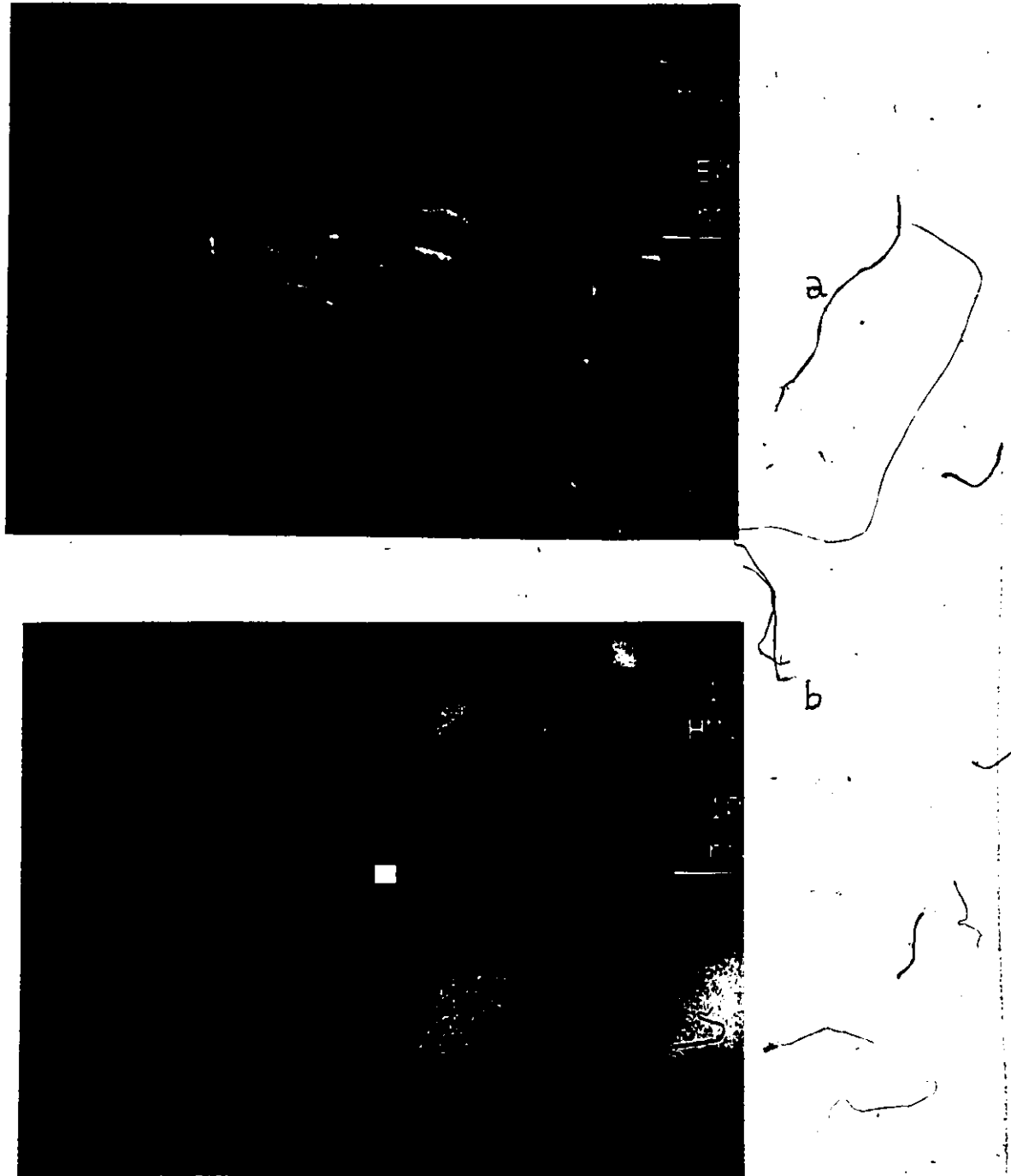


Fig. 69 a) Coarsened spinodal microstructure in Al-22 at.% Zn after 478K, 300 s. ADF image.
b) Area of microanalysis. $\cdot 10^6 \times$. B.F. image.

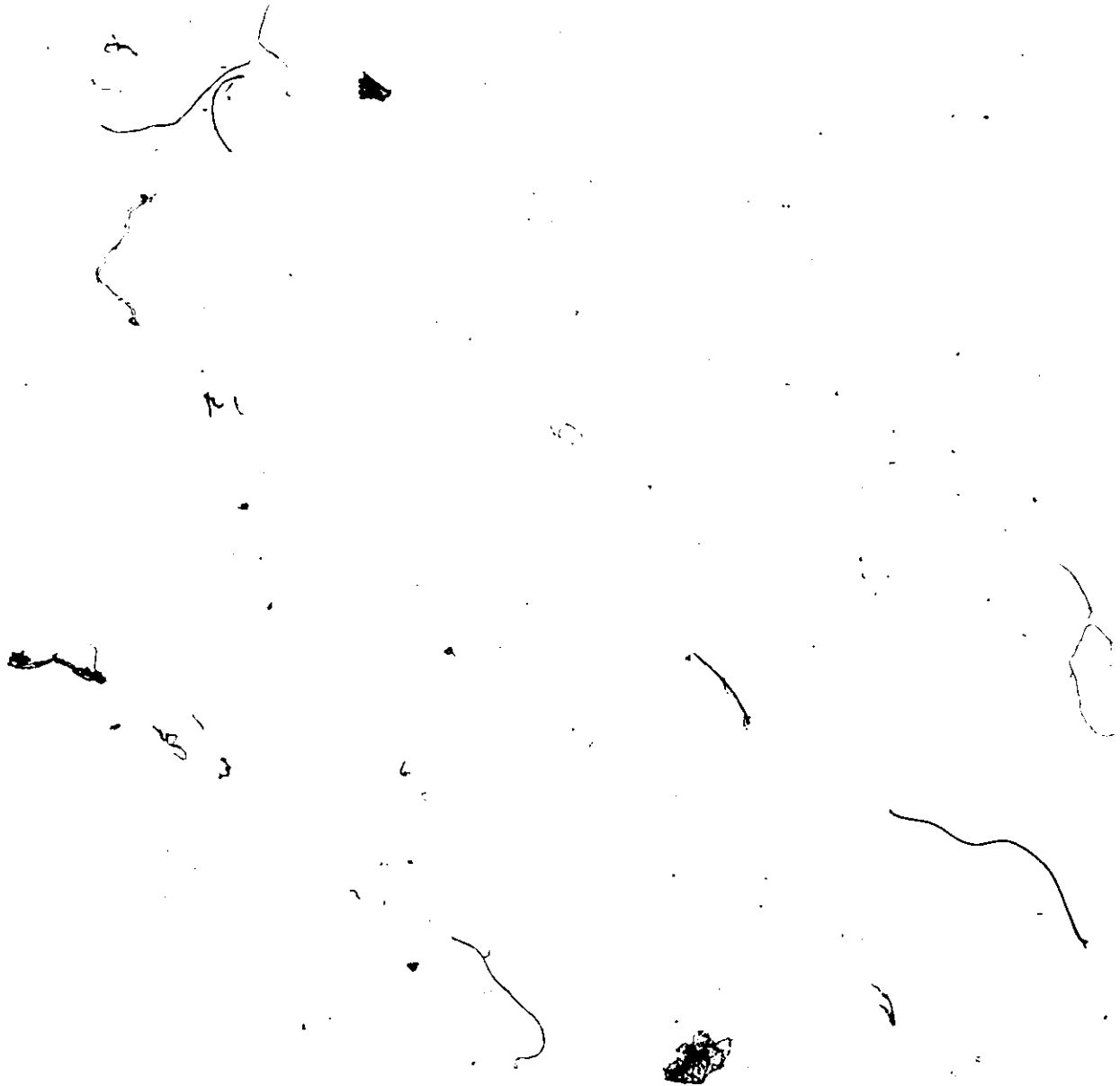
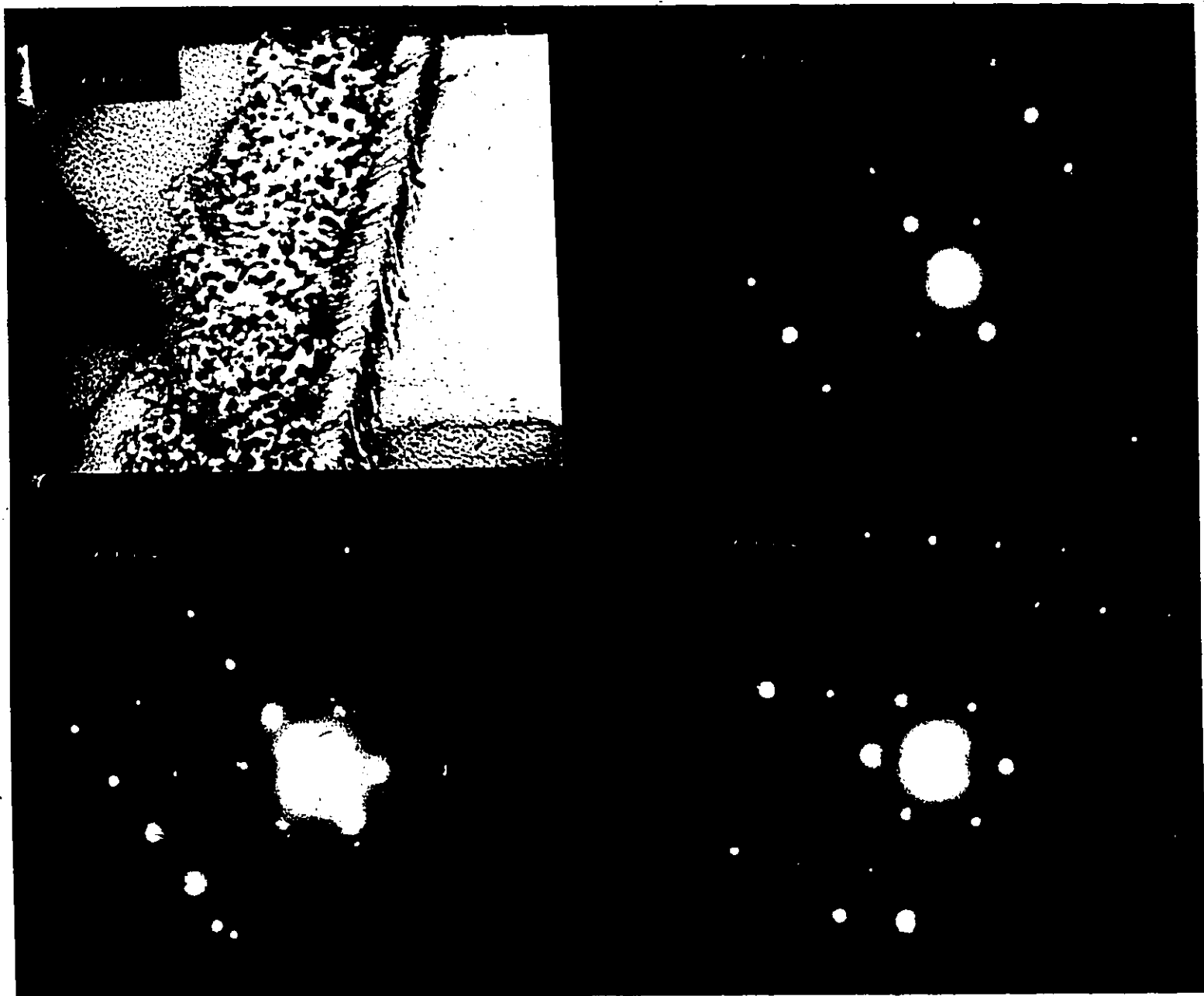


Fig. 70 a) Granular precipitation at a static grain boundary Al-22 at.% Zn. RT, 100 h.



Bright field

SADP from left grain

Diffraction pattern from both
grains together

SADP from right grain

Fig. 70 b) SADP sequence showing the low misorientation of the grain boundary.



Fig. 71 Granular precipitation posterior to discontinuous precipitation when the last has lost mobility.
Al-22 at.% Zn. 423K, 300 s, RT, 125 h.

which, although unable to migrate at room temperature still provides an active solute diffusion path. In a supersaturated matrix precipitation initiated at the grain boundary and then proceeds by the cooperative growth of the two phases without the migration of the grain boundary. Such appears to be the case for the example shown in fig. 70.

- ii) Granular precipitation at a grain boundary that has stopped migrating

Some as-annealed and quenched discontinuous precipitation cell boundaries appear to lose their mobility at room temperature. Granular precipitation, however, may replace the discontinuous mode in the same manner as in the preceding case. This event is illustrated in fig. 71.

4.4 Dissolution of the Discontinuous Product

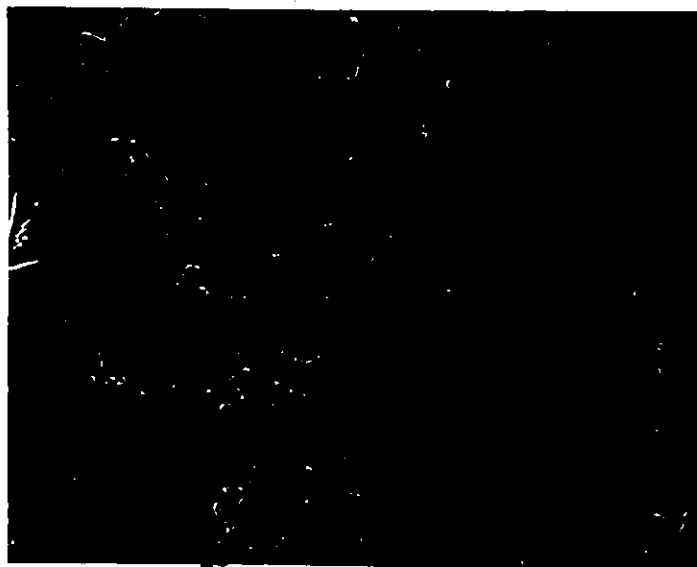
The purpose of this study was to see if the dissolution process is discontinuous, i.e. the grain boundary retreating and thereby dissolving the precipitated phase (as shown by Sulonen and by Tu and Turnbull). The present work has not found evidence for discontinuous dissolution. After annealing both alloys, 28 and 22 at.% Zn, at temperatures slightly above their solvus no measurable extent of grain boundary migration was detected; the process of dissolution takes place rapidly by volume diffusion control. Figure 72 shows typical low magnification SEM micrographs of both alloys, in which the static character of the grain boundary can be inferred. These

micrographs are to be compared with those shown in fig. 28.

Detailed CEM and STEM examination of the resulting microstructure in the alloy 22% Zn have shown that a dynamic recovery process takes place after only a few seconds of dissolution treatment. Some salient micrographs of this process are shown here. An explanation of the observed features, in conjunction with the discussion of the discontinuous precipitation process, will be attempted in the next chapter. It is noted that the grain boundary has not migrated 'backwards' even considering the favourable capillarity component, figs. 73 and 74. Closely spaced hexagonal arrays of screw dislocation can be observed at original α'/β interface, figs. 74-76. Eventually edge dislocation walls perpendicular to the screw dislocation walls can occur in the α' , figs. 77, 78. The dynamics of the recovery process (accompanying the dissolution) can rapidly organize the dislocations into subcells, figs. 79, 80. One may then speculate that after longer dislocation treatment a finer-grained defect-free homogeneous structure is to be expected.



b



a

Fig. 72 Low magnification SEM of microstructures resulting from ageing followed by dissolution treatment.
a) Al-28 at.% Zn, 472K, 300 s + 615K, 10 s.
b) Al-22 at.% Zn, 428K, 300 s + 595K, 10 s.

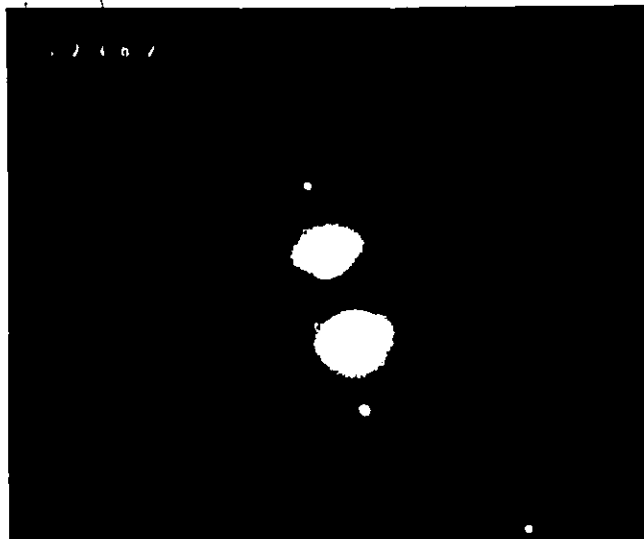


Fig. 73 a) Illustrating that neither the favourable curvature of the grain boundary nor the dislocation content in the product cell has insentivated at this stage, the migration of the boundary. Bright field TEM micrograph, 10K x. The SADP is from the product cell.



Fig. 73 b) A bright field (top) centered dark field (bottom) detail of the former reaction front.



Fig. 74 Bright field TEM image of the microstructure resulting from ageing and dissolution treatment: 478K, 300 s; 595K, 10 s. Despite the pronounced curvature of the grain boundaries (particularly at left), no retreating migration of these can be inferred. At this stage a high density of dislocations has resulted, although ineffective to induce the boundary to migrate.



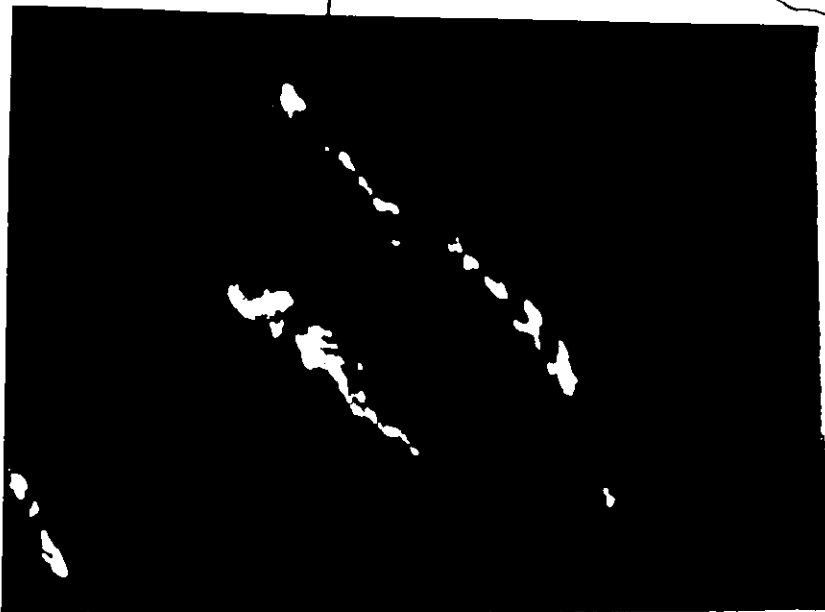
Fig. 75 a) STEM bright field micrograph of partially dissolved lamellar precipitates within two cells. 475K, 300 s; 593K, 10 s.



Fig. 75 b) Detailed view of the interfacial dislocation arrangement.

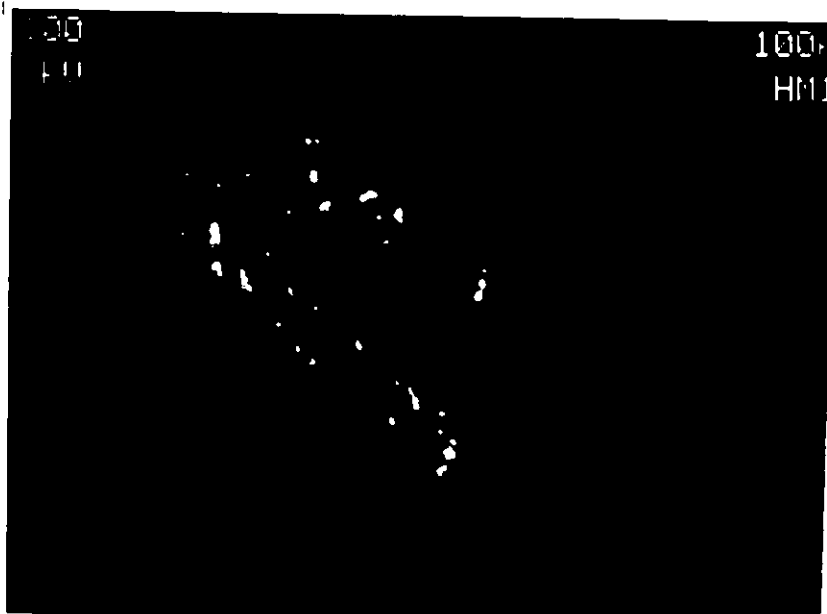


a



b

Fig. 76 Illustrating an isolated partially dissolved lamella in bright field a), in CDF with a ZN reflection, b) and in the weak beam dark field mode, c) in order to narrow the width and enhance the contrast of the strain fields.



c

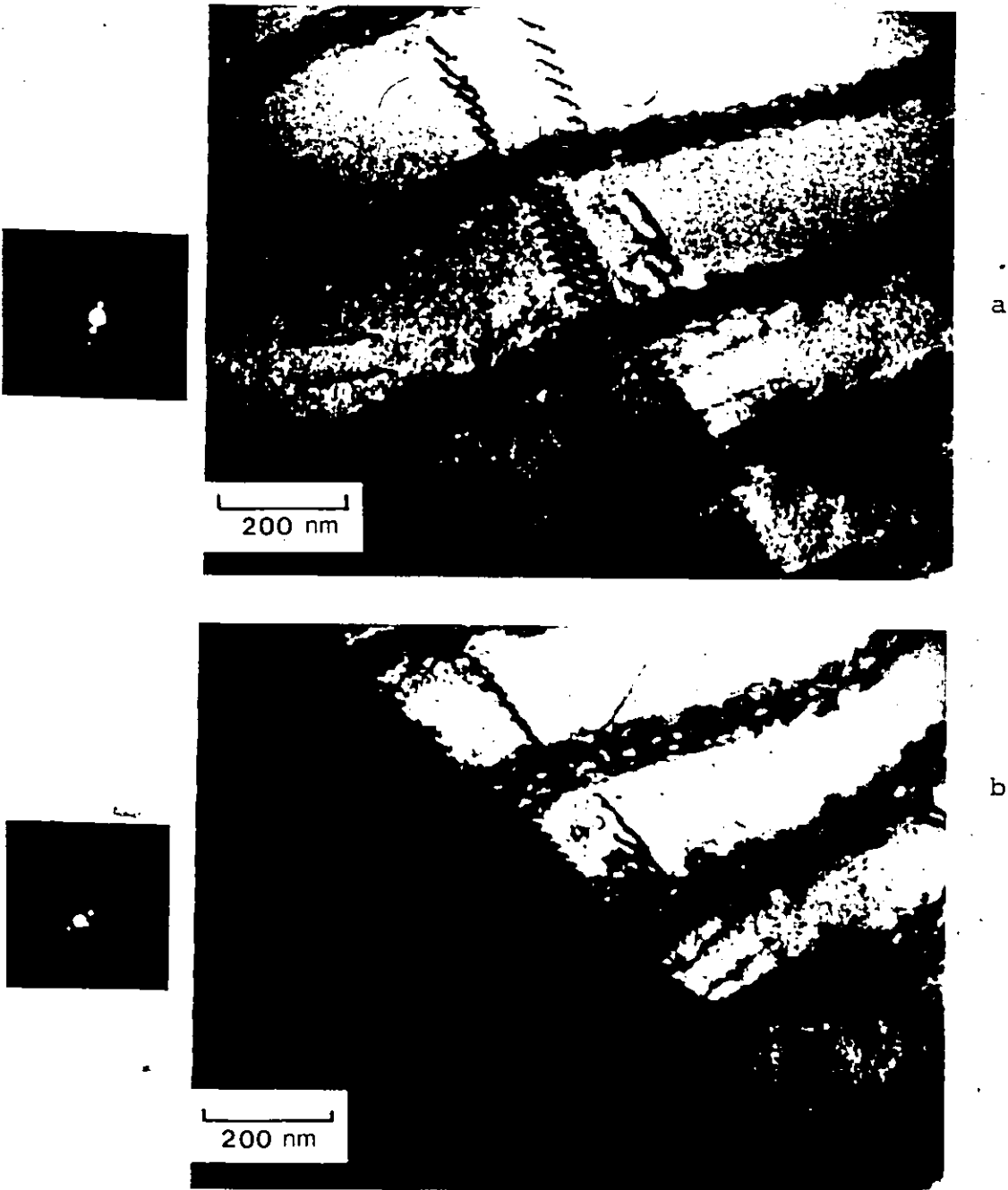
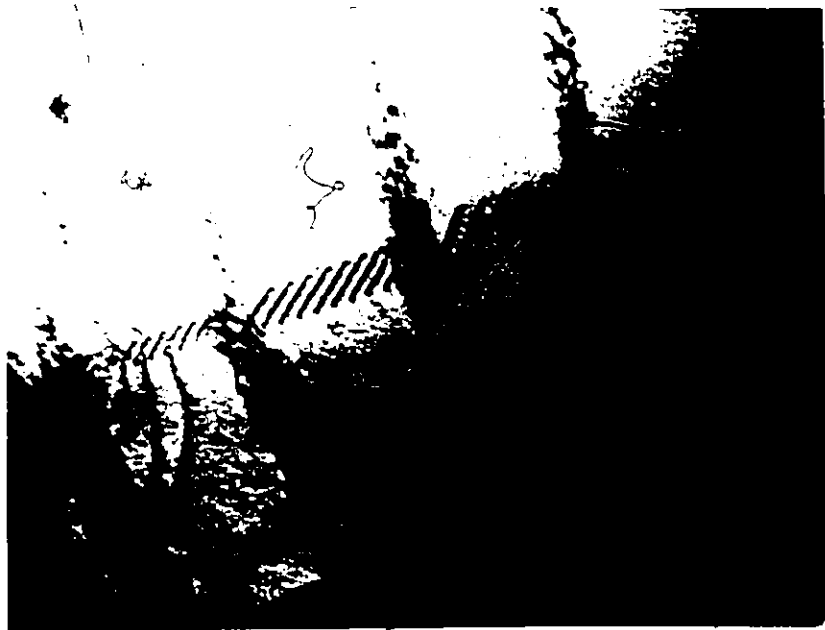


Fig. 77 Bright field STEM micrographs illustrating the fact that the recovery process eventually can produce a tilt boundary in the depleted lamella. This is shown as a wall of edge dislocation in a) the same area is shown under different diffraction conditions, in b).



a



b

Fig. 78 A second example of the edge dislocation wall perpendicular to the screw dislocation walls. a) in bright field, b) in dark field mode. 478 \times , 300 s, 595K, 10 s.

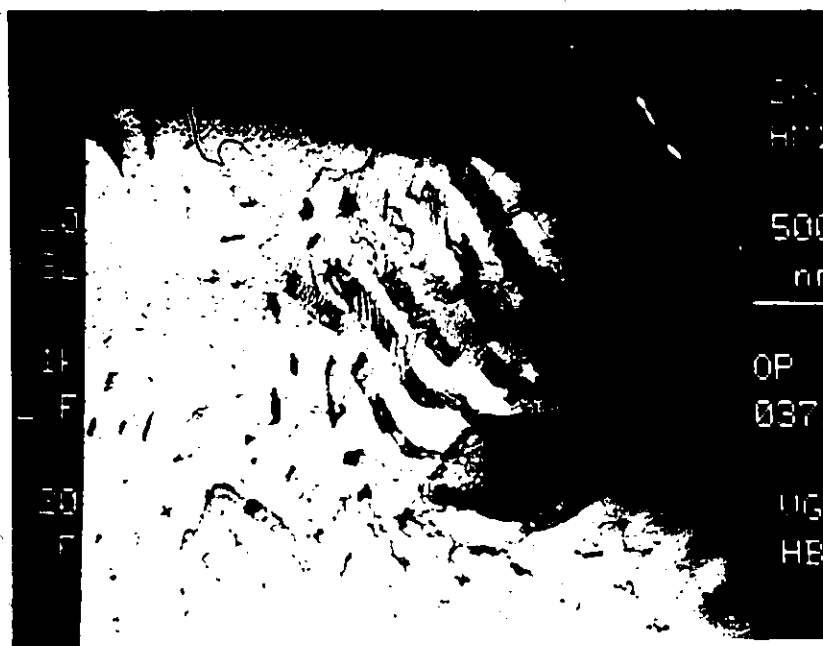


a



b

Fig. 79 { Illustrating that the generated dislocations organize themselves into subcells. a) Bright field, b) centered dark field. 478K, 300 s; 595K, 10 s.



a



b

Fig. 80 a) Bright field; b) centered dark field STEM micrographs showing the formation of subcells after 478K, 300 s, 590K, 11 s.



Fig. (80)c) Bright field micrograph of the same area under different diffraction conditions.

CHAPTER 5

DISCUSSION

In the description of the experimental results presented in the last chapter, a complete account of the discontinuous precipitation phenomena in this system was attempted. In the present chapter these results are examined under the light of the appropriate theoretical models, summarized in Chapter 2, whose relative merits will then be discussed. The major emphasis will be placed in the steady state growth process and related aspects. The interlamellar spacing problem is analyzed in some detail and a new set of calculations is presented in order to compare predicted vs. experimental results. Finally, since our experimental results and subsequent calculations are, to a great extent, based on analytical electron microscopy data, the reliability of these are discussed. Hence, for clarity, the discussion of the present work is divided into sections dealing with:

- i) The precursor of discontinuous precipitation.
- ii) The steady state lamellar growth process.
- iii) The post-dissolution microstructure.
- iv) The analytical results.
- v) Suggestions for further work.

5.1 The Precursor of Discontinuous Precipitation

Since the first recognition of DIGM, its similarities with the grain boundary migration during discontinuous precipitation, in particular at early states where the precipitating phase has not yet aligned itself, were acknowledged^{9,27}. It was suggested that both phenomena respond to a driving force of a similar nature⁹.

The present work has shown for the first time that a well-defined DIGM even can occur in systems undergoing discontinuous precipitation and, indeed, precede these. As pointed out in the last chapter, the high reaction velocity in Al-22 at.% Zn makes the detection of the precursor stage difficult. With this in mind, homogenized samples of Al-12 at.% Zn were treated for 300 sec at 428K. The boundaries were then found to possess configurations that must have developed through DIGM, e.g. the formation of precipitates on s-shaped boundaries, as shown in fig. 66. The fact that the boundary has migrated against its curvature is demonstrated by dark field imaging (fig. 66 b,c). The compositional STEM scan shows that the swept regions are depleted in Zn (fig. 67). The thermally induced migration and the pucker mechanism (precipitate induced) for initiation are clearly ruled out again in this case. It is very unlikely the coherence strain, in the sense proposed by Sulonen²¹ and developed by Hillert^{22,26}, could provide all the necessary.

driving force since the misfit parameter characteristic of Al-Zn is very small, $\eta = .009$. Hence it is difficult, in this case, to avoid the conclusion that the grain boundary has migrated in response, at least in large part, to a chemical driving force. Although the formulation of the chemical driving force is now the subject of some controversy²⁶, it is nevertheless of importance to recognize the existence of DIGM as a precursor of discontinuous precipitation and to regard it as independent of the previously postulated Fournelle-Clark and Tu-Turnbull mechanisms for reaction initiation. The natural question arising is why the effect is observed only with certain grain boundaries. This question awaits a better understanding of the effects of structure-sensitive grain boundary properties on discontinuous precipitation. No such study was attempted in the present work. However some suggestions are given at the end of this chapter.

5.2 The Steady State Growth

5.2.1 The resulting microstructure and thermokinetic results

An examination of the morphologies resulting from discontinuous precipitation in the aluminium-zinc alloy studied here lends no support to the criteria proposed by Bauman et al. It is not possible to characterize a single seam with high ageing temperatures ($T > T_m/2$) nor the double seam with the low ageing temperature ($T < T_m/2$). Furthermore, as discussed in the previous section, their proposed link with the conventional and pucker mechanisms, respectively, is non-existent in these alloys.

Regarding the microstructural characteristics of the steady state product, perhaps the more critical for the thermokinetic description are the interlamellar spacing and the α_0/α' interface curvature. The last is discussed here, in conjunction with the calculated parameters, and the next section is reserved for the former.

The series of examples of quenched interface shapes, given in chapter 4, support the general impression that the grain boundary tends to bow towards the parent grain for situations where the spacing is relatively stable. The discussion of the force balance acting at reaction fronts in such convex-forward configurations thus suggests that the chemical driving force plays a major role. Here reference is made to Hillert's¹⁰ and Perovic and Purdy's⁴⁶ analysis discussed in section 2.3.3 and illustrated in figures 9 and 10. In those

lamellae labelled as "characteristic of steady state growth", e.g. figures 60 and 62, the experimental composition profile compared with the parameter a (equation (5)) calculated through non-linear regression, gives indeed only a minor range of uncertainty (Tables IV and V). The inverse is true with lamellae assigned-('a priori' and based on interfacial shape) - a non-steady state designation. An example of this case was given in fig. 59; the local composition step across α_0/α' , given by the composition profile (albeit apparently exhibiting two maxima), seems not to balance the local capillary component at the interface.

The concentration of zinc in the α' phase at the α'/β boundary, $x_{\alpha'/\beta}$, given both by the measured X-ray microanalysis and by the non linear regression, indexed by x_3 in Tables IV and V, indicates that the equilibrium composition x_e has not been attained. This point was previously theoretically postulated by Hillert^{10,22} and the present work brings the first experimental proof for it. Porter and Edington⁴¹, in contrast, reported that in MgAl the composition of growing α' lamella at line in contact with the precipitating β particle was equal to the equilibrium value. Even considering the uncertainty in the x_3 values listed in tables IV and V, there is a gap with respect to the equilibrium values: from the Al-Zn phase diagram presented in reference 166 one can read at 428K, $x_e = 0.035$; at 478K, $x_e = 0.06$. This composition gap is even larger than the difference with the equilibrium solubility in α affected

by the curving edge of the β lamella, in accordance with the Gibbs-Thompson theorem. Assuming uniform hemicylindrical curvature at the tip of the β precipitate, the calculations yield: at 428K, $S_\beta = 25$ nm, $x_{\alpha/\beta} = 0.045$ at 478K, $S_\beta = 60$ nm, $x_{\alpha/\beta} = 0.066$.

The aim of the theories of discontinuous precipitation is to predict the various growth parameters at a given temperature. It is of interest to compare the behaviour of each cell boundary analyzed in terms of v , S_α and the measured concentration profile which are implicit in the values of a . By substituting these terms into equation (5) it is possible to obtain values for the grain boundary diffusion group $KD_b\delta$. This was done for each region analyzed and the values are listed in tables IV and V. the discussion is now focussed on the analysis at different segments contained in the same colony. When this is regularly formed, e.g. figures 35, 55, the local value of v is the same and the difference in S_α is small; the local $KD_b\delta$ value corresponding to each lamellae takes approximately the same value. The same kind of behaviour was also observed in colonies where local S_α and v are significantly different. In such a case the degree of solute partitioning, reflected in the composition profile, enters to moderate the variation of the vS_α^2 product. A colony for which this characteristic might be inferred is illustrated in figure 58 with individual lamellae Nos. 2, 3 and 4 (table V), figures 60 and 61. On the other hand, if the $KD_b\delta$

values obtained at the different cell reaction fronts are compared, a larger scatter is noted. The same kind of observation was made by Porter and Edington. This variation can be caused by changes in K , D_b or δ , all of which could be sensitive to such variables as boundary structure. Also variations in K could arise from changes in the interaction energy between zinc and the grain boundary. Such structure effects will not only arise between boundaries with different misorientation, but also as the plane of the boundary changes along the reaction front. Indeed Hassner's¹⁹⁴ Zn tracer diffusion data in random grain boundaries in Al-Zn alloys reports values of activation energy, Q , ranging from 22 to 30 K J mol⁻¹ and values of $D_b \delta$ from 2×10^{12} to 7×10^{10} nm³ s⁻¹ for the composition range from 2 to 37 at.% Zn. The values of $K D_b \delta$ reported here correspond to the lower values measured by Hassner¹⁹⁴.

The convergent beam microdiffraction technique was used with two objectives in view. The first, to check the sensitivity of this in detecting composition changes in the same crystal, i.e. the same lamella. Such sensitivity is linked to that of high order Laue zone (HOLZ) patterns to changes in lattice parameter¹⁹¹. The virtual constancy of the CBMD patterns along a compositional scan in α' serves rather to confirm the low atomic misfit in this system. The second, was to explore its response to changes in crystal symmetry. In this regard the technique was very useful in detecting the misorientation

between neighbour α' lamellae through the shift of the HOLZ lines. The parallel beam microdiffraction is a lower resolution technique (if compared with the convergent beam mode in the STEM) but able to resolve individual lamellae. It gives spot and Kikuchi line patterns and thereby allows a more accurate indication than its equivalent CBMD pattern which gives (sometimes diffuse) disc and HOLZ lines. This was the reason for including both in some figures.

5.2.2 The interlamellar spacing problem

The ability of discontinuous precipitation systems to change their spacing in response to change in temperature has been theoretically demonstrated^{34,40} and experimentally observed. Since most researchers display their results as average values of v and S , the range of spacings within a given sample has not received adequate attention. The work of Gust and coworkers⁶⁰, however, shows that a range exists and that its distribution can be represented by a Gaussian.

While the minimum spacing S_c is readily calculated as the thermodynamic limit of the available chemical free energy in the creation of interfacial free energy, as originally noted by Zener and expressed in equation (10), the maximum spacing is not thermodynamically determined. In principle any $S > S_c$ is possible but in accordance with the steady state velocity.

Here Sundquist's analysis⁴⁵, discussed in section 2.3.3, is of interest. He considers the development of recess at the α_0/α' interface as a regulatory mechanism to maintain the steady state spacing. The perception arising from the present work is that this limiting state, at the stability margin, is not the proper choice for the spacing realized in practice, but instead represents an upper limit on a range of possible spacings. Figure 59 illustrates this situation; it has the larger spacing in a well developed discontinuous precipitation colony, fig. 58. Other re-entrant interfaces have occasionally been seen but they are almost certainly transient as opposed to steady shapes.

The discussion of the optimal spacing requires the simultaneous consideration of two other properties of the reaction product: steady velocity v and residual supersaturation in α' , $(1-P)$. The more usual hypothesis for other lamellar products of eutectic and eutectoid transformations (that the velocity of the transformation front is optimized) is not so attractive for the case of discontinuous precipitation. This is because the incomplete solute partitioning, which is inherent in the grain boundary diffusion control reactions, plays a major role in the free energy balance. High velocities are therefore in principle possible, and would be accompanied by large spacing, and by minimal net free energy changes attending minimal solute redistribution.

As discussed in section 2.3.3, there are two theoretical approaches to the problem. Hillert's detailed treatment is potentially very attractive. However, it confronts two difficulties: one theoretical, as the model relies on the formulation of the local chemical force whose validity is now under question, as noted before; the other is related to the requirement to know the interface shape in detail, a condition difficult to meet in practice. The second approach is that the optimum state is one of maximum dissipation. While Cahn's analysis is in terms of maximum dissipation of free energy, Puls and Kirkaldy⁵⁷ favour the maximum entropy production. Since the system is isothermal, both approaches are equivalent.

The thermokinetic optimum, maximum rate of dissipation, is readily applied to experiment via the global theory of discontinuous precipitation. The global nature of this approach is evident when we consider that it is possible to evaluate the free energy change of parent and product phases, at points sufficiently remote from the transformation interface, and so evaluate the free energy consumed in accomplishing the transformation, without inquiring into details of the actual transformation process. The only requirement is that the front remain approximately planar. For the purpose of searching for an optimum the global approach is particularly useful. Indeed, in the application of a thermokinetic optimal principle, it is advantageous to ask as little as possible about the details of the process, but to enquire into initial and final states only.

For the experimental test, we require thermodynamic data for the alloy system under study, grain boundary diffusion data, and an estimate of the residual supersaturation in α' . All these requirements are now available for the Al-Zn system. The last two have been met, simultaneously and for the specific grain boundary under scrutiny (thus removing an element of uncertainty associated with variation of $KD_b\delta$ within a given polycrystalline specimen), through high resolution microanalysis in individual lamellae, as described previously. Before proceeding it is worthwhile to note a difficulty in applying the optimal hypothesis in this system as related to the (fast) competing spinodal reaction in the parent α_0 which must reduce the available free energy in α_0 . Against these, however, are the remarkably constant steady-state spacings and velocities attained by the discontinuous front, suggesting strongly that the system is transforming under constant driving force. A schematic representation of the free energy sinks is given in figure 81, where ΔG_1 is the free energy difference with the alloy under hypothetical dilute solution behaviour, ΔG_2 is the free energy consumed by the spinodal reaction, ΔG is the actual free energy released by the discontinuous precipitation reaction and ΔG_r is the free energy retained with the residual supersaturation in α' .

The systematics of the calculations is as follows. The actual composition profile represented by its parameter a , in conjunction with thermodynamic data for the α solid solution, is used to evaluate the actual free energy released $P\Delta G_{\text{chem}}$.

Now, thanks to the spinoidal reactions, the assignment of dilute solution behaviour to the parent α is reasonable. Recalling here that the analytical form of P is then given by

$$P(a) = \frac{3}{\sqrt{a}} \tanh \frac{\sqrt{a}}{2} - \frac{1}{2} \operatorname{sech}^2 \frac{\sqrt{a}}{2}$$

with

$$a = vs^2/kD_b\delta$$

and for ΔG_{chem} by

$$\Delta G_{\text{chem}} = RT \frac{(x_o - x_e)^2}{2x_o}$$

The test then requires spacing, velocity, and microanalytical data from the same lamella. The local value of $kD_b\delta$ is then used to calculate the net free energy change as a function of v and S using

$$\Delta G_{\text{net}} = P\Delta G_{\text{chem}} - \frac{2\gamma_{\alpha'\beta}V_m}{s}$$

The value of $\gamma_{\alpha'\beta}$ was taken from reference 66. Some sample results for the experimental conditions used here are shown next. Starting with the computed plots of $P\Delta G_{\text{chem}}$ vs v , fig. 82, and $P\Delta G_{\text{chem}}$ vs S , fig. 83, these merely confirm internal consistency. The increase of either both v or S reduces the utilization of the chemical driving force. The plots ΔG_{net} vs. v , fig. 84, and ΔG_{net} vs. S , fig. 85, show that as $S \rightarrow S_c$, the net free energy change $\rightarrow 0$. The reduction in ΔG_{net} with increased velocity of fixed spacing $> S_c$ is simply a result of diminishing

time for solute diffusion in the grain boundary. There is no well defined optimum in these curves.

When dissipation, indexed as $\Delta G_{\text{net}} \cdot v$ is examined as a function of S and v for these same data, we find the well-formed optimum of figure 86. Thus one can see immediately that a maximum in dissipation exists, that is a single value, and that it represents a possible unique state with which to compare experiments. These results, and their comparison with experimental velocity and spacing data are summarized in Table VI. Included in the same table VI are the results of the same sort of calculations given for the alloy Mg-9 at.% Al studied by Porter and Edington. Although they did not concern themselves with quantification of free energy stored in α' nor about the variation in S , their information of v , s and a allows the calculation of the optimum conditions through the dissipation function. The level of agreement seems to be good, particularly with the Mg-Al alloy, where the absence of general precipitation in the parent grain and the dilute solution behaviour certainly contribute. In the Al-Zn alloy it is possible that the value of the chemical driving force was overestimated since rather high solubility limits in the parent α were assumed. A decrease of, say, 5 J on the value of ΔG_{chem} significantly improves the agreement experimental value vs calculated optimum.

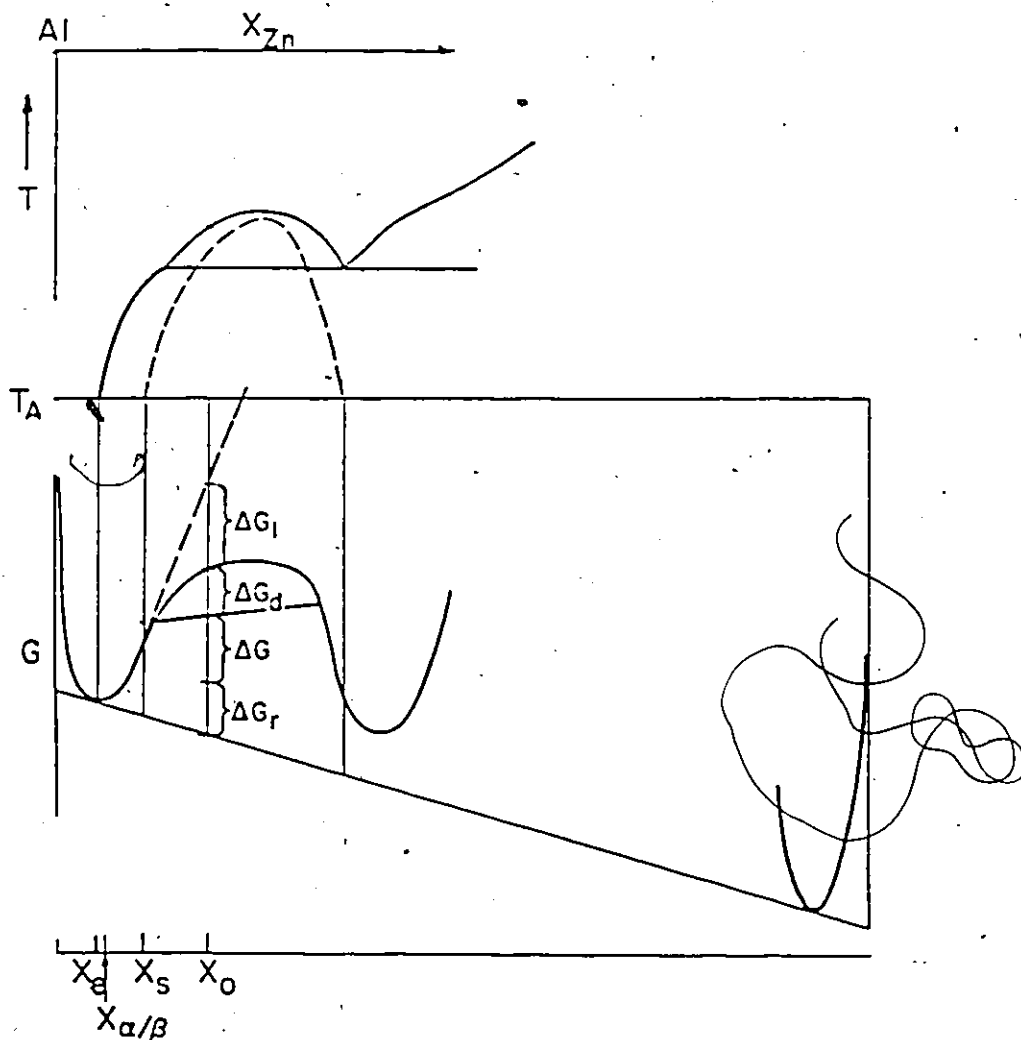


Fig. 81 Schematic free energy-composition diagram demonstrating that the driving force for discontinuous precipitation is reduced by spinoidal decomposition in the parent grain at the ageing temperature T_A .

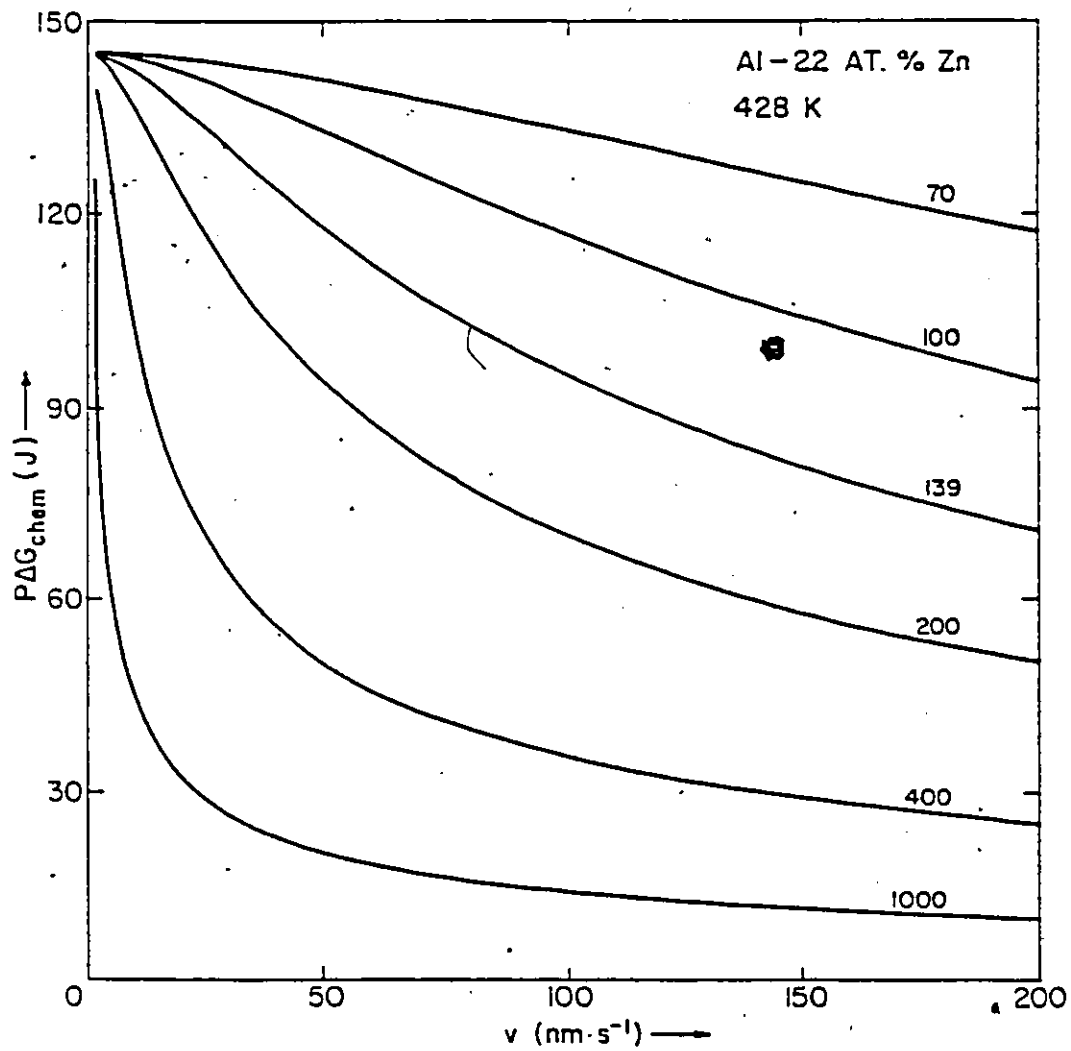


Fig. 82. Computed plots of ΔG_{chem} vs. v . The numbers on the curves are values of S in nm Al-22 at.% Zn a) at 428K

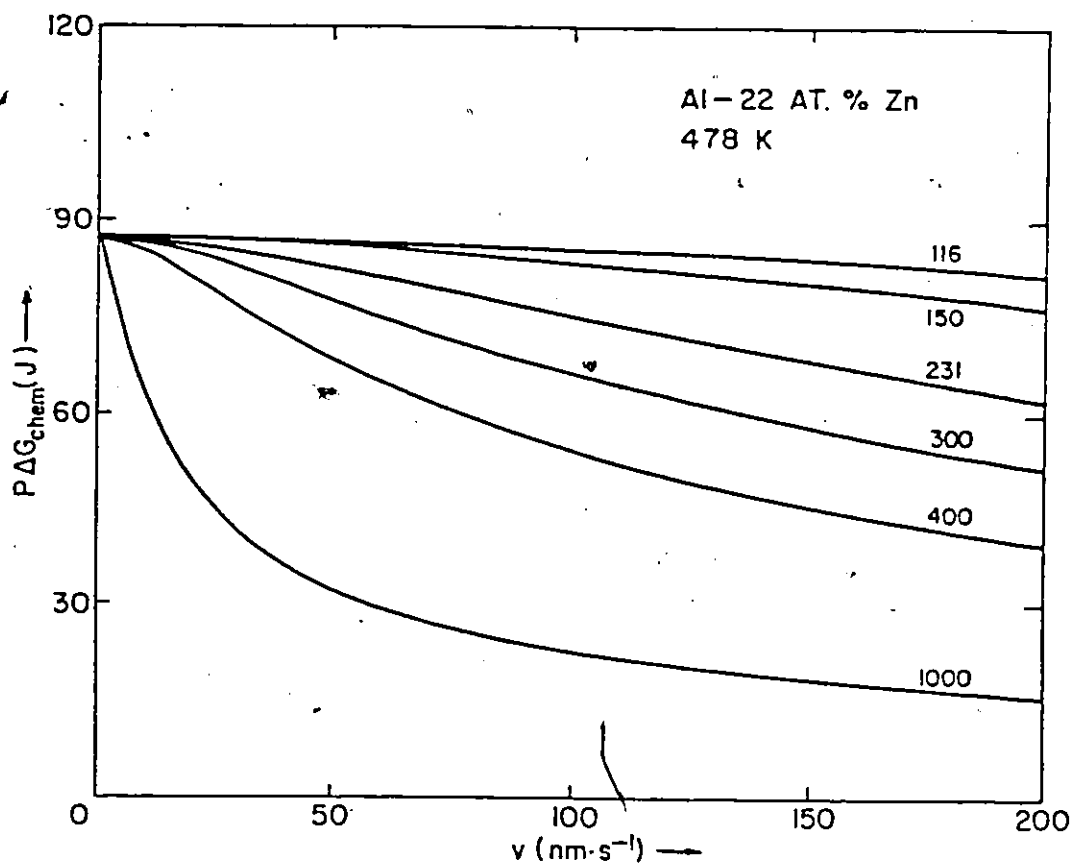


Fig. 82 b) 478K.

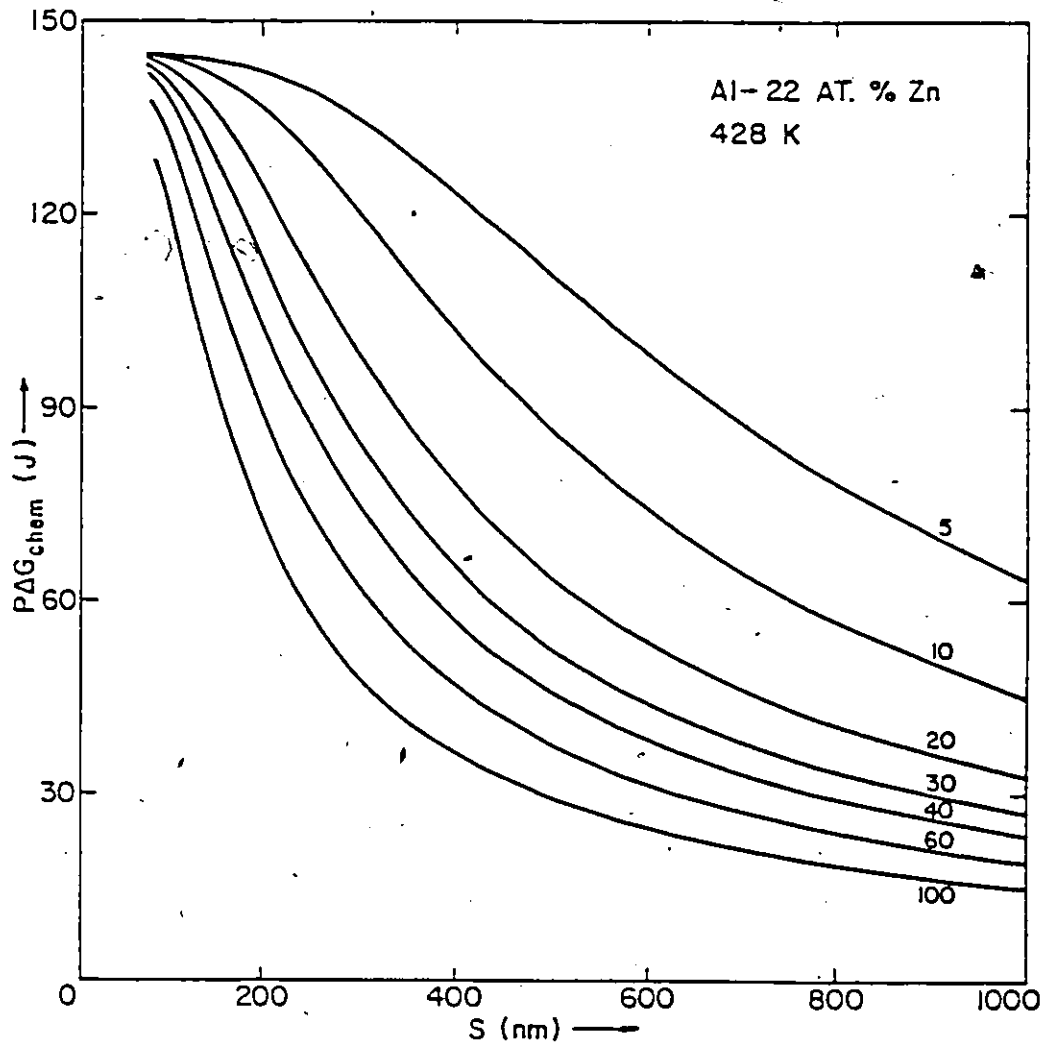


Fig. 83 Computed plots of $P\Delta G_{chem}$ vs. S_1 number on curves are values of ν in nms^{-1}
a) 428K.

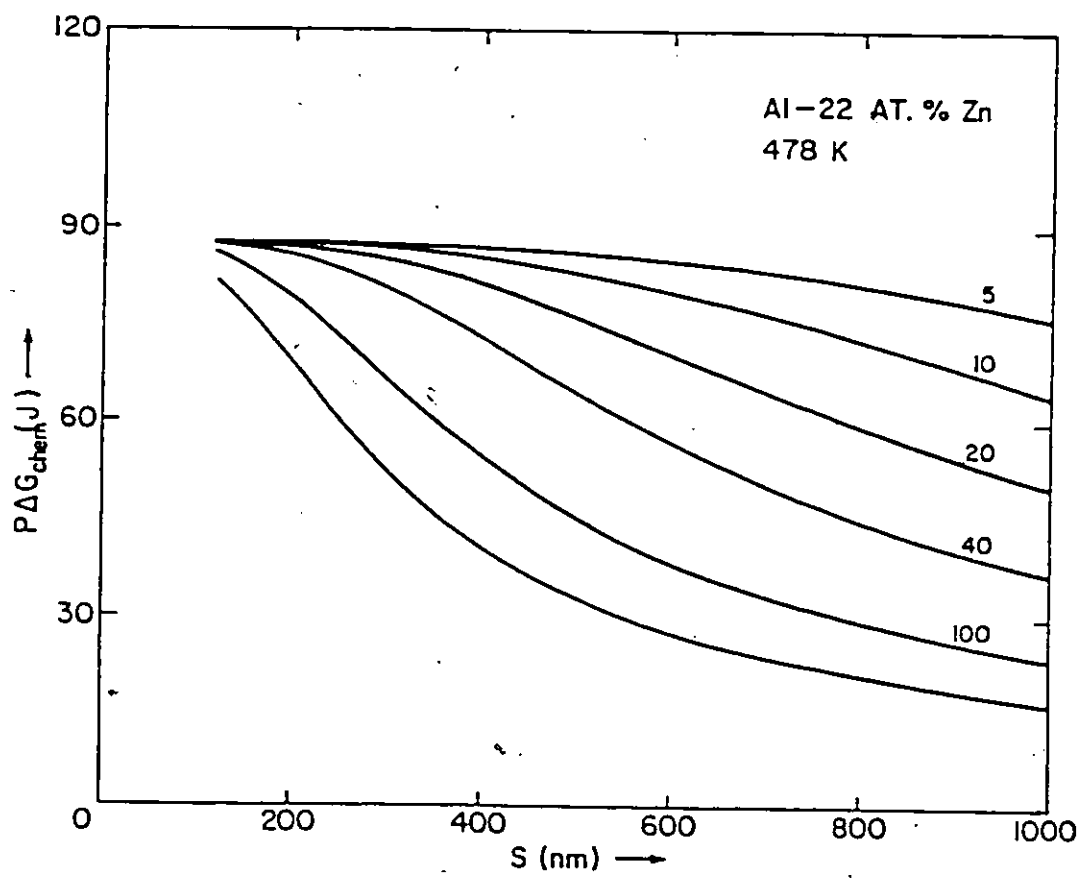


Fig. 83' b) 478K

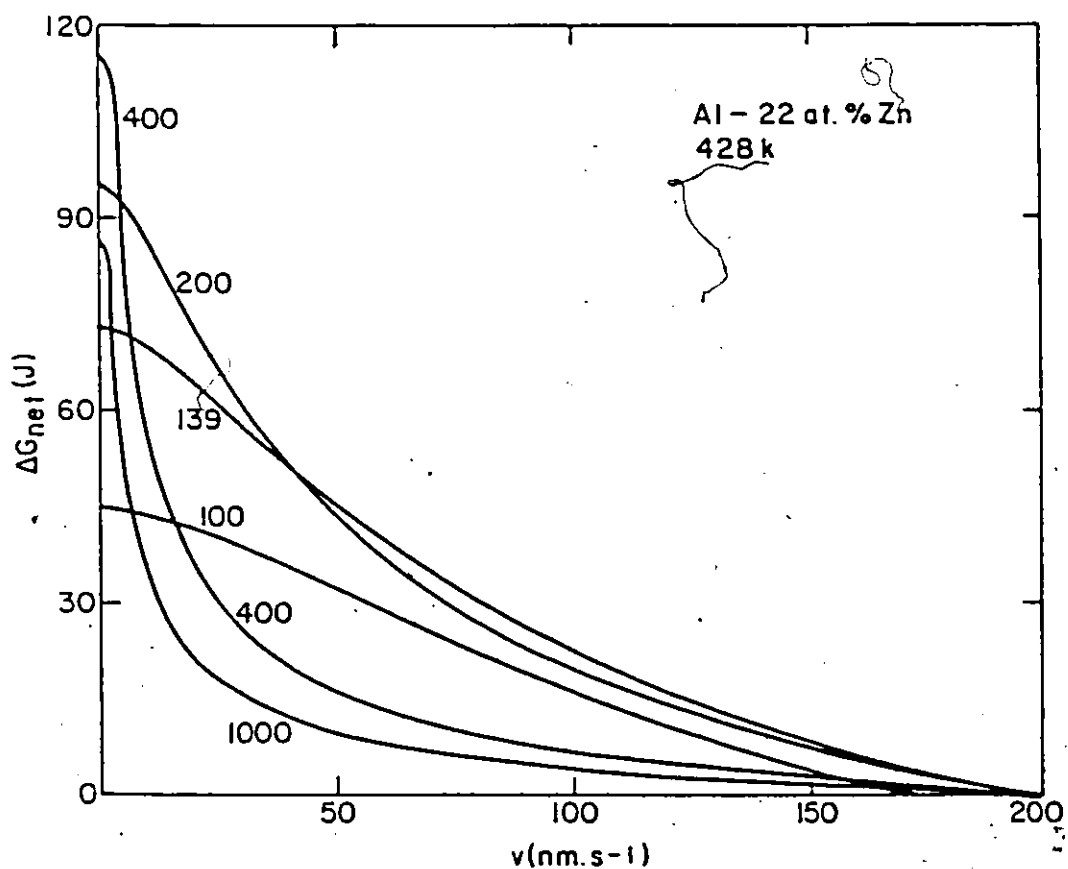


Fig. 84. Computed plots of the net free-energy released, ΔG_{net} , as a function of cell velocity. Number of the curves are values of S in nm. a) 428K.

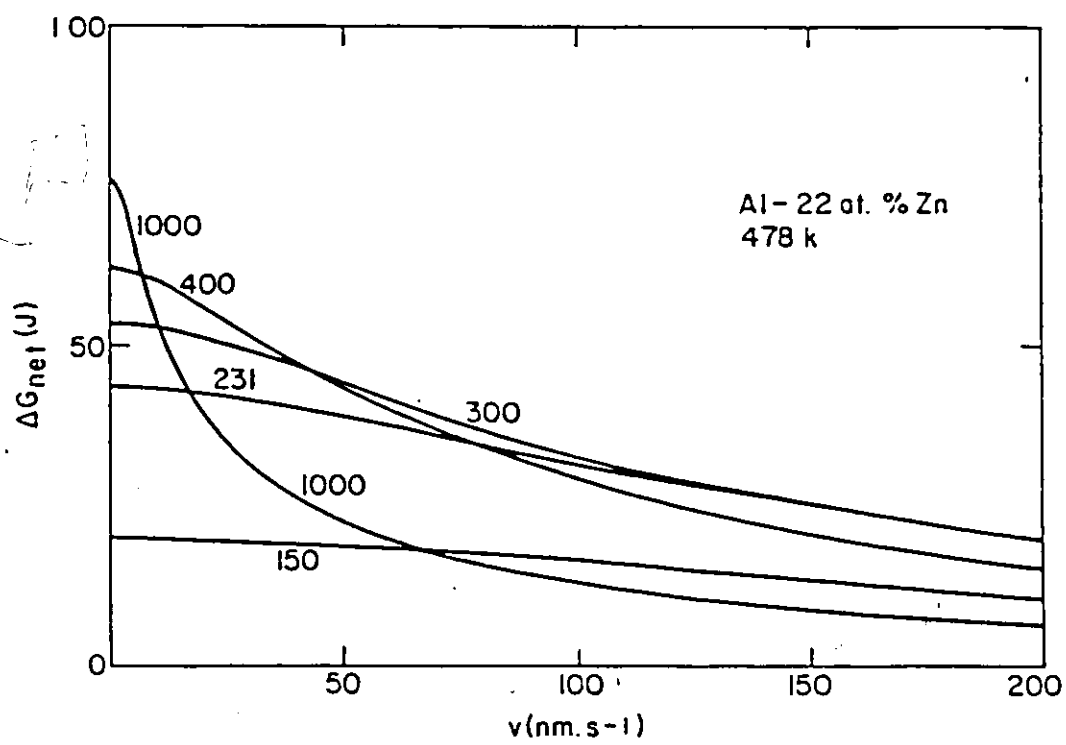


Fig. 84 b) at 478K

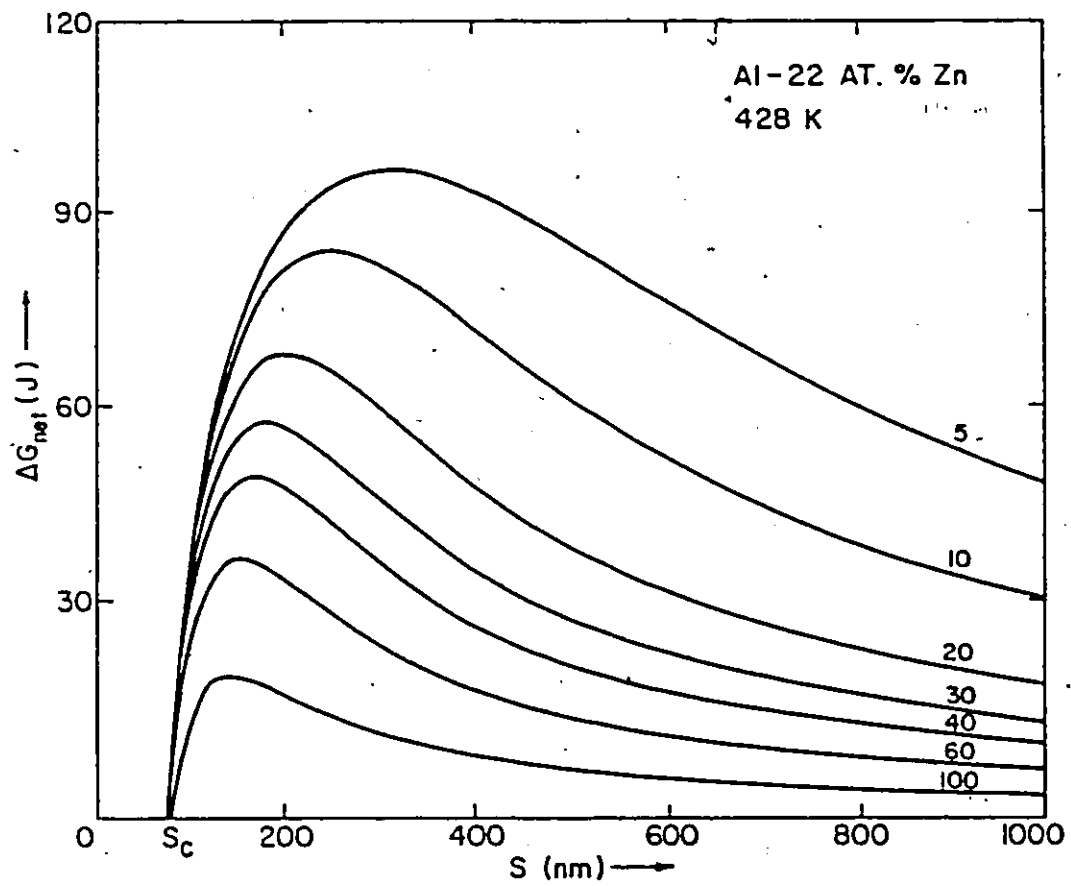


Fig. 85 Computed plots of ΔG_{net} as a function of lamellar spacing. Number of curves are values of cell velocity in $\text{nm} \cdot \text{s}^{-1}$.
a) at 428K

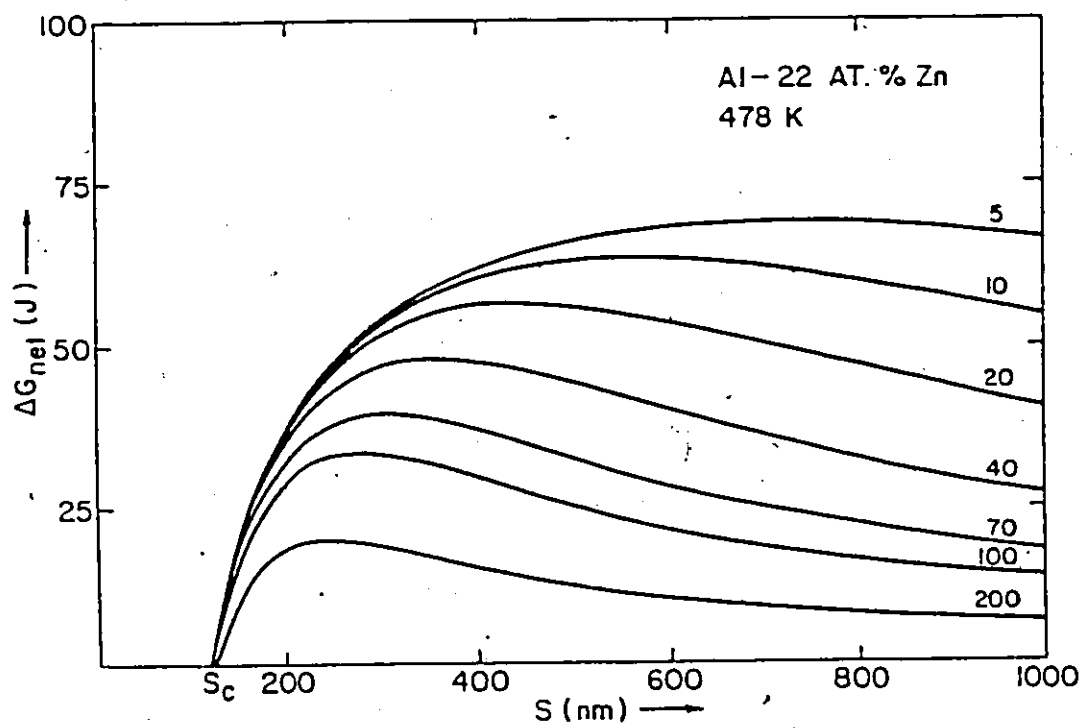


Fig. 85 b) at 478K

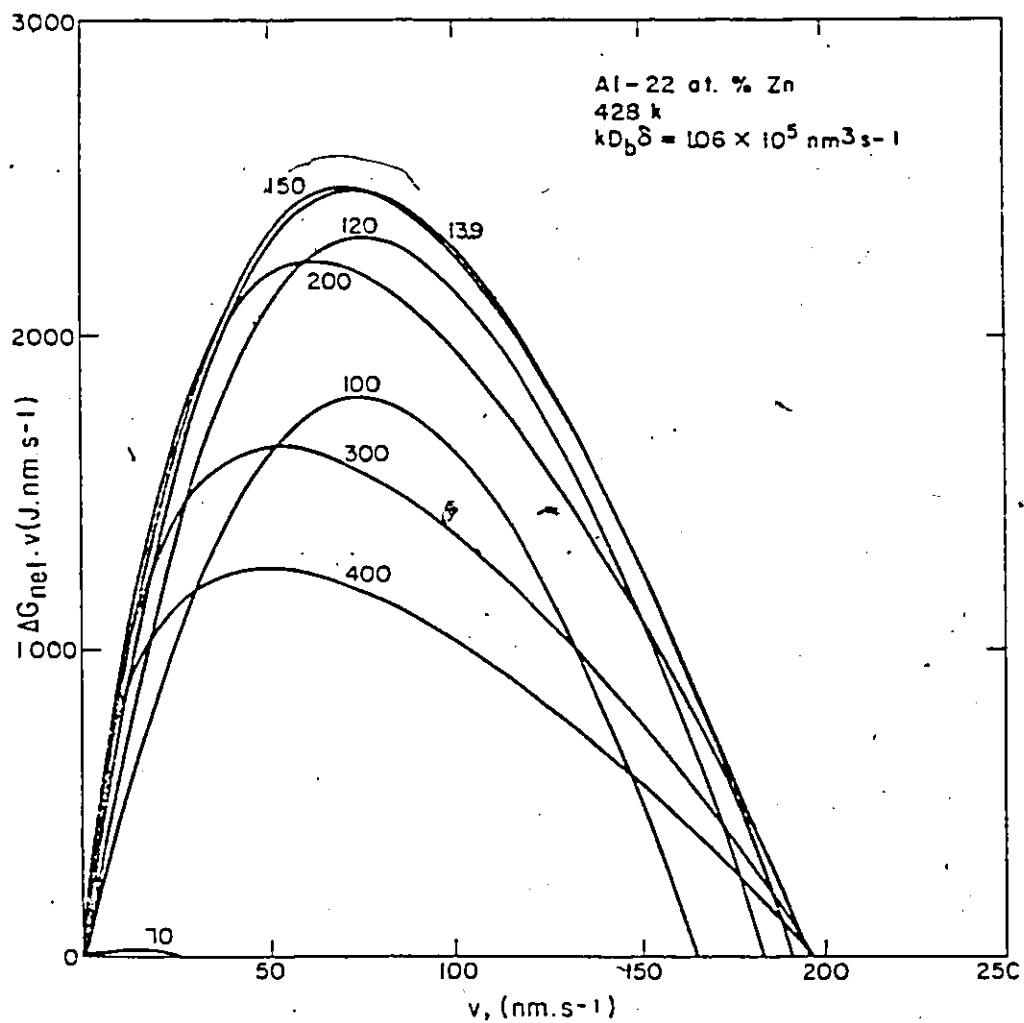


Fig. 86 Computed variation of the dissipation function, $\Delta G_{\text{net}} \cdot v$, with the cell velocity. Number of curves are values of S in nm. Al-22 at. % Zn
a) at 428K

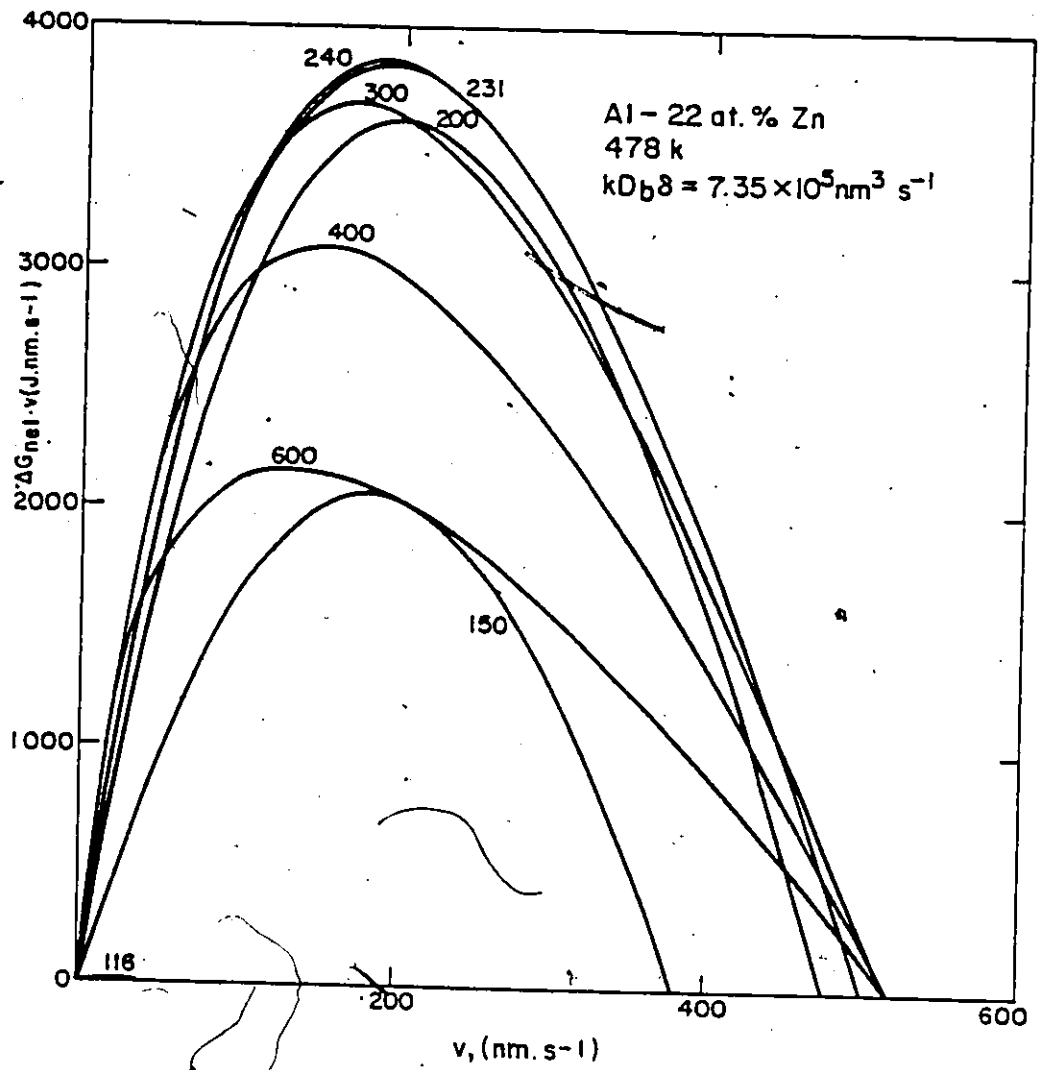


Fig. 86 b) 478K

Table VI. Comparison of measured with optimal values of cell velocity and interlamellar spacing

Parameters	Al-22 at.% Zn		Mg-9 at.% Al	
T(K)	428	478	485	550
ΔG_{chem} (J)	145.1	87.0	83.4	42.7
$KD_b \delta$ ($\text{nm}^3 \text{s}^{-1}$)	1.06×10^5	7.35×10^5	3.6×10^5	6.5×10^6
γ (J nm^{-2})	5.1×10^{-19}	5.1×10^{-19}	4×10^{-19}	4×10^{-19}
S_c (nm)	69.5	115.5	130	255
S_{op} (nm)	140	235	265	515
$S_{\alpha \text{ meas.}}$ (nm)	175	280	288	420
$v_{\text{meas.}}$ (nm s^{-1})	27	41.6	27	59
v_{op} (nm s^{-1})	70	188	20	330

5.3 The Post Dissolution Microstructure

This section will be brief, since it was not considered in the initial objectives of the present work. However, the consistency of the dislocation patterns responding to thermal treatment along with the information, also consistent, obtained from the discontinuous precipitation product, i.e. before dissolution, allow us to attempt an interpretation of the micrographs. The first element of analysis is the observed, measurable, misorientation between neighbouring α' lamellae. The second element is, the observed hexagonal dislocations network at a certain stage of the annealing process. This observation is (with difficulty) reproducible. It seems that during the steady state growth the β precipitating lamellae adopts a cusp orientation with α' while the grain boundary reaction front, in search of its own thermodynamic equilibrium orientation, exerts local torque components at the reaction front. The resulting strain is elastically stored in the discontinuous product. The α' lamella appears as subjected to a twist distortion. Reheating the lamella structure above the solvus temperature - which is comparatively high for the alloy - the stored energy is released and screw dislocations are readily formed at the original α'/β interfaces in array as a twist boundary. A secondary effect of the twist could be, as noted in figs. 75, 76, edge dislocation walls dividing slightly misoriented segments of the same lamella. This

misorientation can be observed by the contrast difference across the wall (fig. 76) and measured by CBMD or PBMD patterns in the STEM.

The above discussion refers to highly transient microstructures, which are, however, amenable to mathematical modeling. It has been shown that pure dilational misfit η can be accommodated by 3 sets of screw dislocations¹⁵⁴. It appears that in this case there is a rotation component ϕ in the deformation tensor and arises from the twist distortion, so that

$$(D_+^{-1} - I) = \begin{bmatrix} \eta & \phi & 0 \\ -\phi & \eta & 0 \\ 0 & 0 & \eta \end{bmatrix}$$

where D_+ is the deformation matrix in the (+) crystal, D^{-1} denotes the inverse of D and I is the identity matrix.

5.4 The Analytical Results

The concentration profiles measured with the STEM are quantitatively in good agreement with those calculated through nonlinear regression. Therefore the a and P values are considered reliable. The value of x_3 is more sensitive to the accuracy of the analytical conditions. It is clear that the major sources of uncertainty are related to the determination of the K_{ZnAl} factor and absorption occurring preferentially in aluminium. The last has been minimized by the analysis in thin portions of the crystal. However, some workers, in-

investigating in higher absorbing systems such as Ni-Al¹⁹² alloys assign error bars to be $\pm 10\%$ analyzing foils typically 500 nm thick. The K_{ZnAl} factor obtained with the "standards" prepared here has the value of 1.25 ± 0.08 . The range of values obtained for the different alloys is: for 40 w% Zn: 1.20 to 1.34; for 25 w% Zn: 1.10 to 1.41; for 20 w% Zn: 1.17 to 1.27; for 5 w% Zn: 1.10 to 1.29. For comparison, the following reported values are: Goldstein¹⁷² gives $K_{ZnAl} = 1.18$, from the relation K_{ZnSi}/K_{AlSi} ; Chapness et al¹⁹³, published data which reads $K_{ZnAl} = 1.38$ experimentally and $K_{ZnAl} = 1.43$ calculated. It is worth noting that the K factor is strongly sensitive to instrumental conditions. Errors are estimated for the present results as $\pm 10\%$.

5.5 Suggestions for Further Work

- a) In order to better characterize the influence of grain boundary structure on discontinuous precipitation, the study of the reaction on well-characterized bicrystals of Al-Zn will be of value. However, technical difficulties, associated with the preparation of both the bicrystal itself and the foil for electron microscopy, are to be expected.
- b) With similar purpose, the reaction front structural characteristics in polycrystalline samples could be specified by the axis/angle pair technique in the TEM.

These procedures will contribute to obtain meaningful activation energy values, i.e. from Arrhenius plots for grain boundaries characterized by the same set of structural parameters.

- c) With the Al-22 at.% Zn alloy, up quenching experiments of discontinuous products could be devised with two objectives in mind; the first that enables one to assess if coherency loss takes place in the absence of dissolution (i.e. at $T < T_{\text{eutectic}}$), and the second to determine the mode of precipitate dissolution at temperatures below the solvus (i.e. at $T > T_{\text{eutectic}}$).
- d) The study of discontinuous precipitation and dissolution in an Al-15 at.% Zn will be advantageous in two respects. The precipitation process will take place at lower rate than with the Al-22 Zn alloy, enabling a more detailed study of DIGM event. On the other hand, since in this alloy $T_s = 546\text{K}$ (i.e. slightly lower than T_{eutectic}), it is possible that dissolution proceeds discontinuously.
- e) Concentrated Zn alloys in this system must undergo eutectic decomposition rather than discontinuous precipitation. A study of the transition between the two modes would be of considerable interest.
- f) It may be worthwhile to promote grain refinement through precipitation/dissolution thermal cycling experiments, and to test the mechanical properties response.

CHAPTER 6

CONCLUSIONS

The CTEM and microanalytical STEM studies reported in this thesis indicate the following important features of the discontinuous precipitation reaction in Al-22 at.% Zn alloy.


- 1) Diffusion induced grain boundary migration occurs both as a precursor for and simultaneously with discontinuous precipitation. As a reaction precursor, DIGM is to be regarded as independent of the previously postulated Fourelle-Clark mechanism.
2. The morphologies resulting from discontinuous precipitation, at all the conditions studied here, exhibit migration both on one side and both sides of the grain boundary. Hence, no clear characterization of either of these morphologies with ageing temperature (regardless whether higher or lower than $T_m/2$) is possible. A granular form of boundary precipitation has also been observed. This is apparently cooperative in nature and distinct from discontinuous precipitation in the sense that no boundary migration is involved.
3. The steady state growth reaction front has been studied in detail. The main characteristics are:

- a) Quenched α_0/α' interface shapes exhibit convex-forward configurations thus suggesting that the chemical driving force plays a major role in the migration of the boundary.
- b) There is a well-defined Zn concentration profile along the depleted lamellae parallel (and close) to the cell interface.
- c) Grain boundary diffusivity was obtained from each analyzed lamellae. Lamellae in the same colony yield approximately the same value, although their interlamellar spacing may change. However, a comparison of data from different reaction fronts, in the same sample, indicates a variation of one order of magnitude in diffusivities. This effect has been tentatively explained as being due to the influence of grain boundary structure on discontinuous precipitation. The values of $kD_b\delta$ calculated here are in agreement with those measured by Hassner¹⁹⁴ for Zn trace diffusion along random grain boundaries in Al-Zn alloys.
- d) The concentration of Zn in α' at the α'/α interface both measured and calculated through non linear regression analysis is higher than the equilibrium composition. This finding is

- consistent in all the lamellae studied and appears to be in agreement with the predictions of Hillert's theory^{10,22}.
4. The interlamellar spacing has been discussed by reference to the principle that discontinuous precipitation systems search a maximum rate of dissipation as originally postulated by Cahn⁴⁰ and Kirkaldy⁵⁷. A free-energy dissipation function has been defined and allows calculations requiring local thermokinetic data (retained by supersaturation, grain boundary diffusivity), which can be obtained only through high resolution microanalysis. It seems that discontinuous precipitation systems do find and hold an optimal state and that they represent an optima in the rate of dissipation of free energy. Comparison with real systems is promising. In Al-Zn, where the chemical driving force has to account for the competing spinodal reaction, the agreement is not as good as with the Mg-9 at.% Al considered, where matrix precipitation is absent.
 5. The dissolution of the discontinuous precipitation product at temperatures slightly above the solvus has been found to proceed by volume diffusion control. The observed generation of dislocation arrays within the former cell which accompanies this dissolution has been interpreted as due to a recovery mechanism induced by elastic energy stored in the product phases during the growth

process. Microdiffraction and dark field imaging techniques have revealed twist distortions in the aged and quenched steady-state lamellar product.

REFERENCES

1. W. Gust, "Phase Transformations", Vol. 1, Ser. 3, No. 11, p 27, Institute of Metallurgist, London (1979)
 2. D.B. Williams and E.P. Butler, Int. Met. Rev. 3, 153 (1981).
 3. N. Agnew and G. Sachs, Z. Phys., 66, 293 (1930).
 4. W.C. Hagel and H.J. Beathe, Trans. AIME, 215, 967 (1959).
 5. R.P. Marshall, Acta Met., 9, 958 (1961).
 6. H. Böhm, Z. Metallk., 52, 564 (1961).
 7. A. Perovic, Ph.D. Thesis, McMaster University, 1980.
 8. G. Meyrick, Scripta Met., 10, 649 (1976).
 9. M. Hillert and G.R. Purdy, Acta Met., 26, 333 (1978).
 10. M. Hillert, "The Mechanisms of Phase Transformations in Crystalline Solids", p. 231, The Institute of Metals, London, 1969.
 11. K. Tu and D. Turnbull, Acta Met., 15, 369, 137 (1969).
 12. H.B. Aaron and H.I. Aaronson, Metall. Trans., 3, 2743 (1972).
 13. J.K. Lee and H.I. Aaronson, Acta Met., 23, 809 (1975).
 14. N. Lange and G.R. Purdy, Metall. Trans.,
 15. P.A. Fournelle and J.B. Clark, Metall. Trans., 3, 2757 (1972).
 16. S.F. Bauman, I. Mitchel and D.B. Williams, Acta Met., 29, 1343 (1981).
 17. D.B. Williams and J.W. Edington, Acta Met., 24, 323 (1976).
 18. M. Millert and R. Langneborg, J. Mater. Sci., 6, 208 (1971).
 19. A.H. Gaisler, "Phase Transformations in Solids", 432, Wiley, New York, 1951.
- 

20. S.C. Smith, Trans. ASM, 45, 533 (1953).
21. M.S. Sulonen, Acta Met., 12, 749 (1964).
22. M. Hillert, Metall. Trans., 3, 1729 (1972).
23. J.S. Kirkaldy, "Decomposition of Austenite by Diffusional Processes", eds. V.F. Sackay and H.I. Aaronson, p. 39, Interscience, New York, 1962.
24. J.M. Shapiro, Ph.D. Thesis, McMaster University, 1966.
25. J.M. Shapiro and J.S. Kirkaldy, Acta Met., 16, 1239 (1968).
26. M. Hillert, Scripta Met., 17, (1983)
27. J.W. Cahn, J.D. Pan and R.W. Balluffi, Scripta Met., 13 503 (1979).
28. R.W. Balluffi and J.W. Cahn, Acta Met., 29, 493 (1981).
29. P. Shewmon and Zong-Sen Yu, Met. Trans. 13A, 1567 (1982).
30. M. Hillert and Chogmo Li, Acta Met., 29, 1133 (1981).
31. T.J. Picone, D.B. Butrymowicz, D.E. Newbury, J.R. Manning and J.W. Cahn, Scripta Met., 16, 839 (1982).
32. C.A. Hondwerker, R.L. Clobe and J.E. Blendell, Ceramic Society Symposium, 3-5 May 1982, Cincinnati, Ohio.
33. K. Tashiro and G.R. Purdy, Scripta Met., In press.
34. C. Zener, Trans. AIME, 167, 550 (1946).
35. M. Frebel and B. Predel, Mat. Sci. Eng. 15, 221 (1974).
36. D. Turnbull, Acta Met., 3, 55 (1955).
37. E.P. Butler, V. Ramaswamy and P. Swan, Acta Met., 21, 517 (1973).

38. T.R. Anantharam, U. Ramaswamy and E.P. Butler, *J. Mater. Sci.*, 9, 240 (1974).
39. K. Smidoda, W. Loftschalk and H. Gleiter, *Acta Met.*, 16, 579 (1978).
40. J.W. Cahn, *Acta Met.*, 7, 8 (1959).
41. D. Porter and J.W. Edington, *Proc. Roy. Soc.*, A385, 335 (1977).
42. H.J. Aaronson and Y.C. Liu, *Scripta Met.*, 2, 1 (1967).
43. J. Peterman and E. Hornbogen, *Z. Metallk.*, 59, 814 (1968).
44. K. Lüke, *Z. Metallk.*, 52, 1 (1961).
45. B.E. Sundquist, *Metall. Trans.*, 4, 1919 (1973).
46. A. Perovic and G.R. Purdy, *Acta Met.*, 29, 53 (1981).
47. M. Hillert, *Acta Met.*, 30, 1689 (1982).
48. G.R. Speech, *Trans. AIME*, 227, 754 (1963).
49. R. Kossowsky, *Metall. Trans.*, 1, 1623 (1970).
50. J. Singh, S. Lele and S. Ranganathan, *Z. Metallk.*, 72, 469 (1981).
51. D. Turnbull and Treaffis, *Trans. AIME*, 212, 33 (1958).
52. H.I. Aaronson and J.B. Clark, *Acta Met.* 16, 845 (1968).
53. Y.C. Liu and H.I. Aaronson, *Acta Met.*, 16, 1343 (1968).
54. G.R. Speech, *Trans. AIME*, 242, 1359 (1968).
55. M. Frebel and B. Predel, *Z. Metallk.*, 64, 913 (1973).
56. M. Frebel, K. Bohler and B. Predel, *Z. Metallk.*, 67, 228 (1976).
57. M.P. Puls and J.S. Kirkaldy, *Metall. Trans.*, 3, 2777 (1972).

58. E. Hornbogen, Metall. Trans., 3, 2717 (1972).
59. M.V. Thompson, Ph.D. Thesis, University of Cambridge, 1972.
60. W. Gust, B. Predel and V. Roll, Z. Metallk., 68, 117 (1977).
61. E. Nes and H. Billdal, Acta Met., 25, 1039 (1977).
62. M.H. Ainsley, G.J. Cocks and D.R. Miller, MET. Sci., 13, 20 (1979).
63. M. Frebel and J. Schenk, Z. Metallk., 70, 230 (1979).
64. R.A. Fournell, Acta Met., 27, 1135 (1979).
65. E.P. Butler, Rep. Prog. Phys., 42, 833 (1979).
66. M. Vijayalakshmi, V. Seetharam and V.S. Raghuratham, Acta Met., 30, 1156 (1982).
67. R.C. Ecob, J.V. Bee and B. Ralph, "Phase Transformations", 2, II-22, Institution of Metallurgists (1979).
68. "Grain Boundary Structure and Kinetics", American Society for Metals, 1979.
69. J.C. Fisher, J. Appl. Phys., 22, 74 (1951).
70. P.H. Pumphrey, "Grain boundary structure and properties", p. 136, G.A. Chadwick and D.A. Smith, eds., Academic Press (1976).
71. H. Gleiter and B. Chalmers, Prog. Mater. Sci., 16 (1972).
72. N.L. Peterson, in ref. 68, p. 209.
73. J. Herbeuval, M. Biscond, and A. Goux, Mem. Sci. Rev. Met. 70, 39 (1973).
74. R.W. Balluffi, in ref. 68, p. 297.
75. R.W. Balluffi, Metall. Trans., 13, 2069 (1982).

76. G.R. Purdy, in "Proceedings of an International Conference in Solid-Solid Phase Transformations", The Metallurgical Society of AIME, 1982.
77. W. Gust, B.M. Hints, Lodding, Odelens and B. Predel, Acta Met., 29, (1981).
78. J. le Coze, C. Rauson and G. Goux, Comptes Rend. Hebd. Seance Acad. Sci., C 271, 1120 (1970).
79. J. le Coze and G. Goux, ibid., C 271, 1225 (1970).
80. P.N. Uinwing and R.B. Nicholson, Acta Met., 17, 1379 (1969).
81. E.P. Butler and P. Swan, Acta Met., 24, 343 (1976).
82. R. Gronski and P. Furrer, Metall. Trans., 12A, 121 (1981).
83. J. Briano-Valero and R. Gronski, ref. 76, p. 439.
84. J.M. Penison and R. Gronski, ref. 70, p. 679.
85. C.S. Smith, Trans. ASM, 45, 533 (1953).
86. K.N. Melton and J.W. Edington, Acta Met., 22, 1457 (1974).
87. G. Hassen and G. Goux, Scripta Met., 5, 889 (1971).
88. D.A. Smith, C.M.F. Rae and C.R.M. Grovenor, ref. 68, p. 337.
89. W. Gust, N. Predel and K. Dieskstatt, Z. Mettalk. 68, 619 (1977); 69, 75 (1978); 69, 444 (1978).
90. W. Gust, B. Predel and V. Roff, Acta Met. 28, 1395 (1980).
91. W. Gust, M.B. Hintz, B. Predel and V. Roll; quoted in ref. 1.
92. R. Wirth and H. Gleiter, Acta Met., 29, 1830 (1981).
93. R. Dudler and H. Gleiter, Z. Mettalk., 73, 677 (1982).
94. H.B. Aaron and G.R. Kotler, Metall. Trans., 2A, 393 (1971).
95. M. Sulonem, Acta Met. 8, 669 (1960).

96. L.N. Larikov and Y.F. Yunchenko, Phys. Met. Metalloved, 20, 4, 628 (1965).
97. G.N. Bogaceva, V.D. Sadovsky and V.M. Shastlivtsev, *ibid*, 23, 2, 283 (1967).
98. K. Tu and D. Turnbull, Metall. Trans. 2A, 2509 (1971).
99. K. Tu, Metall. Trans. 3A, 2769 (1972).
100. S.P. Gupta, Mat. Sci. Eng., 21, 211 (1975).
101. M. Frebel and J. Shenk, Z. Metallk., 70, 55 (1979).
102. K. Russew and W. Gust, Z. Metallk., 70, 522 (1979).
103. K. Akamatsu, W. Gust, M.B. Hints and B. Prebel, ref. 76, p. 933.
104. A. Pawlowki and W. Truszkowski, Acta Met., 30, 37 (1982).
105. V. Melhorthra and K.B. Rundman, Metall. Trans., 3A, 1551 (1972).
106. D. Chethan and F.R. Sale, Acta Met., 22, 333 (1974).
107. P.G. Boswell and G.A. Chadwick, Acta Met., 25, 779 (1977).
108. L.E. Murr, "Interfacial Phenomena in Metals and Alloys" Addison-Wesley Publishing Company Inc., 1975.
109. A. Kelly and R.B. Nicholson, Progress in Materials Science, Vol. X, No. 3, Pergamon, Oxford, 1963.
110. "Phase transformations", American Society for Metals, 1970.
111. "Precipitation Processes in Solids", K.C. Russel and H.I. Aaronson, editors, The Metallurgical Society of AIME, 1978.
112. G.R. Purdy, Metallography, 7, 131 (1975).

113. M. Hillert, Metall. Trans., 6A, 5 (1975).
114. J.W. Martin and R.D. Doherty, "Stability of Microstructure in Metallic Systems", Cambridge University Press, 1976.
115. R.D. Doherty, Metal Sci., 16, 1 (1982).
116. J.W. Cahn, Trans. Met. Soc. AIME, 242, 167 (1968).
117. H.I. Aaronson and J.K. Lee in "Lectures on the Theory of Phase Transformations", The Metallurgical Society of AIME, 1975.
118. G.P. Speich and P.A. Oriani, Trans. Met. Soc. AIME, 233, 623 (1965).
119. D.E. Stephens and G.R. Purdy, Acta Met., 23, 1343 (1975).
120. G.W. Lorimer and R.B. Nicholson, Ref. 10, p. 36.
121. M.H. Jacobs and D.W. Pashley, *ibid.*, p. 43.
122. D.W. Hoffman and J.W. Cahn, Surf. Sci., 31, 368 (1972).
123. J.W. Cahn and D.W. Hoffman, Acta Met., 22, 1205 (1974).
124. R.C. Ecob, Met. Trans., 11A, 1407 (1980).
125. R.C. Ecob and B. Ralph, Ref. 76, p. 915.
126. W. Bollman, "Crystal Defects and Crystalline Interfaces", Springer-Verlag, Berlin (1970).
127. P.C. Ecob and B. Ralph, Acta Met. 29, 1039 (1981).
128. C.M. Sargent, G.R. Purdy and G. Weatherly, Scripta Met., 14, 725 (1980).
129. G. Weatherly (in press).

130. R. Gronsky, Report on the panel discussion on experimental techniques, Ref. 76, p. 1577.
131. F.C. Frank and J.H. van der Merwe, Proc. R. Soc., A198, 205 (1949).
132. J.H. van der Merwe in "Treatise in Materials Science and Technology", Vol. 2, p. 1, Academic Press, N.Y., 1973.
133. W. Bollman, J. Microsc., 102, 233 (1974).
134. J.H. van der Merwe, *ibid.*, 102, 261 (1944).
135. L.M. Brown and G.R. Solhouse, Phil. Mag., 19, 329 (1970).
136. H.I. Aaronson, J. Microsc., 102, 275 (1974).
137. C. Laird and R. Sankaran, *ibid.*, 116, 123 (1979).
138. J.W. Matthews, in "Dislocation in Solids", ed. by F.R.N. Navarro, North Holland, 1979.
139. M.G. Hall, H.I. Aaronson and K.R. Kinsman, Surf. Sci., 31, 257 (1972).
140. G.C. Weatherly, P. Humple and D. Borland, Acta Met., 27, 1818 (1979).
141. J.W. Christian and K.M. Knowles, Ref. 76, p. 1185.
142. J.W. Christian, Metall. Trans., 13A, 509 (1982).
143. G.R. Purdy, Acta Met., 26, 477 (1978).
144. G.C. Weatherly and R.B. Nicholson, Phil. Mag., 17, 801 (1968).
145. R. Sankaran and C. Laird, Phil. Mag., 29, 179 (1974).
146. R.J. Livak and G. Thomas, Acta Met., 22, 589 (1974).
147. G.C. Weatherly and C.M. Sargent, Phil. Mag., 22, 1049 (1970).

148. G.C. Weatherly, *Acta Met.*, 19, 181 (1971).
149. G.C. Weatherly and T.D. Mok, *Surf. Sci.*, 31, 335 (1972).
150. J.M. Rigsbee and H.I. Aaronson, *Acta Met.*, 27, 351 (1979).
151. D.A. Porter and K.E. Easterling, "Phase Transformations in Metals and Alloys", Van Nostrand Reinhold, 1981.
152. K.E. Easterling and T. Johannesson, *Phil. Mag.*, 24, 179 (1971).
153. I.W. Mathews, *Phil. Mag.*, 29, 797 (1974).
154. C.M. Sargent and G.R. Purdy, *Phil. Mag.*, 32, 27 (1975).
155. P.P.K. Smith, P.F. Champness and G.W. Lorimer, Ref. 76, p. 581.
158. L.F. Mondolfo, "Aluminium Alloys", Butterworths, 1976.
159. I.J. Polmear, "Light Alloys", American Society for Metals, 1982.
160. J.W. Morris, L. Brewer, J.R. Cost and P.G. Shewmon, *Mat. Sci. Eng.*, 35, 75 (1978).
161. M. Hansen and K. Anderko, "Constitution of Binary Alloys", McGraw-Hill, 1958.
162. P. Guyot, 1981. Lecture given at McMaster University.
163. T. Ungar, J. Lendrai and I. Kovacs, *Phil. Mag.*, 43A, 927 (1981).
164. D. Schwahn and W. Schmatz, *Acta Met.* 26, 1571 (1978).
165. R. Hultgren, R.L. Orr, P.D. Anderson, K.K. Kelly, "Selected Values of Thermodynamical Properties of Binary Alloy" ASM, 1973.

166. G.W. Lorimer, "Precipitation in Al alloys", Ref. 111, p. 87.
167. M. Simerska and V. Synecek, Acta Met., 15, 223 (1967).
168. G.J.C. Carpenter and R.D. Garwood, Met. Sci. J., 1, 203 (1967).
169. K.B. Rundman and J.E. Hilliard, Acta Met., 15, 1052 (1967).
170. J.W. Cahn, Acta Met., 8, 1 (1961).
171. L.M. Brown, J. Phys. F: Metal Phys., 11, 1 (1981).
172. J.I. Goldstein in "Introduction to Analytical Electron Microscopy", (eds. J.J. Hren, J.I. Goldstein and D.C. Joy), p. 101, Plenum Press, 1979.
173. N. Zaluzec, in ref. 172, p. 121.
174. J.I. Goldstein and D.B. Williams, SEM/1977, 651 (1977).
175. G. Cliff and G.W. Lorimer, Proc. 5th Europ. Congress on Electron Microscopy, 1972.
176. J. Venables and A.P. Janssen, Ultramicroscopy, 4, 297 (1980).
177. B. Robertson, 1981, private communication.
178. E.L. Hall, D. Imeson and J.B. Vander Sande, Phil. Mag., 43A, 1569 (1981).
179. M.E. Twigg, M.H. Loretto and H.L. Fraser, Phil. Mag. 43A, 1587 (1981).
180. I.P. Jones and M.H. Loretto, J. Microsc., 124, 3 (1981).
181. R.H. Geiss and D.F. Kyser, Ultramicroscopy, 3, 379 (1979).
182. D.E. Newburg and R.L. Mykubust, *ibid.*, 3, 391 (1979).
183. J.I. Goldstein, J.L. Costley, G. Lorimer and G. Reed, SEM/77, 315 (1977).

184. P. Wycliff, Ph.D. thesis, McMaster University, 1982.
185. R. Tixier and J. Philibert, Proc. 5th Conf. X-ray Optics and Microanalysis, 180, Springer, 1969.
186. B. Robertson, 1980, Unpublished work.
187. D. Houghton, Proceedings of the EMAG Conference 1982.
188. R. Woldseth, "X-Ray Energy Spectrometry", Kevex Corporation, 1973.
189. P.M. Kelly, A. Jostons, R.C. Blake and J.W. Napier, Phys. Stat. Sol., A31, 771 (1975).
190. A.J. Ardell, K. Nuttal and R.B. Nicholson, Ref. 10, p. 22.
191. J.W. Steeds, Ref. 172, p. 387.
192. R. Glitz, M. Notis and J.I. Goldstein, Ref. 76, p. 691.
193. P.E. Champness, G. Cliff and G.W. Lorimer, Ultramicroscopy, 8, 121 (1982).
194. A. Häsner, Kristall. und Tech., 9, 1371 (1974).